Nucleon Structure and Its Modification in Nuclei

by

Barak Schmookler

B.S. Physics, North Carolina State University (2011)

Submitted to the Department of Physics
in partial fulfillment of the requirements for the degree of

Doctor of Philosophy in Physics

at the

MASSACHUSETTS INSTITUTE OF TECHNOLOGY

September 2018

Author ..... Signature redacted

Department of Physics
August 21, 2018

Certified by ..... Signature redacted .....

Or Hen
Assistant Professor
Thesis Supervisor

Certified by ..... Signature redacted .....

Shalev Gilad
Principal Research Scientist
Thesis Supervisor

Accepted by ..... Signature redacted .....

Nergis Mavalvala
Associate Department Head, Physics

Nucleon Structure and Its Modification in Nuclei

by

Barak Schmookler

Submitted to the Department of Physics
on August 21, 2018, in partial fulfillment of the
requirements for the degree of
Doctor of Philosophy in Physics

Abstract

Inclusive electron scattering experiments using fixed targets are an important tool for studying the structure of the nucleons. The electromagnetic structure of the proton, as encapsulated by its elastic form factors, can be extracted through measurements of the elastic electron-proton scattering cross-section. The *GMp* experiment in Hall A at the Thomas Jefferson National Accelerator Facility (JLab) seeks to measure this cross-section with high precision up to large momentum transfers. In addition, it is known that the inelastic structure of the nucleon is modified inside the nucleus. This modification, known as the *EMC* effect, can be studied using inclusive electron Deep Inelastic Scattering (DIS) on a nuclear target. Evidence suggests that the *EMC* effect may arise due to nucleon Short Range Correlations (SRC). This thesis describes studies of the elastic proton form factor measured in the *GMp* experiment at Hall A of JLab and studies of the *EMC* effect in nuclei relative to deuterium using data collected at the *CLAS* detector in Hall B at JLab. Furthermore, this works presents new measurements of SRC pair abundances in nuclei and develops a data-driven SRC-based phenomenological model of the *EMC* effect, which can correctly describe the effect across nuclei.

Thesis Supervisor: Or Hen
Title: Assistant Professor

Thesis Supervisor: Shalev Gilad
Title: Principal Research Scientist

Acknowledgments

During my time in graduate school, I have been afforded the opportunity to work on many different projects. I was able to work on experiments in Hall A, Hall B, and the free-electron laser at JLab; an experiment at the Cornell Electron Storage Ring; and phenomenology at MIT. For giving me the independence to pursue all this work, and for providing the help and support I needed to obtain actual physics results, I want to thank my research supervisors, Or Hen and Shalev Gilad. I also would like to thank Bill Bertozzi and Or and Shalev for the way that they seamlessly managed the recent transition of our group at MIT.

We have a great research group at MIT. Besides Or and Shalev, we have visiting scientists, postdocs, graduate and undergraduate students. I want to acknowledge the guidance provided to my by Axel Schmidt; he really helped me see how one can successfully transition from being a graduate student to conducting research as a post-doc. I can't thank enough my fellow graduate student Longwu Ou for his friendship and willingness to patiently entertain all my (usually simplistic) questions. During my last year at MIT, I also worked with two undergraduate students, Adrian Silva and Joe Iosue, teaching them how to analyse nuclear and particle physics data. Seeing how quickly they were able to learn analysis techniques was a real encouragement to me. I'm sure they will go far in whatever field they choose to pursue.

For our work on Deep Inelastic Scattering and Short Range Correlations, our group collaborates with several universities, including Old Dominion University and Tel Aviv University. Thank you to Larry Weinstein and Eli Piasetzky for their help with the work discussed in this thesis.

I spent several years of my graduate studies at JLab, during which time I had the opportunity to work with scientists at the lab and at various universities. I had the opportunity to work with Bogdan Wojtsekhowski, Eric Christy, and Stepan Stepanyan while at the lab. I learned much from each of them, for which I am very grateful. Our own MIT group had two postdocs stationed at the lab, Vincent Sulkosky and Kalyan Allada. I want to thank them for their help. There were many graduate students at

JLab that I got to know quite well during my time there. In particular, I will always remember Dien Nguyen's friendship and support. Dien will in fact be joining our group at MIT in a few months, and I wish her all the best.

I also want to thank William Detmold and Richard Milner for serving on my thesis committee.

Finally, thank you to my parents and sister for all your past and continued encouragement and support.

Contents

List of Figures

List of Tables

Chapter 1

Introduction

Nuclear physics is the study of quark-gluon bound states. As is well known, the atomic nucleus is composed of these bound states in the form of neutrons and protons, which are collectively called nucleons. An understanding of the structure of these nucleons and their mutual interactions is therefore vital for a complete physical description of the fundamental nature of matter.

Charged leptons, which are point-like particles and interact through the electromagnetic force, can be used as probes to study the internal structure of complex objects like the nucleons. The structure of the probed object can be extracted by measuring differential scattering cross-sections where only the lepton is detected (i.e. inclusive scattering). The resolving power of the leptonic probe, as characterized by the momentum and energy transfer, determines which features of the object are being studied. This can be seen in figure 1-1: as the energy transfer is increased, finer and finer underlying aspects of the target are resolved.

If the object under study is a proton, and the momentum transfer is such that the process is elastic scattering, the measured cross-sections provide knowledge on the electromagnetic structure of the proton. These charge and magnetic distributions are encapsulated in momentum space by the proton electromagnetic form factors [1]. Quasi-elastic (QE) scattering is elastic scattering off a moving nucleon inside the nucleus [2, 3]. If the leptonic probe is tuned to study quasi-elastic scattering, the measured cross-sections will provide information on how the nucleons move inside the

nucleus. If the resolving power is increased even more, the probe becomes sensitive to the underlying partonic structure of the target [4]. This in known as Deep Inelastic Scattering (DIS), and the cross-sections here depend on the underlying quark-gluon dynamics inside the nucleus.

These three reactions are generally studied in separate experiments, but the information from all of them is combined to form a consistent picture of the nucleon and Quantum Chromodynamic (QCD) effects in the nuclear medium. This thesis presents a study of all three of these reactions using inclusive electron scattering. The results are used to improve our understanding of nucleon structure and its modification inside the nucleus.

This chapter will discuss the formalism of electron scattering in the elastic, quasi-elastic, and Deep Inelastic regimes. It will highlight the most salient features and results in each case. Section 1.4 in this chapter will discuss the modification of the nucleon structure inside the nucleus, referred to as the European Muon Collaboration (*EMC*) effect.

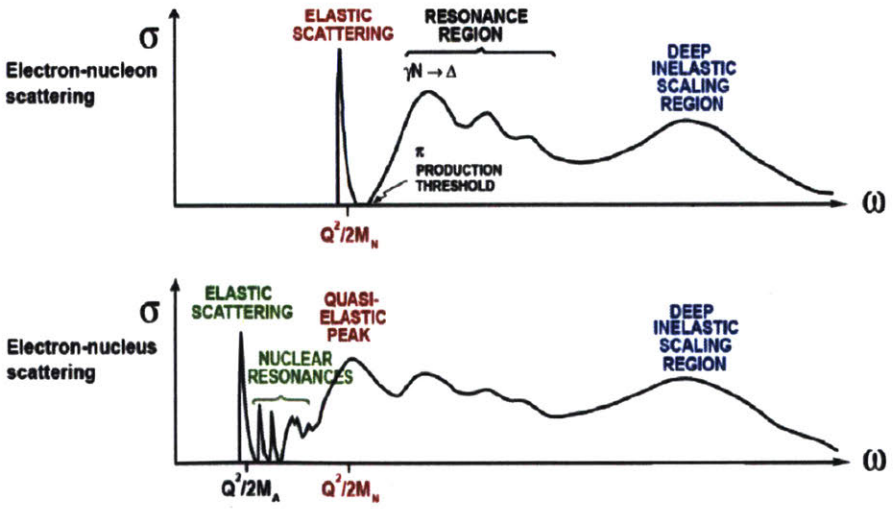

Figure 1-1: Top: The total cross-section for electron-nucleon scattering on a free nucleon as a function of the energy transfer. Bottom: The total cross-section for various processes in electron-nucleus scattering as a function of energy transfer. This work focuses on the elastic, QE, and DIS regions.

1.1 Elastic Electron-Proton Scattering

The cross-section for elastic electron-proton scattering in the Born approximation can be written in terms of two form factors, which express the electromagentic structure of the proton [5]. This process is shown in figure 1-2. With the initial proton at rest, for a given incident electron energy E, the scattered electron angle θ_e fully defines the final state. Therefore, the cross-section will be differential with respect to a single variable, usually chosen to be θ_e. The kinematic variables needed to best describe this process, as well as the other processes discussed later in this chapter, are

$$\nu = E - E' , \tag{1.1}$$

$$Q^2 = -q^2 = 4EE' \sin^2\left(\frac{\theta_e}{2}\right) , \tag{1.2}$$

$$W = \sqrt{(P+q)^2} = \sqrt{M^2 + 2M\nu - Q^2} , \tag{1.3}$$

$$x_B = \frac{Q^2}{2M\nu} , \tag{1.4}$$

$$\tau = \frac{Q^2}{4M^2} , \tag{1.5}$$

$$\epsilon = \left[1 + 2(1+\tau)\tan^2\left(\frac{\theta_e}{2}\right)\right]^{-1} , \tag{1.6}$$

where E is the initial electron energy, E' is the scattered electron energy, θ_e is the electron scattering angle, and M is the mass of the proton. In the above set of equations ν is the energy transfer; Q^2 is the squared four-momentum transfer; W is the mass of the final state hadronic system, which is equal to M for elastic scattering; x_B is the Björken scaling variable, which is equal to one for elastic scattering; τ is a variable used in the definition of ϵ; and ϵ is the longitudinal polarization of the virtual

photon.

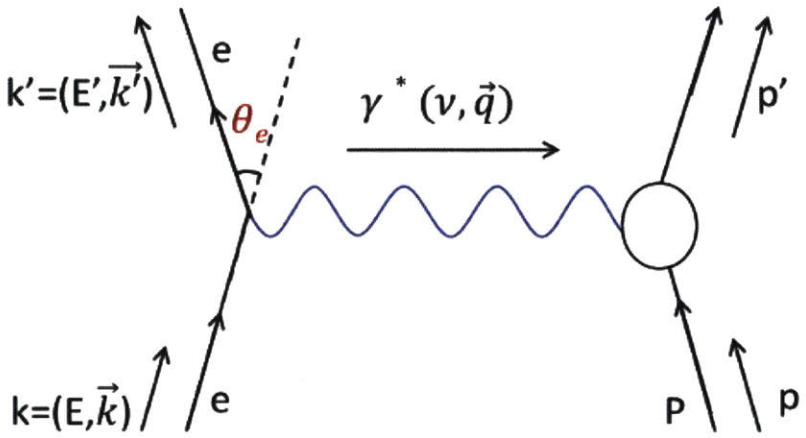

Figure 1-2: Feynman diagram for elastic electron-proton scattering at lowest order.

Since the electron is a point-like particle, the electron current, j_μ, can be written as

$$j_\mu = -e\bar{u}(k')\gamma_\mu u(k)\,, \tag{1.7}$$

where γ_μ represents the simple vertex matrix, and $u(k)$ and $\bar{u}(k')$ are the Dirac spinors for the incoming and outgoing electrons, respectively. The more complex proton current, J_μ, can be written as

$$J_\mu = e\bar{v}(p')\Gamma_\mu v(p)\,, \tag{1.8}$$

where Γ_μ represents the proton vertex, and $v(p)$ and $\bar{v}(p')$ are the Dirac spinors for the incoming and outgoing protons, respectively.

The scattering amplitude can then be written as

$$iM = \frac{-i}{q^2}[ie\bar{v}(p')\Gamma_\mu v(p)][ie\bar{u}(k')\gamma_\mu u(k)]\,. \tag{1.9}$$

Under the assumptions of Lorentz covariance, current conservation, and parity conservation [5] and using some simple identities [6], we can write the spin-averaged

cross-section as

$$\frac{d\sigma}{d\Omega} = \left(\frac{d\sigma}{d\Omega}\right)_{Mott} \left(\frac{E'}{E}\right) \frac{1}{1+\tau} \left(G_{Ep}^2(Q^2) + \frac{\tau}{\epsilon} G_{Mp}^2(Q^2)\right) , \tag{1.10}$$

where $G_{Ep}(Q^2)$ and $G_{Mp}(Q^2)$ are the electric and magnetic form factors, respectively. The Mott cross-section is defined as

$$\left(\frac{d\sigma}{d\Omega}\right)_{Mott} = \frac{\alpha^2 \cos^2 \frac{\theta_e}{2}}{4E^2 \sin^4 \frac{\theta_e}{2}} , \tag{1.11}$$

where α is the fine-structure constant. The Sachs form factors, G_{Ep} and G_{Mp}, are related to the Pauli and Dirac form factors, F_1 and F_2, by

$$\begin{aligned} G_{Ep} &= F_1 - \tau F_2 \\ G_{Mp} &= F_1 + F_2 . \end{aligned} \tag{1.12}$$

Since the form factors are only a function of Q^2, they can be extracted by measuring the cross-section at multiple ϵ points for a given Q^2 value. This technique called the Rosenbluth separation method [7].

Another way of extracting the ratio of the electromagnetic form factors is the recoil polarization method [8]. In this method, the longitudinal and transverse polarization components of the final-state proton are measured. The ratio of the form factors is proportional to the ratio of these two polarization components. As can be seen in figure 1-3, the form factors extracted by Rosenbluth separation method differ from those obtained using the recoil polarization method [1]. Several explanations have been proffered for this discrepancy, with the most likely being an incomplete understanding of the hard two-photon radiative correction [1, 6, 9]. The *GMp* experiment will extract precision cross-section measurements at high Q^2 and low ϵ, allowing for a better understanding of two-photon effects.

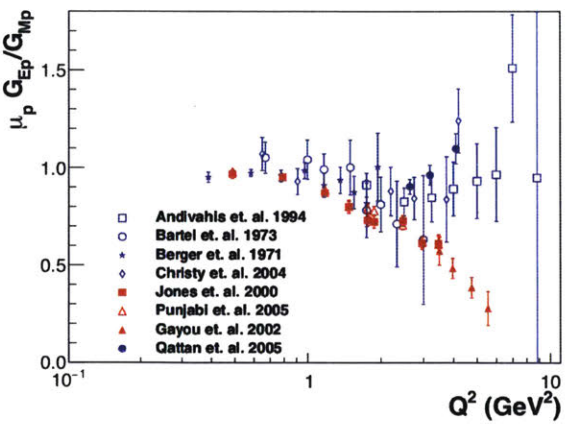

Figure 1-3: Ratio of the electric to magnetic proton form factors using the Rosenbluth technique (blue points) and the recoil polarization technique (red points). Figure taken from Ref. [6].

1.2 Quasi-elastic Electron-Nucleon Scattering

In the simplest sense, quasi-elastic (QE) electron-nucleon scattering is elastic scattering off a moving nucleon in the nucleus. QE reactions off a nucleus A will give a final state consisting of the scattered electron, a single separated nucleon, and the A-1 nucleus (potentially in an excited state).

In the plane-wave impulse approximation (PWIA), the scattering interaction takes place between a single virtual photon and a single nucleon, with the other nucleons as spectators to the reaction (figure 1-4) [2, 3]. Under this approximation the (e,e'N) cross-section can be written as

$$\frac{d^6\sigma}{d\nu d\Omega_e dE_p d\Omega_p} \propto \sigma_{eN} \times S(P_m, E_m)\,, \tag{1.13}$$

where σ_{eN} is the off-shell electron-nucleon cross-section, P_m is the missing momentum and E_m is the missing (i.e. separation) energy. The term $S(P_m, E_m)$ is the spectral function, and it represents the probability of finding a nucleon with missing momentum P_m and missing energy E_m inside the nucleus.

The momentum distributions of the nucleons inside the nucleus can be probed using this type of reaction. One interesting feature of the nuclear wave function is the high-momentum tail, which makes up about 20% of the strength of the wave function

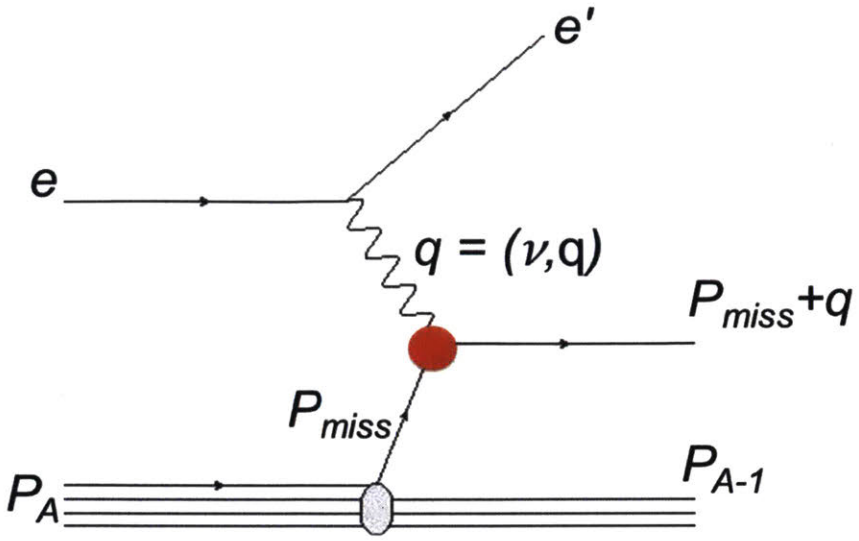

Figure 1-4: Quasi elastic electron-nucleon scattering in the plane-wave impulse approximation. The important kinematic variables are listed on the plot. Figure taken from Ref. [3].

for moderate to heavy nuclei [3]. From double and triple coincidence reactions, we also know that this tail consists primarily of nucleons in Short Range Correlation (SRC) pairs. These SRC pairs are nucleons which are dynamically close to each other in the nucleus and have a large relative but small center-of-mass momentum, where large and small are with reference to the Fermi momentum. These SRC pairs prefer deuteron-like configurations, with neutron-proton pairs being much more likely to form than either proton-proton or neutron-neutron pairs [2, 3]. A cartoon of the nucleon momentum distribution listing all these features is shown in figure 1-5.

Inclusive scattering can in fact be used to study these SRC pairs. For the PWIA diagram in figure 1-4, we can write the four-momentum conservation equation as

$$(q + p_A - p_{A-1})^2 = p_f^2 = m_N^2 \,. \tag{1.14}$$

For inclusive scattering, only q and p_A are known in the above equation. However, using this equation, we can determine the minimum momentum of the struck nucleon if we know Q^2 and x_B [10]. This momentum is the component of the stuck nucleon's initial momentum parallel to $\vec{q}$ when the residual A-1 nucleus remains in an unexcited state.

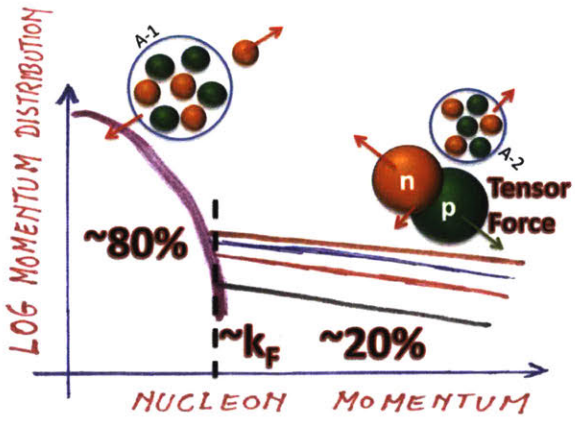

Figure 1-5: Cartoon showing the gross features of the momentum-space nuclear wave function which are discussed in the text. Figure adapted from Ref. [3].

The upshot of this is that the high momentum part of the nuclear wave function (which consists primarily of SRC pairs) can be probed using inclusive scattering by going to large enough Q^2 and x_B (figure 1-6). This is the region where the nuclear wave function is mostly deuteron-like, but with a small number of pp and nn SRC pairs. The use of inclusive scattering is in the calculation of the per-nucleon cross-section ratio for a nucleus A to deuterium in this high initial momentum region. We call this ratio $a_2(A/d)$, and it tells us the probability of finding a nucleon in the high momentum region for a nucleus A relative to deuterium.

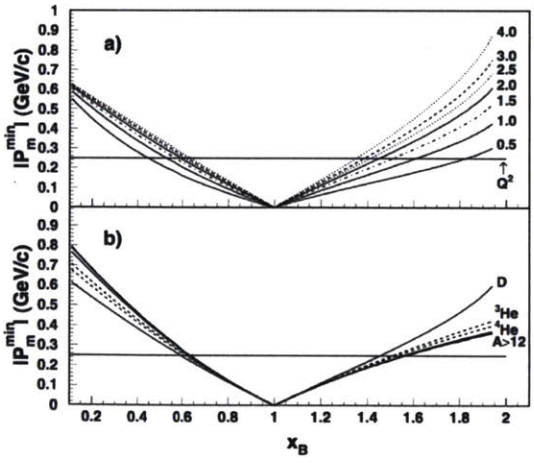

Figure 1-6: Top: Minimum momentum of the struck nucleon in deuterium as a function of x_B for several Q^2 values. Bottom: Minimum momentum of the struck nucleon for various nuclei at $Q^2 = 2.0\ GeV^2$. Figure taken from Ref. [10].

The main interest of this work is nucleon structure and how that structure is modified inside the nucleus. Section 1.4.2 will discuss how this nucleon structure modification may be related to SRC.

1.3 Deep Inelastic Electron Scattering

As the amount energy transferred to the target by the charged lepton is increased, the nucleon can be excited into a resonance state. As the resolving power of the leptonic probe is increased even further, the inclusive scattering cross-section becomes sensitive to the details of the quarks and gluons inside the nucleon. Here the lepton is scattering from the point-like quarks inside the nucleon in a process called Deep Inelastic Scattering (DIS). DIS provided the iron-clad proof that the nucleons do indeed have a partonic sub-structure.

For inclusive inelastic scattering (either in the resonance or DIS region), the struck nucleon will be left in a final state with a total mass (W) greater than the nucleon mass. This process is shown in the Born approximation in figure 1-7. Using the same assumptions as in section 1.1, the inelastic electron-proton inclusive scattering cross-section can be written as [4, 11]

$$\frac{d^2\sigma}{d\Omega dE'} = \frac{4\alpha^2 E'^2}{Q^4}\left[2\frac{F_1(x_B,Q^2)}{M}\sin^2\frac{\theta_e}{2} + \frac{F_2(x_B,Q^2)}{\nu}\cos^2\frac{\theta_e}{2}\right], \tag{1.15}$$

where F_1 and F_2 are the two structure functions. In this case, unlike in equation 1.10 for elastic scattering, the cross-section and structure functions and differential with respect to both the scattered electrons's angle and energy. In fact, the elastic-electron proton scattering cross-section is equivalent to the above equation with $x_B = 1$ and a delta-function relating E' and θ_e.

The interest of this thesis is DIS, where the virtual photon interacts with the point-like quarks inside the nucleon. One important consequence of this picture is that as the energy and momentum transfer increase, the structure functions, F_1 and F_2, become only logarithmically dependent on Q^2. This evolution of F_1 and F_2 from functions of two variables to functions of x_B only is called Björken Scaling.

Experimental confirmation of this aspect of DIS is shown in figure 1-8.

Björken Scaling can be qualitatively understood as follows. When the four-momentum transfer is high enough, the time scale of the photon-quark interaction is short compared to that of the interactions between the partons themselves, and the quarks can be regarded as nearly free particles inside the nucleon. So in DIS the leptonic probe is elastically scattering off a quark. For elastic scattering where the two particles' incident energies are known, the kinematics and the cross-section are fully determined by the scattering angle of one of the particles. For lepton-quark scattering, the incident quark has a momentum distribution. So the energy distribution of the scattered lepton at a given scattering angle depends on the quark momentum distribution inside the nucleon [11]. In this picture, x_B represents the fraction of the nucleon's momentum carried by the struck quark in the infinite momentum frame.

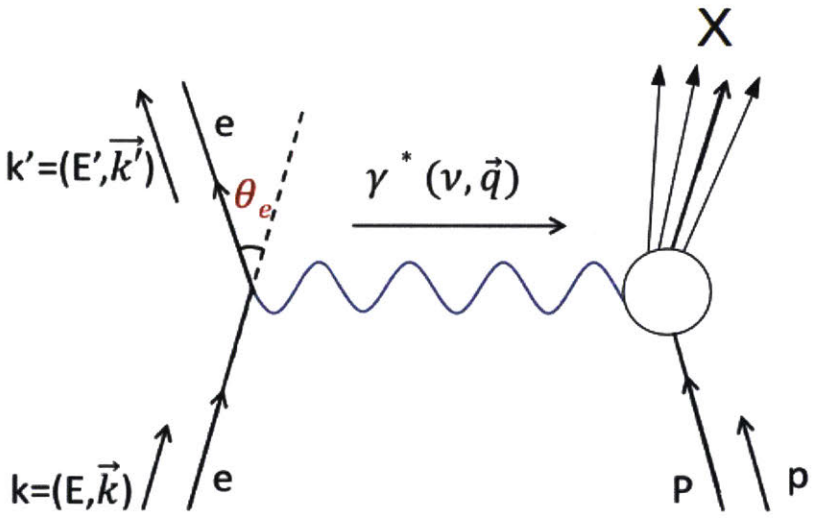

Figure 1-7: Inelastic scattering of an electron and proton at lowest order. The final hadronic state, X, is undetermined in inclusive scattering and will have a mass greater than the proton mass.

In this model, we can then proceed to write the structure functions as

$$F_1(x_B) = \frac{1}{2}\sum_i e_i^2 \left[q_i(x_B) + \bar{q}_i(x_B)\right], \tag{1.16}$$

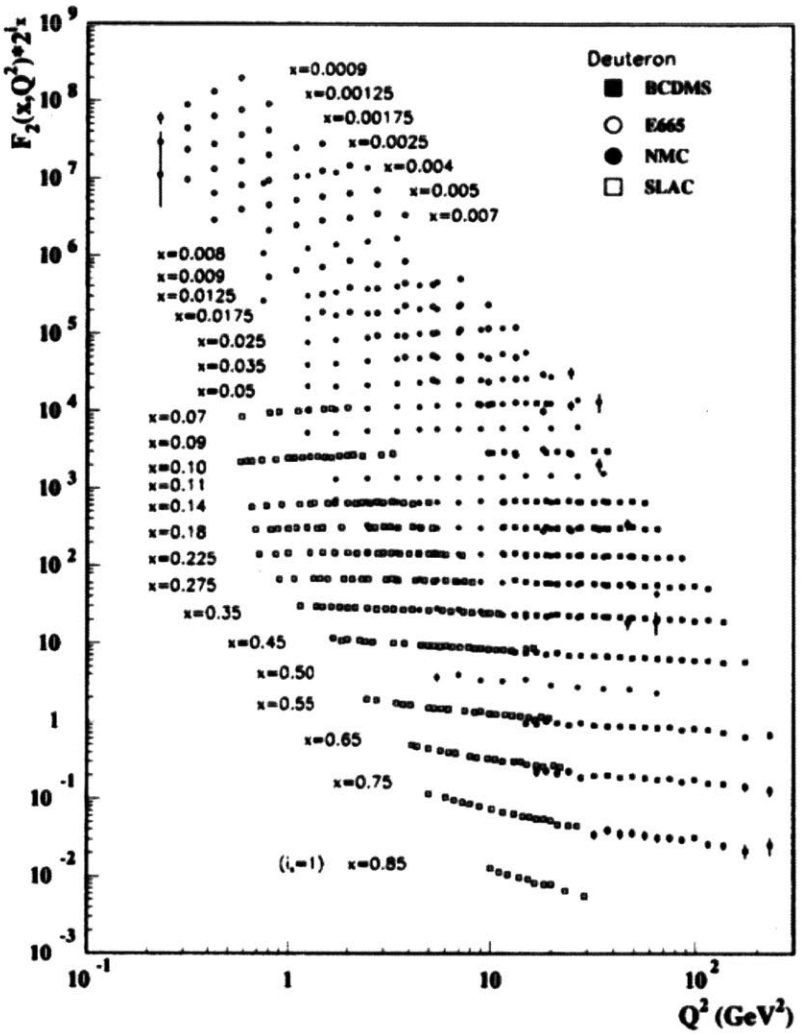

Figure 1-8: Limited Q^2 dependence of the inelastic inclusive F_2 structure function in the DIS regime. This feature is called Björken scaling. Figure taken from Ref. [12].

$$F_2(x_B) = \sum_i e_i^2 \, x_B \left[q_i(x_B) + \bar{q}_i(x_B) \right], \tag{1.17}$$

where the sum is over all quark flavors, e_i^2 is the charge of the quark, and $q(x_B)$ and $\bar{q}(x_B)$ represent the quark and anti-quark momentum distribution functions, respectively. For a given quark flavor, the distribution function, $q(x_B)$, are the combination of the valence-quark distribution function and the sea-quark distribution function. In this model, the structure functions are related by the Callan-Gross equation [12]

$$F_2(x_B) = 2x_B F_1(x_B) \, . \tag{1.18}$$

We will discuss one other item that is needed for the description of the *EMC* effect in the next section. The cross-section in equation 1.15 can be written as

$$\frac{d^2\sigma}{d\Omega dE'} = \Gamma \left[\sigma_T(x_B, Q^2) + \epsilon\, \sigma_L(x_B, Q^2)\right] , \tag{1.19}$$

where Γ is the virtual photon flux, and $\sigma_{T(L)}$ is transverse (longitudinal) cross-section. The ratio, R, of these cross-section components can be related to the structure functions as

$$R = \frac{\sigma_L}{\sigma_T} = \left(1 + \frac{\nu^2}{Q^2}\right) \frac{M}{\nu} \frac{F_2}{F_1} - 1 . \tag{1.20}$$

Rearranging this equation gives

$$\frac{\nu}{M} \frac{F_1}{F_2} = \frac{1 + \frac{\nu^2}{Q^2}}{R + 1} . \tag{1.21}$$

1.4 The EMC Effect

Now that we have described the formalism of DIS and how it can be used to probe the inelastic structure of the nucleon, we will consider how that structure is modified inside the nucleus. The nucleons inside the nucleus are bound by several MeVs, while the nucleons themselves have masses of about a GeV that stem primarily from the interactions of the constituent partons (quarks and gluons). On account of this 'scale separation', it was both surprising and intriguing when evidence was discovered that the inelastic structure of the nucleons is indeed modified in the nuclear medium [13]. This evidence, called the European Muon Collaboration (*EMC*) effect in honor of the discoverers, has been under experimental and theoretical study for approximately 35 years, and there is still no consensus on the QCD-driven quark-gluon dynamics underlying the effect.

We will begin by considering the inclusive scattering cross-section for a charged lepton on a nucleus A. The differential cross-section per-nucleon for a nucleus A will

be

$$\sigma_A/A = \frac{4\alpha^2 E'^2}{Q^4}\left[2\frac{F_1^A(x_B,Q^2)}{M}\sin^2\frac{\theta_e}{2} + \frac{F_2^A(x_B,Q^2)}{\nu}\cos^2\frac{\theta_e}{2}\right]\Big/A\ , \tag{1.22}$$

where σ_A is the doubly-differential cross-section, and F_1^A and F_2^A are the inelastic structure functions for the nucleus. (Note that the definition of $F_{1(2)}^A$ used here is equivalent to the $A \cdot F_{1(2)}^A$ in some other works.)

Therefore, the ratio of the per-nucleon cross-sections for nuclei A_1 and A_2 is

$$\frac{(\sigma_{A_1}/A_1)}{(\sigma_{A_2}/A_2)} = \frac{A_2}{A_1}\frac{F_2^{A_1}}{F_2^{A_2}}\frac{\left[1+2\frac{\nu}{M}\frac{F_1^{A_1}}{F_2^{A_1}}\tan^2\frac{\theta_e}{2}\right]}{\left[1+2\frac{\nu}{M}\frac{F_1^{A_2}}{F_2^{A_2}}\tan^2\frac{\theta_e}{2}\right]}\ . \tag{1.23}$$

If the ratio of the longitudinal to transverse cross-section (equation 1.20) is independent of A, then, from equation 1.21, the cross-section ratio reduces to the ratio of the structure functions:

$$\frac{(\sigma_{A_1}/A_1)}{(\sigma_{A_2}/A_2)} = \frac{(F_2^{A_1}/A_1)}{(F_2^{A_2}/A_2)}. \tag{1.24}$$

Measurements have been made of R for some nuclei, and the results show that R is independent of the nucleus to the several percent level [4, 13]. So the cross-section ratio of two nuclei can be considered equivalent to their structure function ratio.

1.4.1 Observation of the Effect

The original *EMC* measurement was conducted at CERN using a muon beam and an iron and deuterium target [13]. The initial purpose of the experiment was to study lepton-nucleon scattering at very high beam energies. Due to the low muon beam intensity, an iron target was used to boost the event rate [4, 11]. After accounting for known nuclear physics effects, such as the Fermi motion of the nucleons and neutron excess [14], the collaboration expected to find structure function ratios (cross-section ratios) equal to unity. Their results are shown in figure 1-9. As can be seen in the figure, although the nuclear physics considerations can explain part of the effect, the entire *EMC* effect can not be explained without either modifying the internal

structure of the nucleons or including multi-nucleon effects.

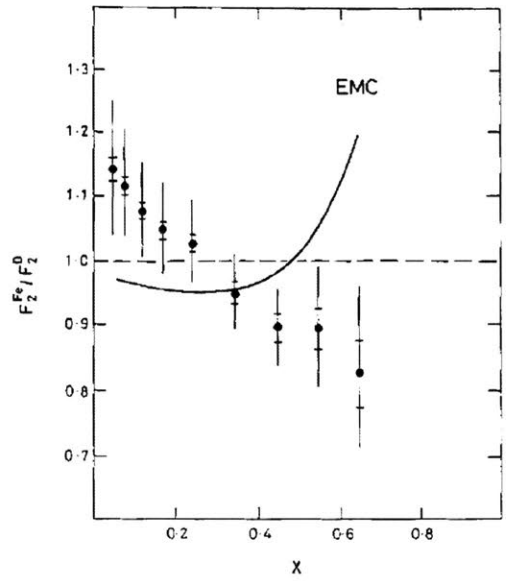

Figure 1-9: Final published result for the original *EMC* effect measurement on iron and deuterium. The figure is taken from Ref. [15]. It differs a bit from the original result in Ref. [13], primarily due to a re-normalization of the ratio. The solid curve shows a prediction if only nuclear effects are included.

The *EMC* collaboration then made more detailed studies on the cross-section ratio of muon scattering off carbon, copper, and tin relative to deuterium [16]. They found that the cross-section ratio was less than unity for $x_B < 0.09$ and that the ratio between $0.09 < x_B < 0.2$ was greater than unity (but the enhancement was reduced from the original measurement). The features in this region can be explained by shadowing and anti-shadowing. They once again found the cross-section to decrease linearly in the *EMC* region between $0.3 < x_B < 0.7$.

Additional measurements of the *EMC* effect, which confirmed the original result, were performed by the BCDMS collaboration [17] and at the Thomas Jefferson National Accelerator Facility (JLab) on light nuclei [18].

The most systematic studies were performed at SLAC [19]. The SLAC experiment made *EMC* effect measurements using an electron beam on ^{4}He, Be, C, Al, Ca, Fe, Ag, and Au relative to deuterium in the range $0.1 < x_B < 0.9$. This experiment confirmed that the effect was universal (i.e. the shape of the ratio was the same for

all nuclei). It also showed that the magnitude of the effect (which is best characterized by the slope of the ratio in the *EMC* region $0.3 < x_B < 0.7$) depends on the nucleus. In addition, the SLAC data was collected in the Q^2 range $2\ GeV^2 < Q^2 < 12\ GeV^2$, and the experiment found no Q^2 dependence to the *EMC* effect.

One question that can be considered is why *EMC* effect measurements are performed relative to deuterium as opposed to hydrogen. The reason for this is that elementary DIS lepton-proton and lepton-neutron cross-sections are very different. So when comparing the cross-section of a nucleus A to hydrogen, most of the difference will be due to the difference in the lepton-proton and lepton-neutron cross-sections. When comparing a non-isoscaler nucleus A to deuterium, the correction to the ratio due to unequal numbers of protons and neutrons in a nucleus A is on the order of a few percent. Therefore the deuteron, which is a loosely bound state of a proton and a neutron, is used for all *EMC* effect measurements. In the *EMC* region, corrections due to binding and nucleon motion for the deuteron are smaller than 3% [13].

1.4.2 Current Hypotheses

We will briefly discuss current theoretical hypotheses used to model the *EMC* effect. Additional details can be found in Refs. [3, 4, 14, 16].

The most conventional way to try to explain the *EMC* results is by using models based on single nucleons, including the effects of nuclear binding and Fermi motion [20, 21]. The average off-shell nucleon in a nucleus has a separation energy ϵ_s and momentum $\vec{p}$ related by

$$\epsilon_s + \frac{\vec{p}^2}{2M} \approx -16\ MeV\ . \tag{1.25}$$

The nucleon's four momentum is now $(M + Kinetic\ Energy + \epsilon_s, \vec{p})$, and we define the variable x_A as

$$x_A = \frac{AM}{M_A} \cdot x_B\ , \tag{1.26}$$

where M is the nucleon mass, M_A is the mass of the nucleus, A is the mass number of the nucleus and x_B is the standard Björken-x variable. x_A represents x_B corrected

for the average nucleon binding energy.

In the nucleon-only models, the structure function per-nucleon for a nucleus A is written as

$$F_2^A(x_A)/A = \int_{x_A}^{A} dy f_N(y) F_2^N(x_A/y)\,, \tag{1.27}$$

where y is the fraction of the nuclear momentum carried by a single nucleon divided by the number of nucleons, $f_N(y)$ is the corresponding probability distribution for the struck nucleon, and F_2^N is the free average nucleon structure function. For non-interacting, stationary nucleons, $f_N(y)$ is a delta function peaked at $y = 1$. Fermi motion causes the distribution to have a non-zero width; defining $\epsilon = -\epsilon_s/M$, binding effects shift the peak to $y = 1 - \epsilon$.

If the width of $f_N(y)$ is ignored, equation 1.27 can be simplified as

$$F_2^A(x_A)/A \approx F_2^N\left(\frac{x_A}{1-\epsilon}\right). \tag{1.28}$$

This equation indicates that the structure function in a nucleus is equivalent to the free nucleon structure function evaluated at a slightly higher x_A value. As can be seen in figure 1-8, the nucleon structure function falls with increasing x_B in the *EMC* region. A value of $\epsilon = 0.04$ is sufficient to explain the effect [22].

However, shifting the peak of the $f_N(y)$ violates momentum sum rules [3] since it implies that

$$\int dy\, y f_N(y) = 1 - \epsilon. \tag{1.29}$$

In addition, relativistic corrections significantly reduce the strength of nuclear binding effects [22]. So, single-nucleon models can not explain the *EMC* effect.

The nuclear binding models can be combined with models based on the enhancement of the pion field associated with the nucleon-nucleon interaction in the nucleus [23]. In this case, the momentum suppression in equation 1.29 is compensated for by pions. These combined models can account for the *EMC* effect if the nuclear pions carry about 4% of the nuclear momentum [3]. This would lead to an enhancement of the sea, which would be observable in Drell-Yan experiments. But such an

enhancement was not seen in the Drell-Yan results [24].

It is now generally believed [3] that the conventional nuclear effects described above can explain part of the *EMC* effect up to $x_B \approx 0.5$ but not at higher values [14]. This means that a complete explanation of the effect requires either multi-nucleon effects or modification of the nucleon structure function inside the nuclear medium. Since the structure function encapsulates the momentum distributions of the quarks, the reduction in the structure function of a nucleus A relative to deuterium suggests that the valence quarks in the nucleus have less momentum than in the free nucleon [4]. Based on the uncertainty principle, this suggests that the quarks are confined to a larger volume in the nucleus compared to a free nucleon. Some viable current mean-field, static modification models are based on this idea [25, 26, 27].

One intriguing recent result is the observed linear correlation between the strength (i.e. slope) of the *EMC* effect and the SRC pair fraction probability, $a_2(A/d)$ [28, 29]. This correlation is shown in figure 1-10. If the *EMC* effect is related to nucleon SRCs, this suggests that any complete model of effect needs to include momentum-dependent, dynamic modification that goes beyond the mean-field.

One approach to the *EMC* that includes SRCs is discussed in Ref. [3]. Both the QE and the DIS reactions on a nuclear target have a virtual photon interacting with a nucleon initially moving with four-momentum p (figure 1-4). We define the virtuality of the nucleon, v, as

$$v \equiv p^2 - M^2 \,. \tag{1.30}$$

In the non-relativistic case, this reduces to

$$v \approx -2M \left(\frac{\vec{p}^2}{2M_r} + E_m \right) \,, \tag{1.31}$$

where $M_r = M(A-1)/A$. Writing the Schrödinger equation as

$$\frac{\vec{p}^2}{2M_r} + U = -E_m \,, \tag{1.32}$$

where U represents the nuclear interaction - both the binding and the nucleon modi-

fication. Combining equations 1.31 and 1.32, we get

$$U = \frac{v}{2M_r} . \tag{1.33}$$

This means that the interaction U is proportional to the virtuality, with SRCs being the dominant contribution to the average nucleon virtuality. So a model of the *EMC* effect dominated by nucleon SRCs needs to show that the nucleon modification increases as the magnitude of U increases.

The nucleon can be modelled as a superposition of a "blob-like" component and a "point-like" component. The blob-like component is a nucleon-sized component and the point-like component is a small-sized three-quark system. Because of its small size, the point-like configuration is responsible for the high x_B nucleon structure function behavior in the *EMC* region. So the point-like component should be suppressed in the nucleus.

The nucleon state in the nuclear medium can be as

$$|N\rangle_M = |N\rangle + (\epsilon_m - \epsilon_f)|N^\star\rangle . \tag{1.34}$$

In the above equation, $|N\rangle$ is the free-nucleon state that comes primarily from the blob-like component, while $|N^\star\rangle$ is primarily point-like. ϵ_f represents the relative strength of the point-like component in the free nucleon, and ϵ_m represents the relative strength of the point-like component when the nucleon is placed in the nuclear medium. If the nuclear interaction is represented by U, ϵ_m and ϵ_f are related by

$$\epsilon_m = \epsilon_f \frac{C_0}{C_0 - |U|} , \tag{1.35}$$

where C_0 is a constant. As $|U|$ increases, ϵ_m will be suppressed compared to ϵ_f.

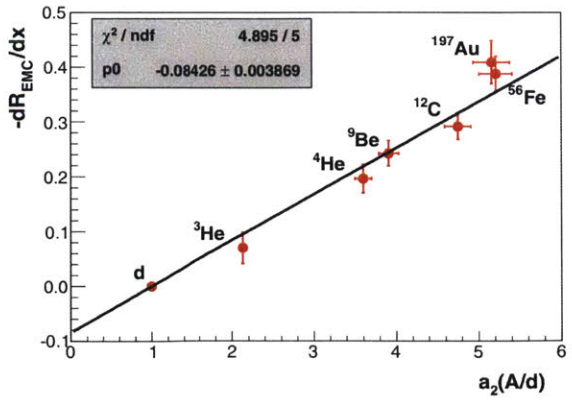

Figure 1-10: Observed linear correlation between the strength of the *EMC* effect (as characterized by the slope) and the SRC pair fraction probability ($a_2(A/d)$). This figure comes from Ref. [29].

1.5 This Work

This thesis presents experimental studies conducted at JLab on inclusive elastic scattering, QE scattering, and DIS. This thesis will present new DIS measurements of the *EMC* effect and QE measurements of SRC pair fraction probabilities conducted at Hall B at JLab. These measurements will be discussed in chapter 2. The DIS and QE measurements will be used to create a data-driven phenomenological model that presents a quantitative connection between the *EMC* effect and nucleon SRCs. In addition, chapter 3 will discuss an elastic electron-proton scattering experiment, the *GMp* experiment [30], that was performed in Hall A of JLab.

Chapter 2

Studying Bound Nucleon Stucture and SRCs with *CLAS*

We will now turn to a discussion of our cross-section ratio measurements in *CLAS* [31]. This analysis was performed as part of the *CLAS* Data-Mining initiative [32] on data taken during the *EG2c* experiment. The *EG2c* experiment took place in 2004 using an electron beam with a nominal beam energy of 5.014 GeV [33, 34]. The experiment used a specially designed target cell consisting of a 2 cm long cryogenic cell (filled with either liquid deuterium or liquid hydrogen) as well as a solid target located approximately 5 cm downstream [35]. A mechanical lever arm allowed one of the six solid target foils (^{12}C, thick or thin ^{27}Al, ^{56}Fe, ^{118}Sn, or ^{208}Pb) to be remotely placed into the beamline at a time.

The *EG2c* experiment operated with an open electron trigger design. This makes it possible to re-analyse the data, looking for physics not considered at the time the experiment was conducted. In this analysis, we present per-nucleon inclusive cross-section ratios for carbon, aluminum, iron, and lead to deuterium for both the Deep Inelastic Scattering (DIS) region and for high x_B Quasi-Elastic (QE) scattering. We use this data to extract *EMC* slopes and $a_2(A/d)$ values.

2.1 Experimental Setup

Continuous Electron Beam Accelerator Facility

The Continuous Electron Beam Accelerator Facility (CEBAF) at JLab provides continuous wave GeV electron beams for simultaneous use in multiple experimental halls [36]. Between the years 2000 and 2012, CEBAF operated with a maximum electron beam energy of approximately 6 GeV. At the beginning of 2009, construction began on the 12 GeV upgrade of the accelerator.

A schematic of the accelerator is shown in figure 2-1 following the 12 GeV upgrade. The beam is produced at the injector using a photocathode, and then accelerated using two anti-parallel superconducting linacs. The beam can be be recirculated up to four additional times prior to being sent to an experimental hall.

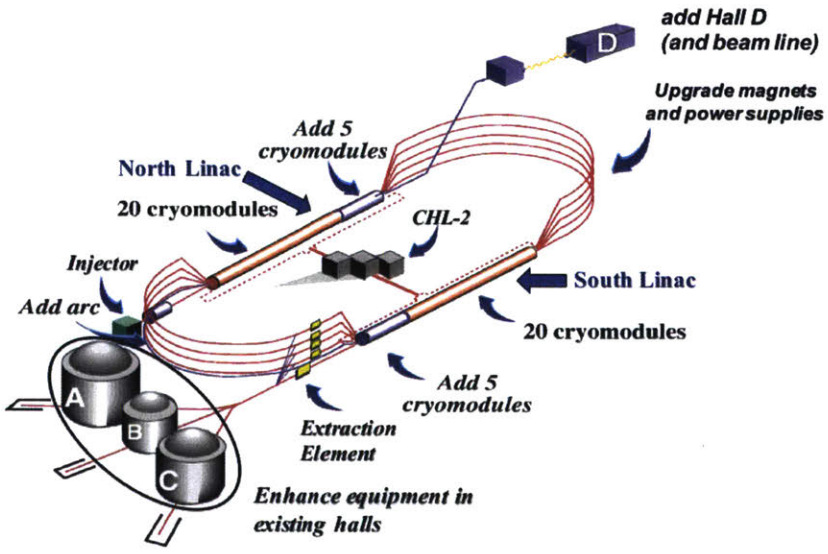

Figure 2-1: Schematic of the CEBAF site at Jefferson Lab after the 12 GeV upgrade. The parts of the accelerator site that were modified during the upgrade are highlighted in the figure.

The CLAS detector in Hall B at JLab

The *CLAS* detector was the primary detector used in Hall B during the 6 GeV CEBAF era [31]. The detector is a nearly 4π detector, which makes it ideal for studying multi-particle final states. It can detect charged particles with scattering angles between 8^o and 140^o. Neutral particles can be detected between 8^o and 75^o.

A schematic of the *CLAS* detector can be seen in figure 2-2. The beam enters from the left side in the figure, with the target placed somewhere near the center of the detector. The detector consists of six identical sectors. The main magnet consists of six superconducting coils which produce a toroidal magnetic field which is mostly constant in the azimuthal direction. A set of 3 drift chambers is used to determine the momentum, angles, and reaction vertices for charged particles. Scintillator paddles are used for time-of-flight measurements and occasionally for triggering. A gas cherenkov detector and electromagnetic calorimeter are used to perform particle identification for certain particles. A large-angle calorimeter is also present in 2 of the sectors.

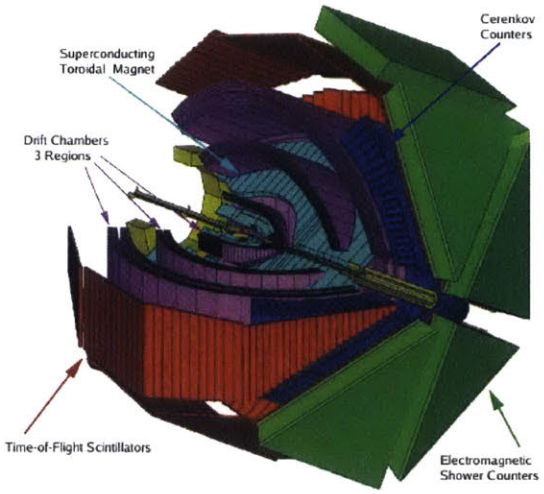

Figure 2-2: Schematic of the *CLAS* detector.

Although mostly used for exclusive and semi-inclusive studies, the *CLAS* detector can also be used to study inclusive electron scattering. For the data under study here, the *EG2c* data, an open electron trigger was used, allowing for inclusive cross-section

ratio measurements. The gas cherenkov and electromagnetic calorimeter were both in the trigger during the EG2 experiment, and they are limited to the forward direction. So electrons can be detected up to scattering angles of approximately 55^o.

Target for the EG2 Experiment

The *EG2c* experiment used a specially-designed target cell capable of placing two targets simultaneously in the beam-line [35]. This allowed for a good control of many systematic uncertainties in the extraction of inclusive cross-section ratios. The first target the beam interacts with is the cryogenic target cell (which was filled with either liquid hydrogen or liquid deuterium). This cell had a length of 2 cm [37]. The beam would then strike the solid target. The available solid targets (all in natural abundances) were as follows: carbon, thin-aluminum, thick-aluminum, iron, tin, and lead. A picture of the target holder is shown in figure 2-3. Table 2.1 lists each target along with its respective thickness.

For this analysis, we make use of the carbon, thick-aluminum, iron, and lead targets. Only a small amount of data was collected for the thin-aluminum and tin targets. In addition, we found that the tin target was not fully inserted into the beamline when data was collected from it.

Target	Thickness [mm]	Areal Density [g/cm^2]
Cryotarget	20	0.324
Carbon	1.72	0.300
Thin-Aluminum	1.5×10^{-3}	≈ 0.0
Thick-Aluminum	0.58	0.1566
Iron	0.4	0.315
Tin	0.31	0.228
Lead	0.14	0.159

Table 2.1: Lengths and areal densities of all EG2 targets along the beam direction. The density of the carbon target was remeasured after the experiment and found to have a slightly different value than the value given in Ref. [35]. This new value is consistent with the measured relative electron yields [38].

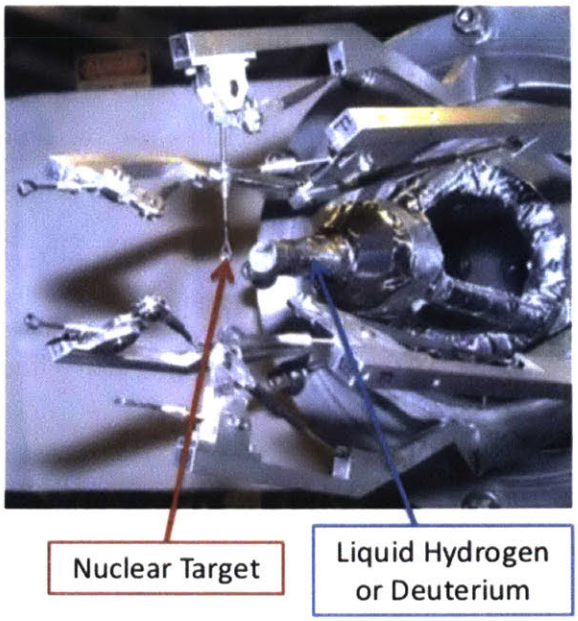

Figure 2-3: Photo of the EG2 target holder. The locations of the cryogenic target and solid target are stated on the figure.

2.2 Electron Identification and Reconstruction

Electron Particle Identification

For the *EG2c* dataset, calibrations were performed shortly after the data was collected. These calibrations convert the raw detector hits and signals for each particle candidate into usable quantities like momentum and energy deposited in the calorimeter [39]. So our work begins with selecting the good electrons out of the set of triggering events. In this analysis, we use the same electron particle identification (PID) cuts for both the DIS and QE regions. This is justified because these exact same cuts were used successfully for an *EG2c* DIS analysis [39] and an *EG2c* QE analysis at high x_B [40].

We will give a brief overview of the applied cuts. Electrons candidates are required to meet the following criteria: they must be the particle that triggered the detector; they must leave a negatively charged track in the drift chamber; and they must have corresponding hits in the scintillator, cherenkov, and calorimeter detectors.

To determine whether an electron candidate is in fact a good electron (and not,

for example, a negative pion), we apply several cuts. First, as shown in figure 2-4, a minimum number of photoelectrons is required in the cherenkov counter. Second, the hit location in the calorimeter can not be too close to the detector edge (figures 2-5a and 2-5b). Third, a minimum energy deposition is required in both the inner and the outer layers of the calorimeter (figure 2-6). Finally, a correlation must be observed between the amount of energy deposited in each layer of the calorimeter and the momentum of the particle as determined by the drift chamber (figures 2-7 and 2-8).

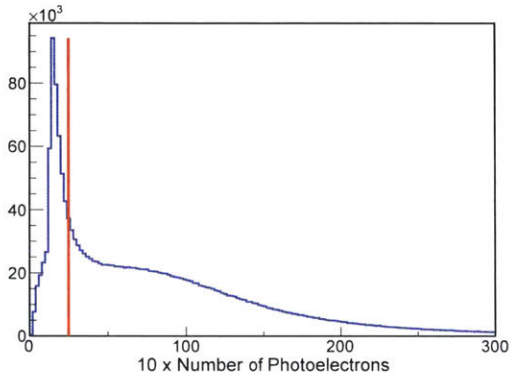

Figure 2-4: Number of photoelectrons deposited in the cherenkov counter for electron candidates. We require that the candidate particles produce at least 2.5 photoelectrons to be considered good electrons.

Electron Vertex Corrections

Since multiple targets were present in the beamline for much of the *EG2c* run period, it is important to correctly reconstruct the reaction vertex. During the experiment, the incident beam was transversely offset from the ideal beamline by approximately 2-3 mm. Since the targets' transverse thickness is larger than this offset, the only effect of the offset is that the *CLAS* software will reconstruct the reaction vertex incorrectly. (This offset will not affect the reconstructed momentum vectors.) As discussed in Ref. [41], the vertex is incorrectly reconstructed in a known way, allowing for an easy correction. The reconstructed electron vertex for a carbon-deuterium run is shown in figure 2-9. The carbon foil should be located at -25 cm, but a clear sector-to-sector

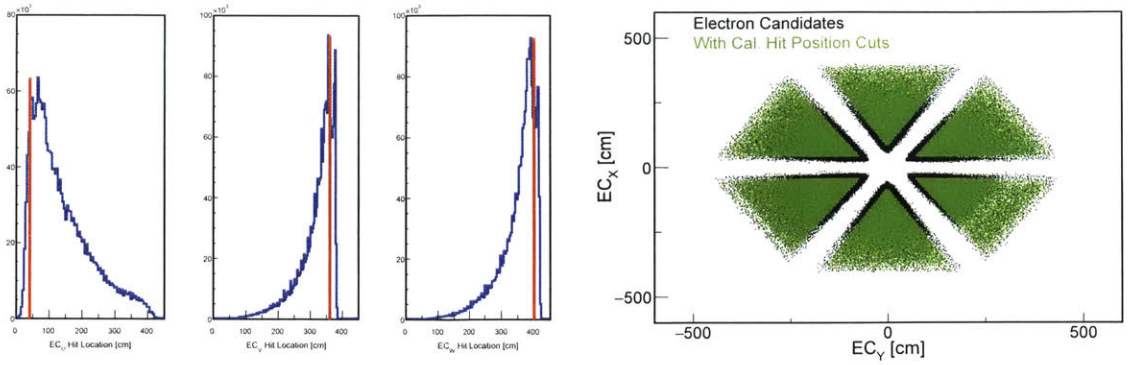

(a) (b)

Figure 2-5: Electron candidate hit locations in the electromagnetic calorimeter. The coordinate systems shown are defined relative to the *CLAS* detector. We apply the following cuts: $EC_U > 40\ cm$, $EC_V < 360\ cm$, and $EC_W < 395\ cm$. (a) Electromagnetic Calorimeter U, V, and W hit locations. (b) Electromagnetic Calorimeter X vs. Y hit locations. The green events are the electron candidate events which pass the EC_U, EC_V, and EC_W cuts.

dependence is observed. In order to correct this, we follow the procedure in Ref. [41]. That is, we look at the reconstructed carbon foil vertex (Z_{meas}) as a function of the azimuthal angle for a specific polar angle. Then we fit this dependence using the appropriate function (figure 2-10):

$$Z_{Fit}(\phi, \theta) = Z_0 - b \cdot \cos(\phi - \phi_0) / \tan\theta\,, \tag{2.1}$$

where Z_0, b, and ϕ_0 are the fit parameters, and θ and ϕ are the electron polar and azimuthal angle, respectively.

Although this fit describes the general features of the incorrect vertex reconstruction, there is still an issue within each sector. Our hypothesis is that this has to do with the polar angle being not perfectly reconstructed (as described in section 2.3). In any event, we developed the following ad-hoc procedure to correct the residuals. Noting that the true foil position is at -25 cm relative to the hall center, we can take into account our previous fit and define the corrected electron vertex as

$$Z_{corr} = (Z_{meas} - Z_{Fit} - 25) \times f(\phi) \times g(\theta)\,, \tag{2.2}$$

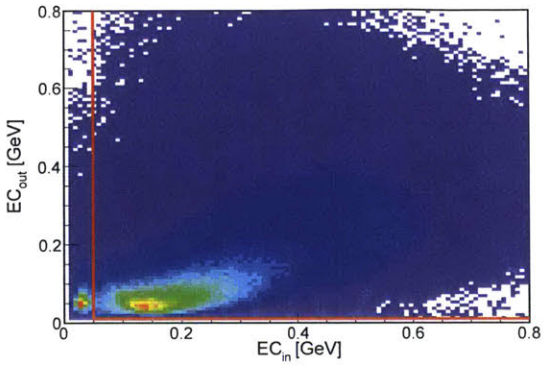

Figure 2-6: Energy deposited in the two layer of the electromagnetic calorimeter. We require the energy deposited in the inner layer to be greater than 0.05 GeV and the energy deposited in the outer layer to be greater than 0.01 GeV.

where $f(\phi)$ and $g(\theta)$ are low (3^{rd}) order polynomials. This type of extraction is used in various momentum correction procedures at *CLAS* [42]. To determine $f(\phi)$ and $g(\theta)$, we substitute the true foil vertex into the left side of equation 2.2 to get

$$\frac{-25}{Z_{meas} - Z_{Fit} - 25} = f(\phi) \times g(\theta) \tag{2.3}$$

First $f(\phi)$ is determined, as shown in figure 2-11a; then, for every event, $g(\theta)$ is solved for in equation 2.3. This is plotted and fit as a function of θ, as shown in figure 2-11b.

The corrected electron vertex is used for the remainder of the analysis. It is plotted in figures 2-12 and 2-13.

Electron Fiducial Cuts

The electron fiducial cut is used to remove events from regions where the detection efficiency and acceptance is rapidly changing. The basic idea is to look for the range of azimuthal angles at a given polar which give a stable electron yield. A continuous parametrization as a function of polar angle can then be developed.

In this analysis, we use the electron fiducial cuts previously developed for *EG2c* [39, 40]. In figure 2-14a, we plot the scattered electron polar vs. azimuthal angle from the deuterium target prior to the fiducial cuts; in figure 2-14b, we plot the same

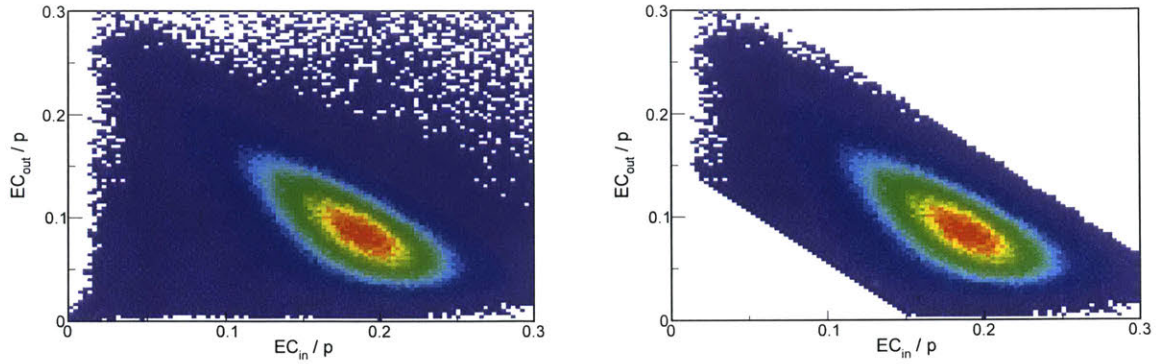

(a) (b)

Figure 2-7: (a) Momentum-normalized energy deposited in each layer of the electromagnetic calorimeter for electron candidates after applying the cuts described in figures 2-4 - 2-6. (b) Momentum-normalized energy deposited in each layer of the electromagnetic calorimeter after requiring a correlation between the energy deposition and the momentum.

quantities after applying the fiducial cuts.

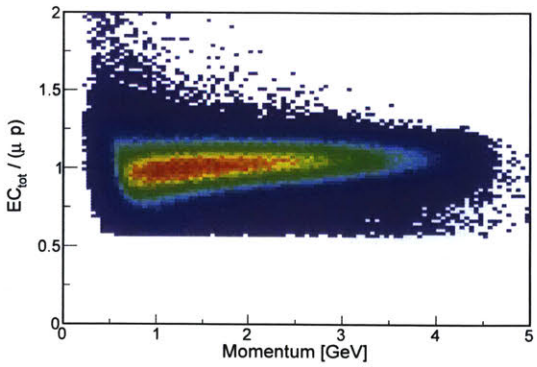

Figure 2-8: Total momentum and sampling-fraction normalized energy deposition in the calorimeter as a function of momentum after applying all electron PID cuts. The sampling fraction μ is equal to 0.271.

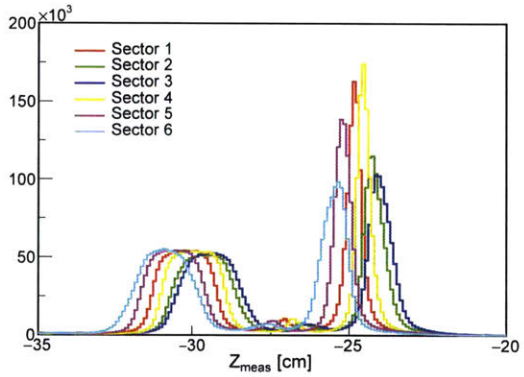

Figure 2-9: Reconstructed electron vertex for a carbon-deuterium run.

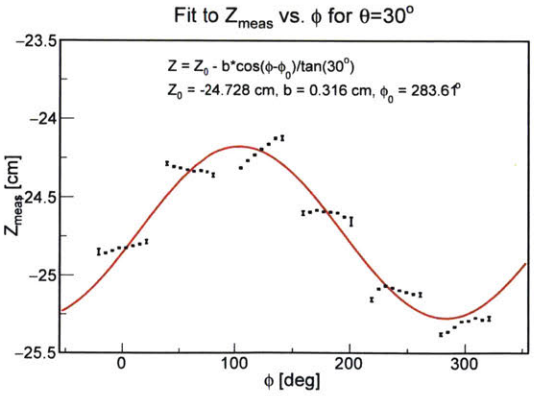

Figure 2-10: Sinusoidal fit to the carbon foil data. The data is fit at a fixed polar angle. We refer to the results of this fit in equations 2.2 and 2.3.

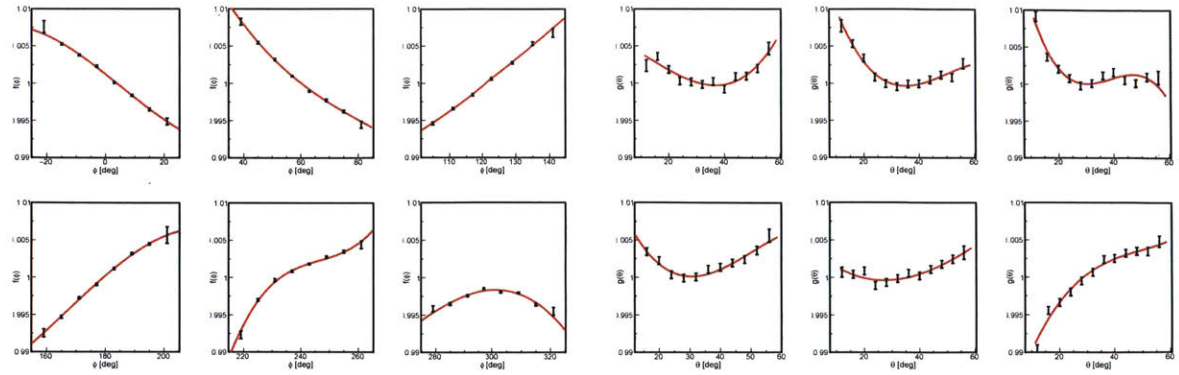

(a) (b)

Figure 2-11: (a) Determination of $f(\phi)$ for each sector. The functions are 3^{rd} degree polynomials. (b) Determination of $g(\theta)$ for each sector. The functions are 3^{rd} degree polynomials.

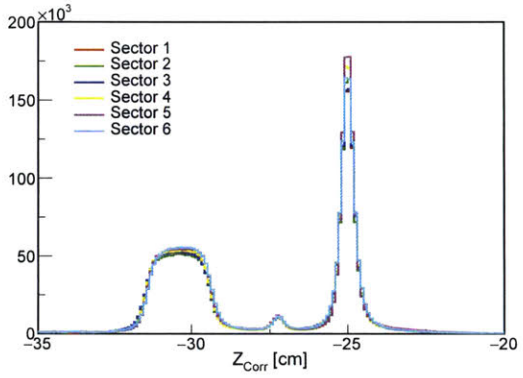

Figure 2-12: Reconstructed electron vertex after applying the corrections detailed in the text.

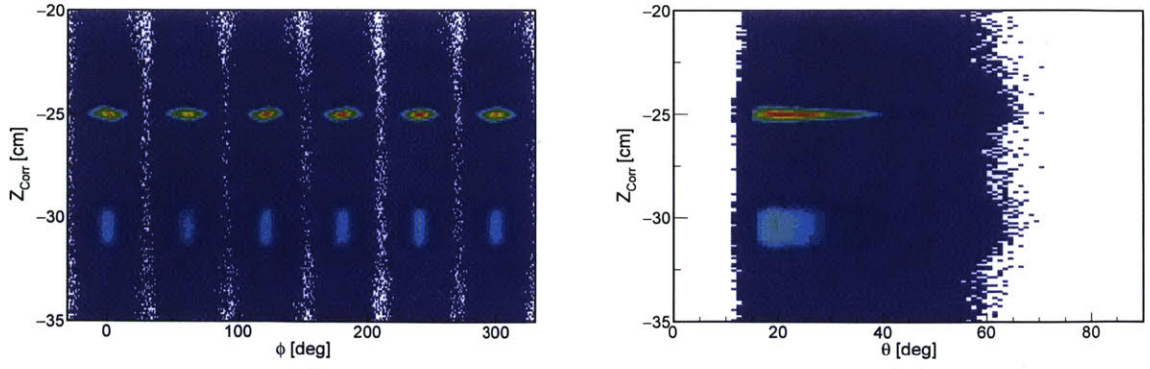

(a) (b)

Figure 2-13: (a) Corrected electron vertex vs. ϕ. (b) Corrected electron vertex vs. θ.

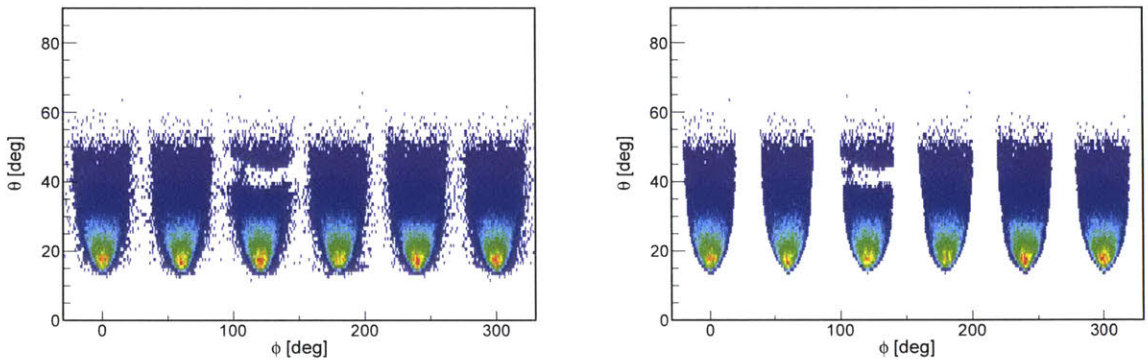

(a) Before fiducial cuts.

(b) After fiducial cuts.

Figure 2-14: Scattered electron θ vs. ϕ for a portion of the data collected on the deuterium target.

2.3 Kinematic Corrections

There exist several potential imperfections which can cause the incorrect reconstruction of particles' momentum vectors. Incomplete knowledge of the torus magnetic field distribution will affect the reconstruction of the momentum. Misalignment of the drift chambers, wire sag, limited knowledge of wire feed-through locations, etc. can affect both the reconstructed angles and momentum. The originally developed empirical momentum corrections assumed the angles to be reconstructed correctly and used e-p elastic scattering to correct the electron momentum [42]. After additional studies [43] found that the angles may not be reconstructed perfectly, more complex correction schemes were developed incorporating all the effects described above [44, 45].

Here we first correct the beam energy using information obtained from the Hall A arc. Then we correct the electron and proton polar angles using e-p elastic scattering, based on the technique used in Ref. [46]. For DIS events, we use radiative elastic events from the hydrogen target to correct the magnitude of the electron momentum [47]. Finally, for QE events, we estimate the magnitude of the momentum correction by using the deuterium target. No fiducial cuts are applied in this section so that the fits can cover a larger range.

2.3.1 Proton Identification and Reconstruction

Proton Particle Identification

Even though we are making an inclusive electron scattering cross-section ratio measurement, we use protons for the kinematic corrections discussed in this section. We therefore need to correctly reconstruct proton events prior to performing these corrections.

The procedure to reconstruct protons is identical to the one used for a prior *EG2c* analysis [40]. For positive particles, we can determine the momentum of the particle in the drift chamber; for a given momentum, we can calculate the time when a proton should arrive at the scintillator counters. If the particle arrives at the scintillator

at the calculated time, it is most likely a proton. We create a quantity called the corrected time-of-flight for the proton defined as

$$TOF_{corr} = T^P_{SC} - S.T. - T^P_{Calc}\,, \tag{2.4}$$

where T^P_{SC} is the measured time of the proton candidate hitting the scintillator, $S.T.$ is the event start time calculated using the scattered electron, and T^P_{Calc} is the calculated time-of-flight from the vertex to the scintillator for a given path-length and momentum assuming the particle is a proton. In figure 2-15a, we plot this corrected time-of-flight for all positive particles. Based on equation 2.4, the protons should have a corrected time-of-flight equal to zero.

In order to select protons, the data is binned in momentum. For every momentum bin, a Gaussian fit is performed and the standard deviation is determined. Then events within $\pm 2\sigma$ are kept, using a continuous parametrization as a function of momentum. The cut parameters are taken from the previous *EG2c* analysis [40]. The events remaining after the proton PID cuts are shown in figure 2-15b. Figure 2-16 shows the reconstructed mass for all positive particles before and after the proton PID cuts.

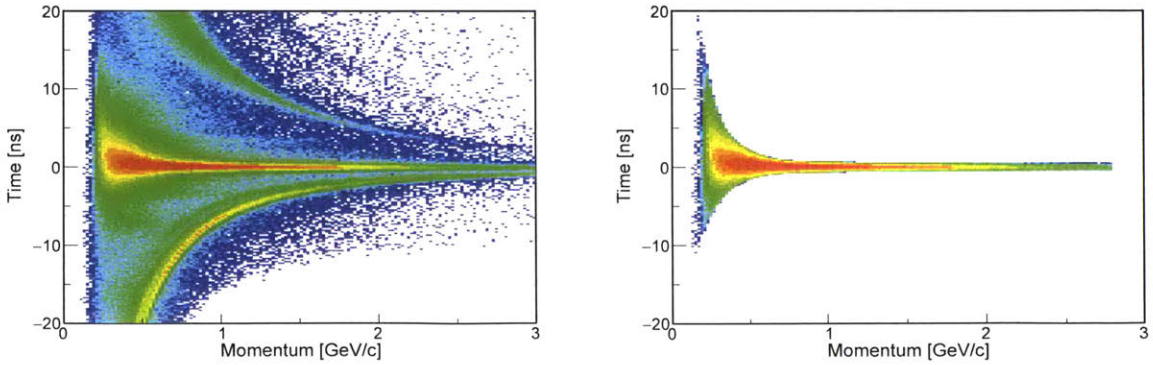

(a) (b)

Figure 2-15: Corrected time-of-flight vs. momentum. The z-axes are in log scale. (a) All positive particles from the iron target. (b) Events that pass the proton PID cuts.

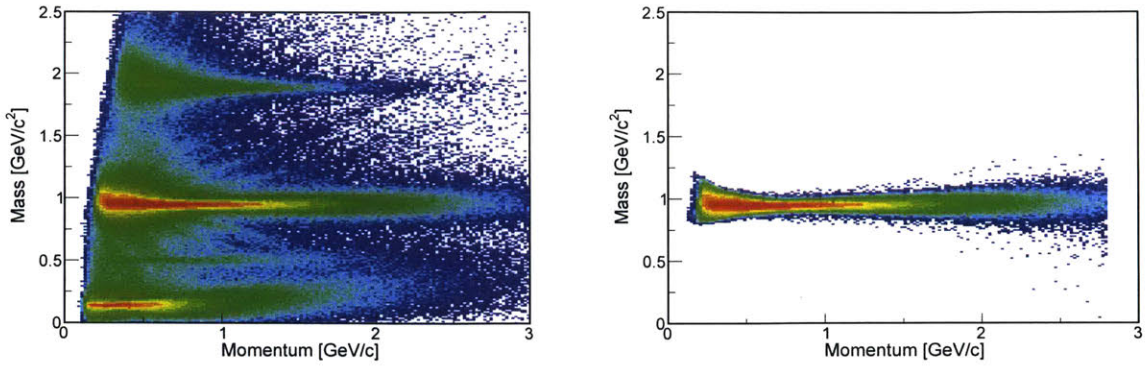

(a) (b)

Figure 2-16: Reconstructed mass vs. momentum. The z-axes are in log scale. (a) All positive particles from the iron target. (b) Events that pass the proton PID cuts.

Proton Vertex Corrections

The proton vertex corrections are done in exactly the same way as the electron vertex corrections described above. Figure 2-17a shows the reconstructed proton vertex before the corrections, and figure 2-17b shows the reconstructed proton vertex after the corrections.

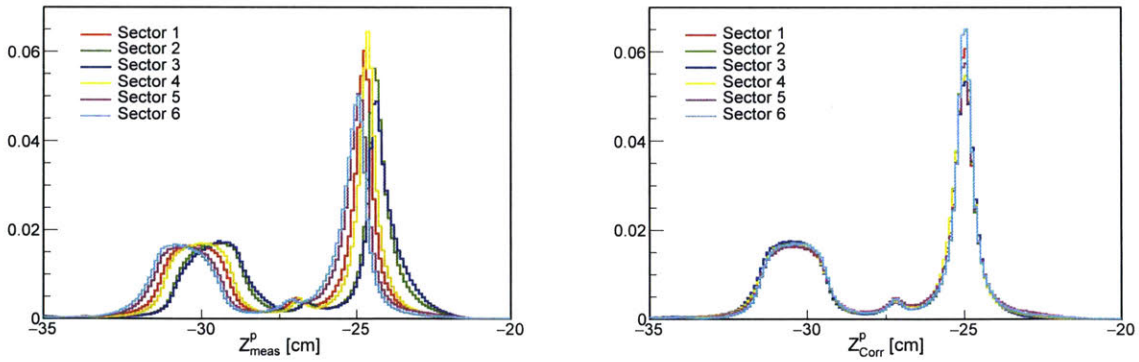

(a) (b)

Figure 2-17: (a) Proton reconstructed vertex before vertex corrections for carbon-deuterium data. The curves are arbitrarily normalized to the same integral. (b) Proton reconstructed vertex after vertex corrections for carbon-deuterium data. The curves are arbitrarily normalized to the same integral.

When performing the kinematic corrections we do not cut directly on the corrected proton vertex to select the relevant target; rather we cut on the corrected electron

vertex and the difference between the corrected electron and proton vertices (figure 2-18).

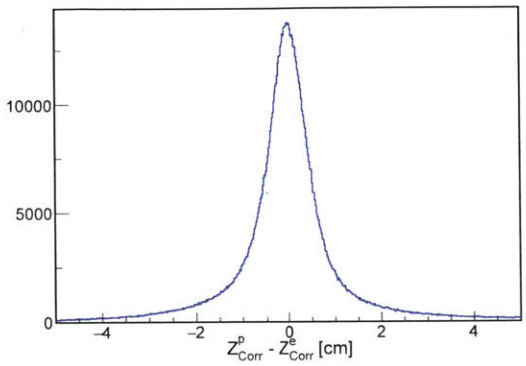

Figure 2-18: Proton corrected vertex minus electron corrected vertex. For the kinematic corrections described here, the absolute value of the vertex difference is required to be less than 2 cm.

Proton Ionization Energy Loss Corrections

Using the *CLAS* monte-carlo simulation (*GSIM*), we can calculate the proton ionization energy loss correction. In figure 2-19, we plot the true proton energy minus the reconstructed proton energy vs. the reconstructed proton momentum. From this, we develop a continuous parametrization for the energy loss correction as a function of momentum. It was found that the same correction can be used for the liquid deuterium and the liquid hydrogen targets.

2.3.2 Electron Beam Energy

For the *EG2c* run period, the set electron beam energy was 5.014 GeV. However, it is known that the set energy during 6 GeV *CEBAF* running was not equal to the true energy [48]. Since Hall A was in operation during the same time, the beam energy can be determined using the Hall A arc measurements. Hall A ran at both 2^{nd} pass and 4^{th} pass during this time. They measured the following beam energies:

$$Injector + 4 \times Accelerator = 4019.5\ MeV\ (Hall\ A\ 4^{th}\ Pass)$$

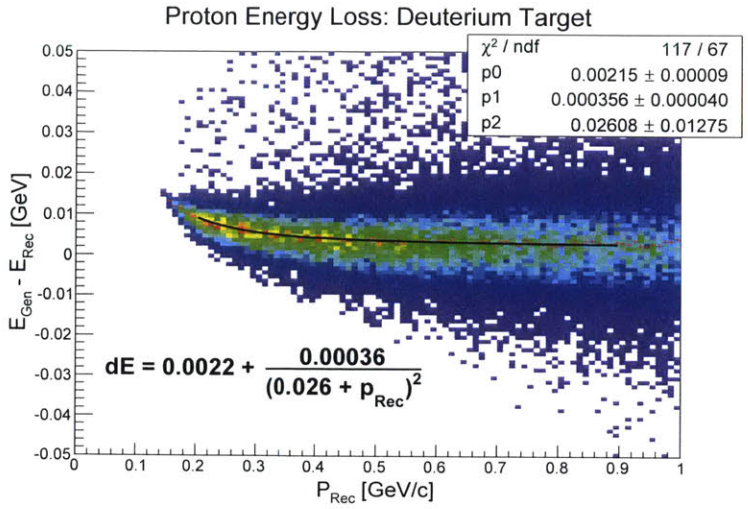

Figure 2-19: Proton ionization energy loss corrections as determined by the simulation. The parameters in this plot can be used for both the liquid deuterium and hydrogen targets.

$$Injector + 2 \times Accelerator = 2039.7\ MeV\ (Hall\ A\ 2^{nd}\ Pass)$$

From this, we can determine what the beam energy in Hall B (operated at 5^{th} pass) should be. We calculate the following beam energy:

$$EG2c\ Energy = 5009.4\ MeV$$

This is the beam energy we use for the remainder of this analysis. As can be seen in figure 2-20, for H(e,e') events, using this energy brings the elastic peak closer to the proton mass.

2.3.3 Scattering Angle Corrections

To correct the reconstructed polar angles, we apply a procedure similar to that done in Ref. [46]. We first select events from the hydrogen target where the scattered electron and one proton were detected. We take events where the invariant mass, W, reconstructs to within the elastic peak (figure 2-21a). Then we require the detected electron and proton to be coplanar (figure 2-21b). With these two cuts, we select

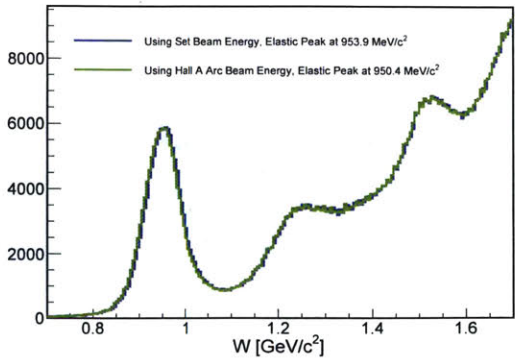

Figure 2-20: Reconstructed invariant mass for H(e,e') events using the two different beam energies.

elastic scattering events with potentially some soft photon radiation.

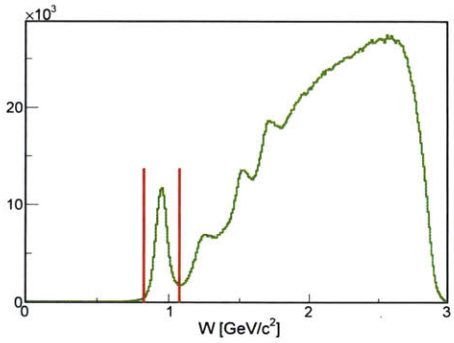

(a) Reconstructed invariant mass for H(e,e'p) events, and the selection of the elastic peak (within red lines).

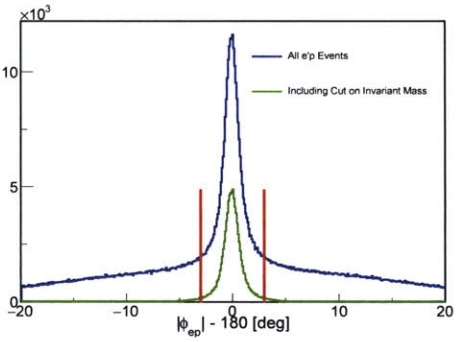

(b) Difference between the absolute value of the electron and proton azimuthal angles minus 180 degrees. We select events between the red lines.

Figure 2-21: Elastic selection cuts.

Next, for elastic scattering, we can calculate the beam energy using the electron and proton angles only [43] as

$$E_0 = \frac{M_p}{1 - \cos\theta_e}\left(\cos\theta_e + \frac{\sin\theta_e}{\tan\theta_p} - 1\right), \tag{2.5}$$

where M_p is the mass of the proton and θ_e and θ_p are the angles of the electron and proton, respectively. This is the important point - the reconstruction of the beam energy is done solely from the two angles, so any mis-reconstruction of the beam energy will have to be because of angular mis-reconstruction. In figures 2-22 and

2-23, we show the ratios of the true energy to the energy reconstructed from the angles.

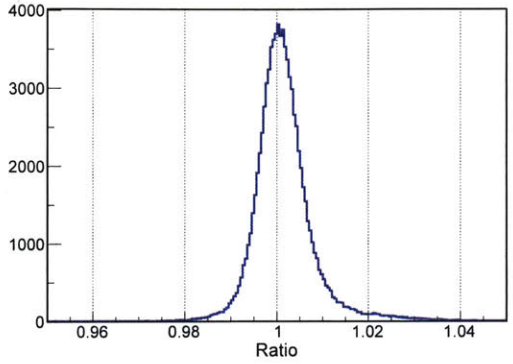

Figure 2-22: True beam energy divided by the energy determined from the electron and proton polar angles.

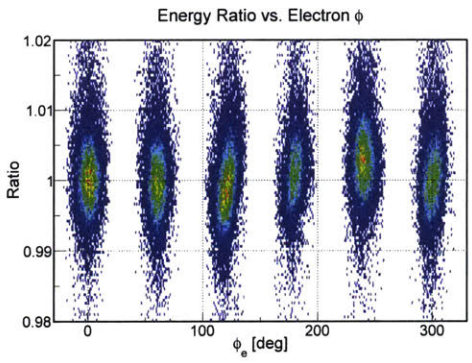

(a) True beam energy divided by the energy determined from the electron and proton polar angles vs. the electron azimuthal angle.

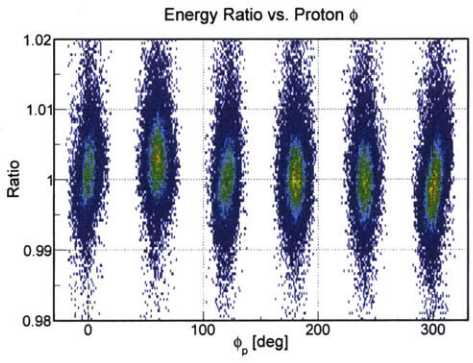

(b) True beam energy divided by the energy determined from the electron and proton polar angles vs. the proton azimuthal angle.

Figure 2-23: Two-dimensional beam energy reconstructed from angles.

Under certain reasonable assumptions [46], the mis-reconstruction should be the same for all types of particles. So, for every event, we can find the distance of closest approach to the electron-proton angle dependency curve for the true energy (figure 2-24). This will give us two angle correction values for every event, one for the electron and one for the proton. Since we assume the form of the correction is the same for both types of particles, the angles lose their individual identities here, and we roll both into a general polar angle for performing the correction. The general polar angle is the combined set of both the electron and proton polar angles. That is, for each

event the general polar angle variable is set twice, to both the electron polar angle and the proton polar angle.

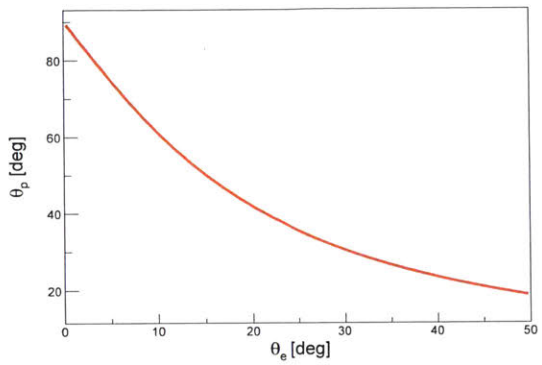

Figure 2-24: Relationship between proton and electron scattering angles for elastic e-p scattering at the true *EG2c* beam energy (equation 2.5). Every selected e-p event, will lie off this curve. By determining the point of closest approach, we can extract a correction to both the electron and proton angles for each event.

In figure 2-25, we show the difference between the measured and calculated general polar angle vs. the measured general polar angle. Note how there are two groups of data in this plot, the lower angles coming from the electron and the larger angles coming from the proton. For every sector, we look at the difference between the calculated and measured general polar angles vs. ϕ (figure 2-26a), and we fit the difference with a 3^{rd} order polynomial. After applying this correction to both the electron and proton reconstructed angles, we see no dependence on ϕ (figure 2-26b). We checked for any dependence on θ (figure 2-27), and saw very little; so, we made the correction only a function of ϕ. In figures 2-28a and 2-28b, we show the reconstructed energy using the corrected angles.

The correction should be valid for all types of particles. Since we see very little dependence of the correction on θ, it may also be valid for all polar angles. As we have events with polar angles between 12 and 55 degrees in the fit, we can at least say that the fit is valid in this range. For the inclusive (e,e') analysis performed in this thesis, the scattered electron's polar angle is never outside the fit range.

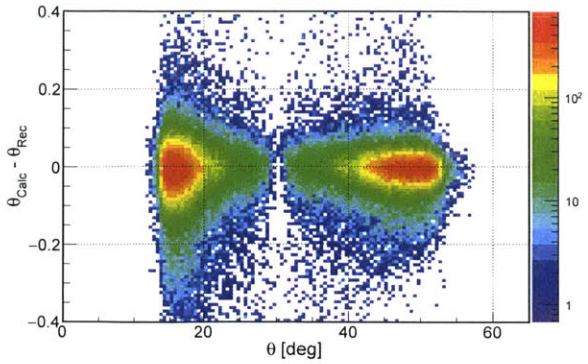

Figure 2-25: The difference between the measured and calculated general polar angle vs. the general polar angle.

2.3.4 Momentum Corrections

Momentum Corrections for DIS Events

Now that we have corrected the polar angles, we can use the corrected electron and proton angles to calculate any quantity for elastic scattering. Part of the analysis in this thesis, however, takes place in the DIS region. As is well known, many of the events that reconstruct with large invariant mass (W) come from the so-called radiative elastic tail [49]. If we can select H(e,e'p)X events where the electron reconstructs as a DIS event, but in reality is an elastic event where the incoming electron radiated a hard photon, we can calculate what the true electron momentum should be as

$$E_f = \frac{E_i}{1 + E_i(1 - \cos\theta_e)/M_p}\,, \tag{2.6}$$

where E_f is final electron energy, and E_i is the initial electron energy. Note that E_i is not equal to the beam energy here since the initial electron must radiate prior to the elastic scattering to perform the correction, and E_i must be calculated from equation 2.5.

To select the required events, we first look at the reconstructed missing mass when we detect an electron and proton for different invariant mass (W) regions. The missing mass for H(e,e'p)X events is defined as the mass of the undetected particles (i.e. the mass of X). As can be seen in figure 2-29, the missing mass resolution

is degraded at large W. So, in order to select radiative elastic events where the initial electron radiated, we first require the electron and the proton to be coplanar (figure 2-30). From figure 2-30, we estimate the inelastic contribution within the cut to be approximately 8-10%. In order to reduce this background and remove events where the scattered (as opposed to the initial) electron radiated, we require the missing momentum (i.e. the momentum of X) to be along the direction of the beamline (figure 2-31). Now, assuming elastic scattering after radiation, we calculate the initial electron momentum and compare that to the sum of the scattered electron and proton momentum along the beamline (figure 2-32). We require this difference to be less than 100 MeV/c.

With the events selected, we consider the missing momentum vs. the invariant mass (figure 2-33). For the events passing all our cuts, we can see the radiative tail rising at high invariant mass. Then in figure 2-34, we plot the scattered electron momentum vs. polar angle for the radiative elastic events with large invariant mass. We can see that these events cover the same area of phase-space as the inelastic inclusive events.

For every event, we calculate the scattered electron momentum from the corrected electron and proton angles using equation 2.5. We then define the following momentum correction functions:

$$\frac{P_{e,calc}}{P_{e,meas}} = f(\phi) \times g(\theta)\,, \tag{2.7}$$

where $f(\phi)$ and $g(\theta)$ are once again 3^{rd} order polynomials; and the justification for this factorization comes from previous momentum-correction studies [42]. In each sector, we bin the data in ϕ and determine $f(\phi)$ (figure 2-35a). Then we divide equation 2.7 by $f(\phi)$ and bin the data in θ to determine $g(\theta)$ (figure 2-35b). After applying the correction, we observe no dependence of the ratio on ϕ and θ (figures 2-36a and 2-36b). We compare the square of the missing mass before and after the momentum corrections in figure 2-37.

The last question we consider is whether these corrections can be used for the solid targets, which were located several cm downstream of the cryotarget. First

note how in figure 2-35a, the ratio is primarily above unity. This occurs because no ionization energy loss corrections were applied for the electrons prior to performing the momentum corrections discussed here. The ionization energy loss correction is therefore rolled into the momentum correction. By using the *CLAS* monte-carlo simulation, *GSIM*, we were able to determine that the electron ionization energy loss is equivalent in all the solid and liquid targets. (This is because almost all of the energy loss occurs in the material surrounding the targets.) So ionization losses can be included in the general momentum correction. Next, we bin the hydrogen target as shown in figure 2-38, and look at the correction for the two regions. In figures 2-39a and 2-39b, we see that the corrections look qualitatively similar for the two bins, even though the centers of the bins differ by about 2 cm. This provides some justification for using the obtained correction factors for the solid targets.

Momentum Corrections for QE Events

For our analysis of quasi-elastic (QE) scattering, we are interested in events with $x_B > 1$, and the hydrogen data obviously does not extend into this part of the phase-space. In figure 2-40, we plot the missing mass for large x_B D(e,e'p)X events, and observe a clear peak at the nucleon mass. For the QE events in that peak, assuming that the scattered electron angles, the proton angles, and the proton momentum are reconstructed correctly, we can calculate the scattered electron momentum [50, 51]. We apply conservation of energy and momentum and solve for the final electron momentum using the following equations:

$$E_e + M_D = E_{e'} + E_p + E_n \,, \tag{2.8}$$

$$p_{z,e} = p_{e'} \cos\theta_e + p_{z,p} + p_{z,n} \,, \tag{2.9}$$

$$0 = p_{e'} \sin\theta_e \cos\phi_e + p_{x,p} + p_{x,n} \,, \tag{2.10}$$

$$0 = p_{e'} \sin\theta_e \sin\phi_e + p_{y,p} + p_{y,n} \,. \tag{2.11}$$

In the above equations, $E_{e'} = p_{e'}$; M_D is the mass of the deuteron; and $p_{p(n)}$ is the momentum of the proton (neutron) remaining in the final state. In figure 2-41, we plot the reconstructed electron momentum and the electron momentum calculated using the above equations for events in the QE peak. The difference between the calculated and measured momentum for every QE event is then shown in figure 2-42. By looking at the mean value of the difference in each sector, we see that at most the electron momentum is incorrectly reconstructed by 20 MeV/c.

Assuming a 4 GeV/c scattered electron, a 20 MeV/c mis-reconstruction will cause a shift of 0.025 in x_B at $x_B = 1$. At $x_B = 1.5$, a 20 MeV/c mis-reconstruction will cause a shift in x_B of 0.037. This mis-reconstruction of x_B can have a small effect on our final QE cross-section ratios, and will be taken into account in the systematic uncertainties.

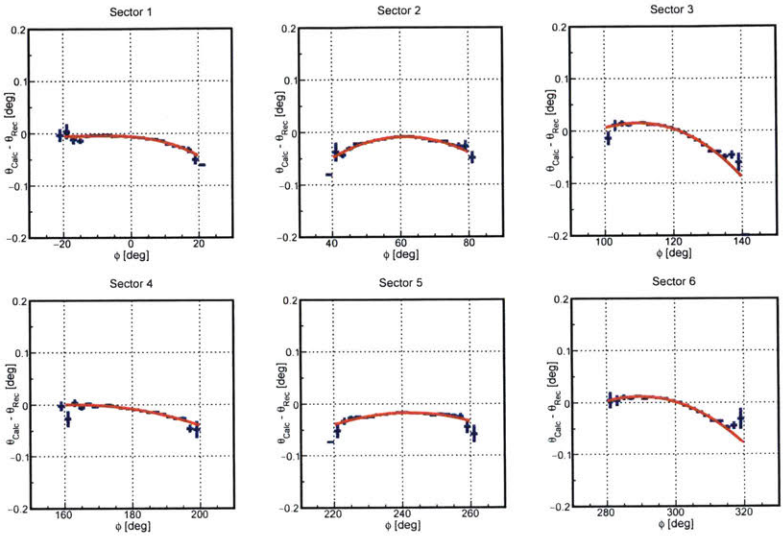

(a) Before Corrections

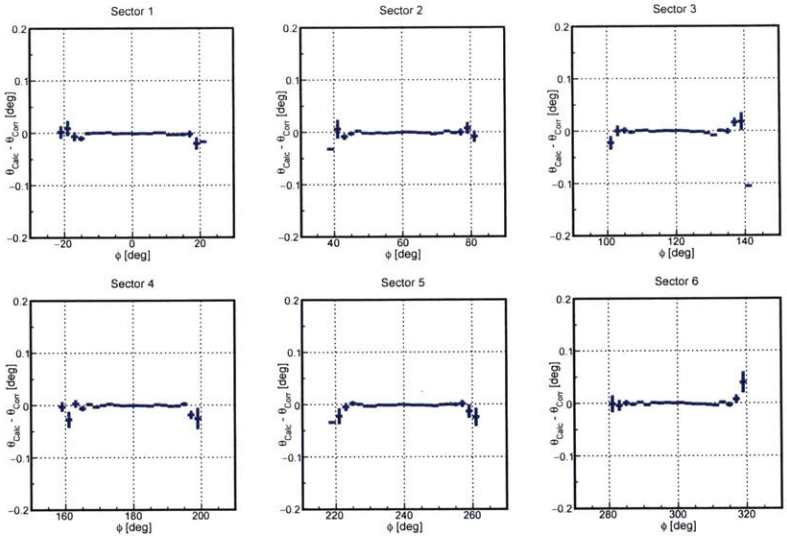

(b) After Corrections.

Figure 2-26: The difference between the measured and calculated general polar angle vs. the general azimuthal angle. We fit each sector with a 3^{rd} order polynomial. The top plot shows before applying any corrections; the bottom after applying the determined correction to both the electron and proton angles.

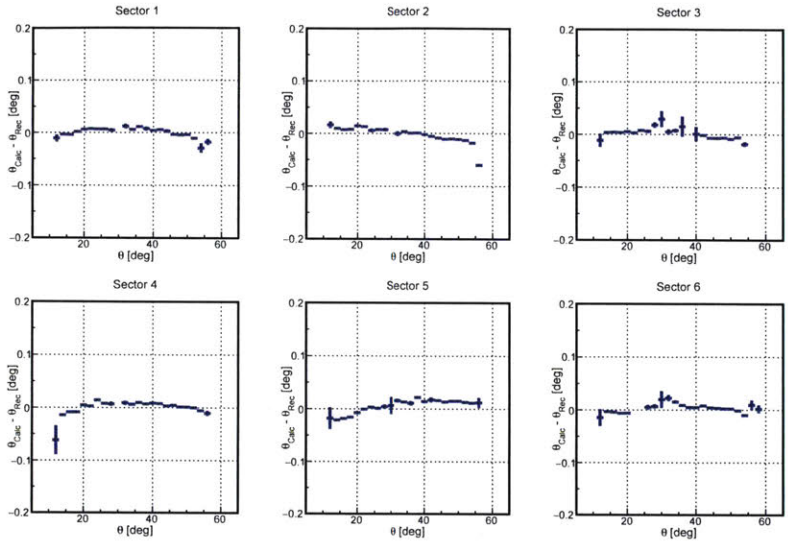

Figure 2-27: The difference between the measured and calculated general polar angle vs. the general azimuthal angle after applying the extracted azimuthal correction to both the electron and proton events. Since we see very little dependence on the polar angle, we don't make any fit here.

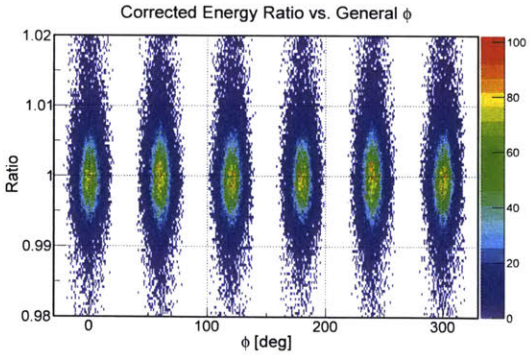

(a) True beam energy divided by the energy determined from the electron and proton polar angles vs. the general azimuthal angle after applying the polar angle corrections.

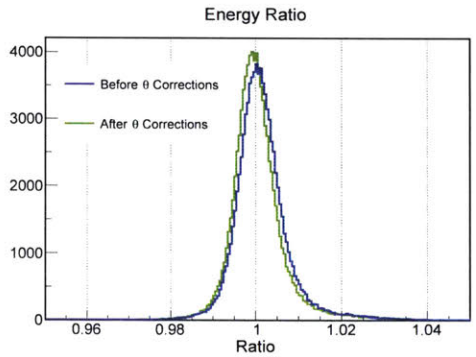

(b) Comparison of true beam energy divided by the energy determined from the electron and proton polar angles before and after applying the polar angle corrections.

Figure 2-28: Beam energy reconstructed from angles after corrections.

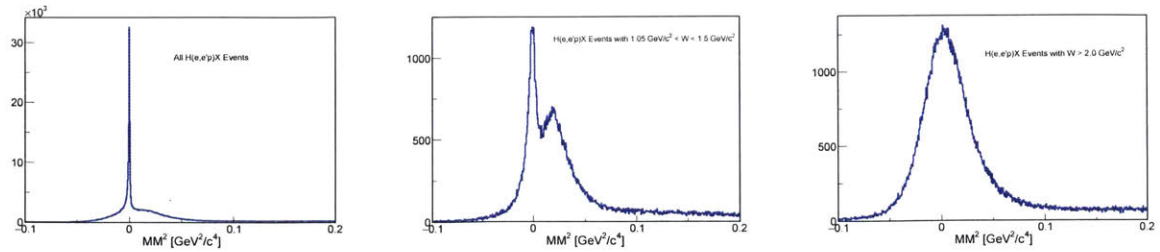

(a) (b) (c)

Figure 2-29: Square of the missing mass for H(e,e'p)X events. (a) All events. (b) Events with invariant mass near the 3-3 resonance. (c) Events with large invariant mass.

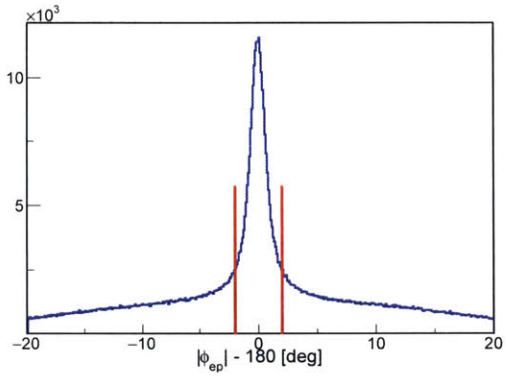

Figure 2-30: Absolute value of the difference between the electron and proton azimuthal angles minus 180 degrees. We require this quantity to deviate from zero by less than 2^o. The background under the peak is reduced by applying additional cuts.

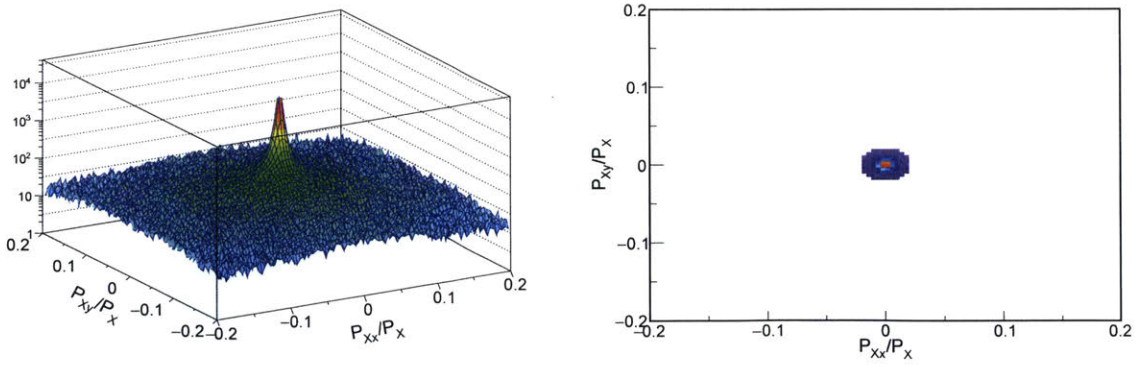

(a) (b)

Figure 2-31: Fraction of the missing momentum in the directions transverse to the beamline. (a) All H(e,e'p)X events. (b) Selected cut on the missing momentum direction. Less than 2% of the missing momentum is allowed to be in a direction transverse to the beamline.

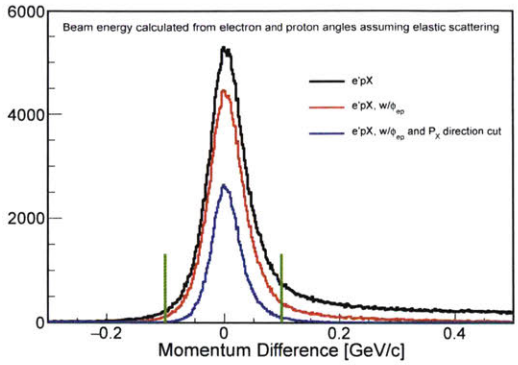

Figure 2-32: Difference between the initial electron momentum reconstructed from the electron and proton angles and the sum of the scattered electron and proton momentum along the beamline. The absolute value of this difference is required to be less than 100 MeV/c.

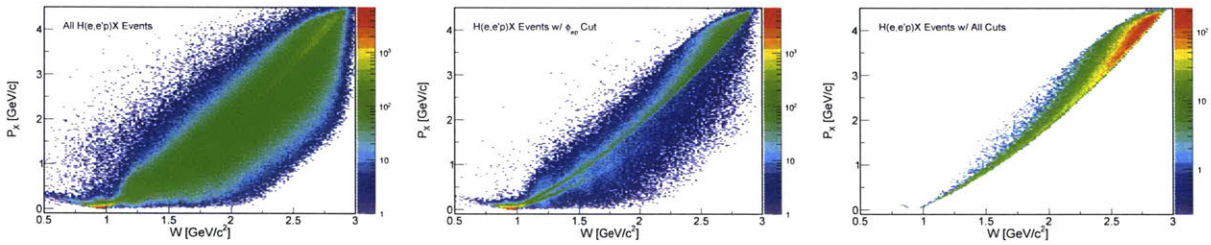

(a) (b) (c)

Figure 2-33: Missing momentum vs. invariant mass. (a) All H(e,e'p)X events. (b) Events passing the electron-proton coplanarity cut. (c) Events passing all three cuts discussed in the text. These events constitute our sample of radiative elastic events.

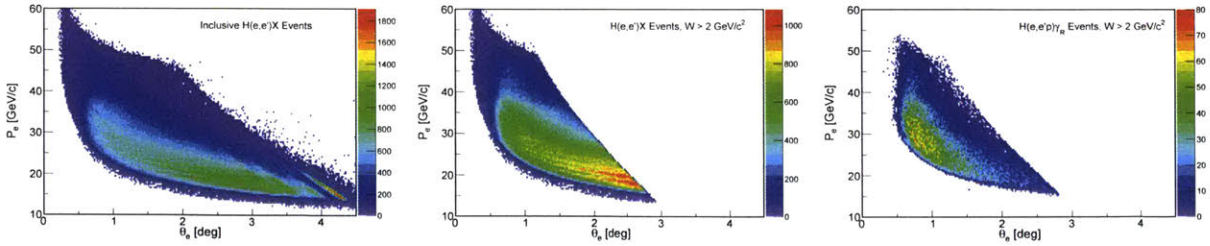

(a) (b) (c)

Figure 2-34: Scattered Electron Momentum vs. Polar angle. (a) All H(e,e')X events. (b) H(e,e')X events, with $W > 2\ GeV$. (c) Radiative elastic $H(e, e'p)\gamma_R$ events, with $W > 2\ GeV$.

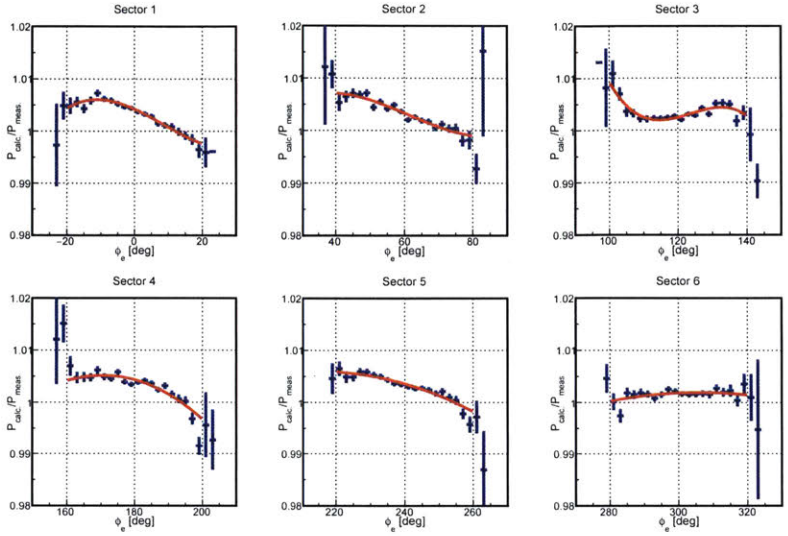

(a) Ratio of calculated to measured electron momentum vs. ϕ for radiative elastic events. The ratios are fit with a 3^{rd} degree polynomial to determine $f(\phi)$.

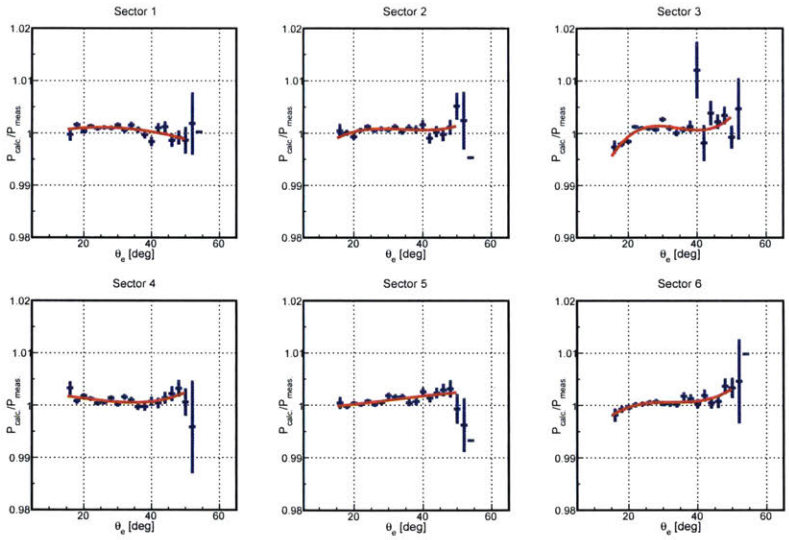

(b) Ratio of calculated to measured electron momentum divided by $f(\phi)$ vs. θ for radiative elastic events. The ratios are fit with a 3^{rd} degree polynomial to determine $g(\theta)$.

Figure 2-35: Electron momentum ratios before applying the corrections.

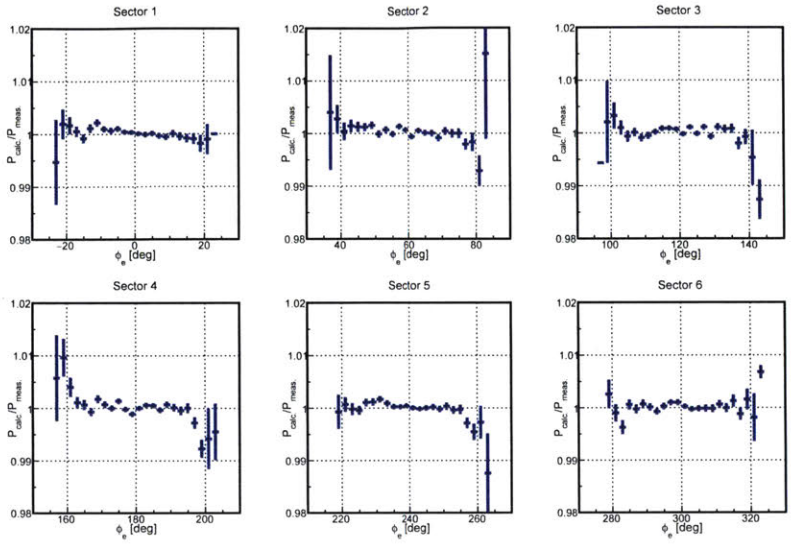

(a) Ratio of calculated to measured electron momentum vs. ϕ for radiative elastic events after applying the electron momentum corrections.

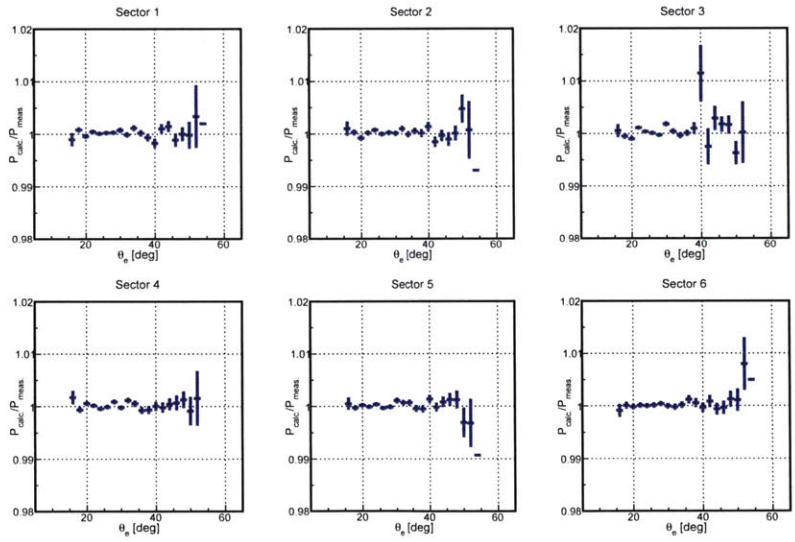

(b) Ratio of calculated to measured electron momentum vs. θ for radiative elastic events after applying the electron momentum corrections.

Figure 2-36: Electron momentum ratios after applying the corrections.

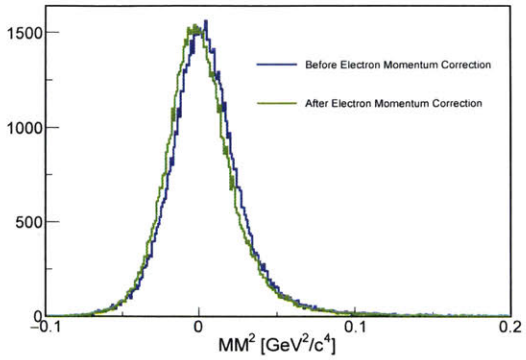

Figure 2-37: Comparison of the square of the missing mass for radiative elastic events before and after applying the electron momentum corrections.

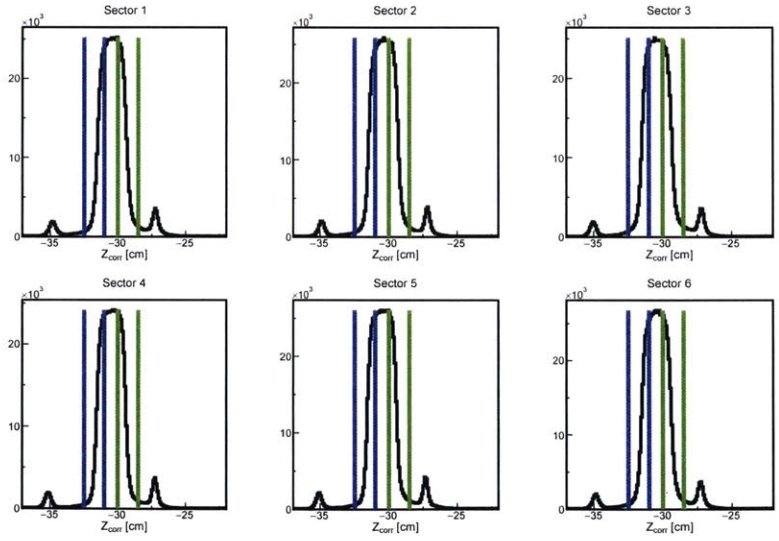

Figure 2-38: Corrected electron hydrogen target vertex for the six sectors. We study the momentum corrections for the two different regions of the target shown by the sets of vertical lines.

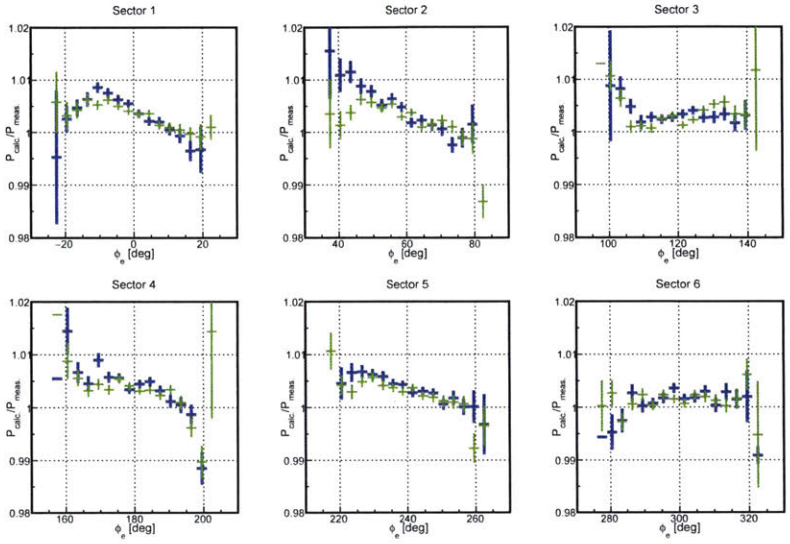

(a) Ratio of calculated to measured electron momentum vs. ϕ for radiative elastic events with large invariant mass. The data is shown for the two regions of the hydrogen target selected in figure 2-38.

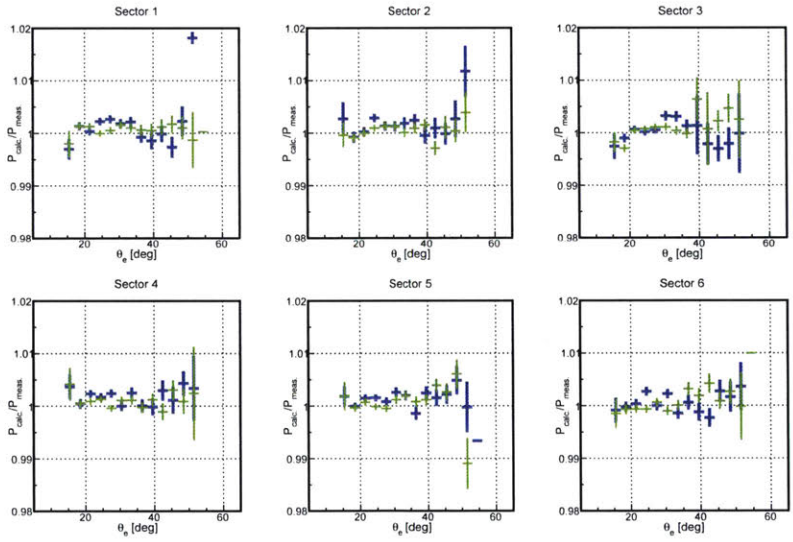

(b) Ratio of calculated to measured electron momentum vs. θ for radiative elastic events with large invariant mass. The data is shown for the two regions of the hydrogen target selected in figure 2-38.

Figure 2-39: Electron momentum ratios for different hydrogen target regions.

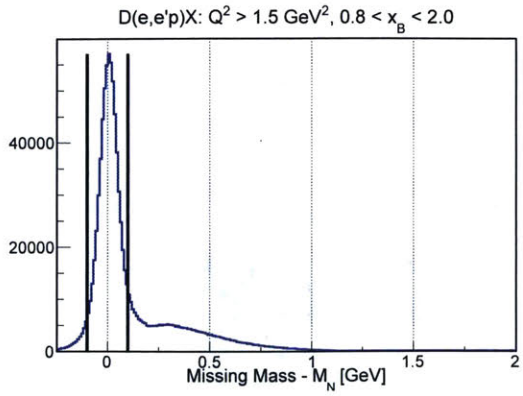

Figure 2-40: Reconstructed missing mass minus the nucleon mass for D(e,e'p)X large Q^2 and large x_B events. The applied Q^2 and x_B cuts are stated on the plot. We select QE events using the cut shown in the plot (i.e. the events between the vertical lines).

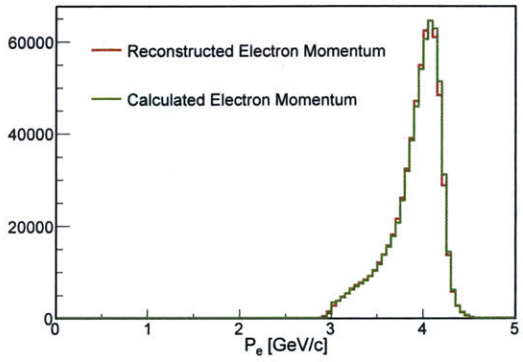

Figure 2-41: Reconstructed (red curve) and calculated (green curve) electron momentum for the D(e,e'p)n events in figure 2-40. The electron momentum is calculated assuming the scattered electron angles, the final proton angles, and the final proton momentum are correctly reconstructed.

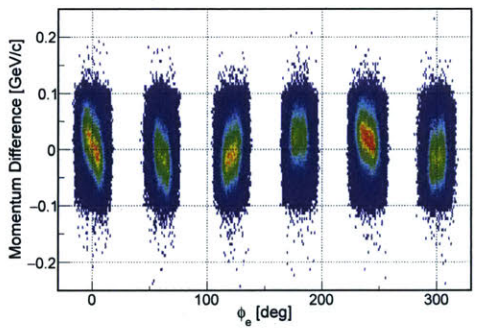

(a) Difference between the calculated and reconstructed electron momentum for D(e,e'p)n events vs. the electron azimuthal angle.

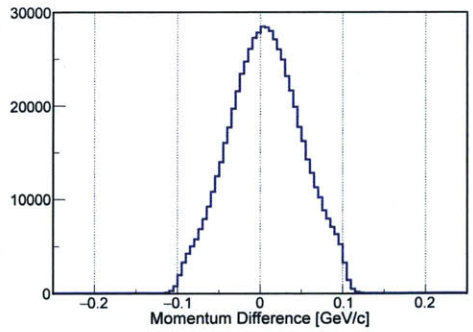

(b) Difference between the calculated and reconstructed electron momentum for D(e,e'p)n events.

Figure 2-42: QE Electron momentum correction estimation.

2.4 Data Quality and Background Removal

2.4.1 Data Quality

In order to select the set of good runs for the final analysis, we follow the procedure of the first EG2 analysis [39] and calculate the yield for every run corrected for the beam charge and live-time. In figure 2-43, we show the normalized inclusive yield for the deuterium data. We combine all the deuterium data when calculating the cross-section ratios, with runs having greater than a 4% deviation from the mean normalized yield excluded from the final analysis. In figures 2-44 and 2-45, we show the normalized inclusive yields for the solid targets. We again remove runs from the final analysis which have larger than a 4% deviation from their respective target's weighted average yield.

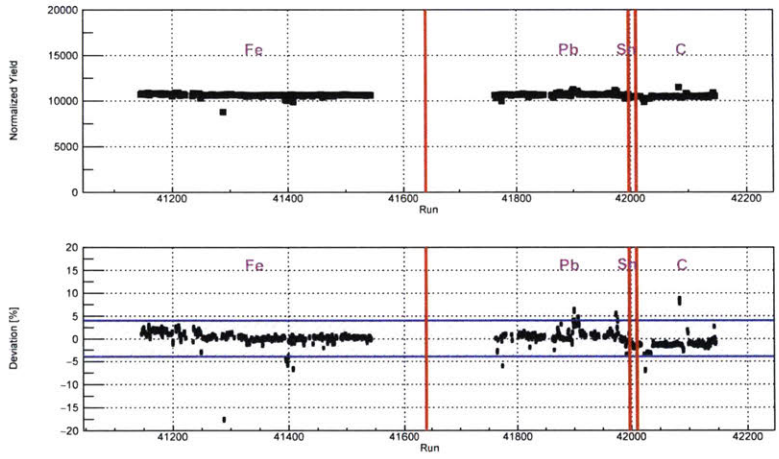

Figure 2-43: Top: Charge normalized yield from the deuterium target for (e,e') events vs. run number. Bottom: Percent deviation from the weighted average yield vs. run number. The shaded region indicates the runs used. In both plots, the vertical lines demarcate the beginning or ending or a given solid target run period.

2.4.2 Background Removal

In figure 2-46, we show the reconstructed electron vertex for the entire dataset used in this analysis. (The tin target was found to be shifted by about 1 cm from the other solid targets. It is believed that this is due to the tin target not being fully inserted

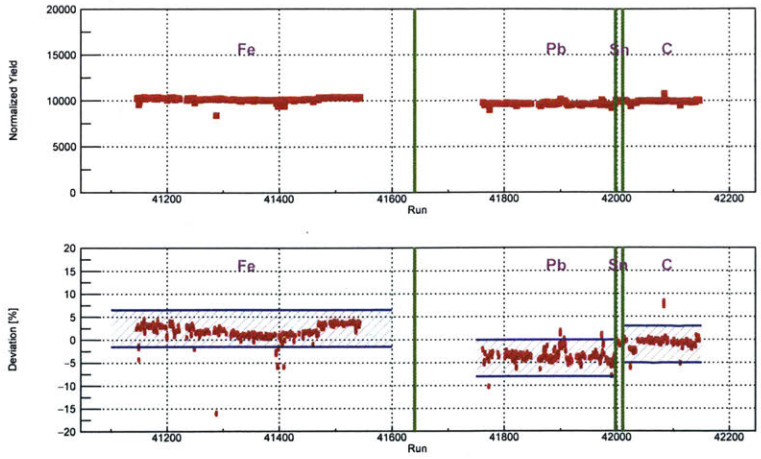

Figure 2-44: Top: Charge and target thickness normalized yield for the four solid targets run concurrently with deuterium for (e,e') events vs. run number. Bottom: Percent deviation from the weighted average yield vs. run number. The shaded region indicates the runs used. In both plots, the vertical lines demarcate the beginning or ending or a given solid target run period.

into the beamline. For this reason, we do not analyse the tin data in this work.) In figure 2-47, we show the reconstructed electron vertex in the DIS region and the large x_B QE region. The kinematic cuts used to select the DIS and QE regions are discussed in section 2.5.1.

Background to the CryoTarget

The 2 cm long cryotarget cell consists of aluminum entrance and exit windows which together are equivalent to 2.5% of the luminosity of the deuterium target [35]. Two approaches can be used to remove the background events when calculating the cryotarget yield: a vertex cut can be applied outside the target cell and then the background subtracted using the empty target runs bin-by-bin in x_B; or the walls can be removed by a vertex cut in the center of the liquid target.

For the QE events, there are not enough statistics for a good background subtraction. So, a 1 cm long cut (i.e. $\pm 0.5\,cm$) is applied in the middle of the liquid target. This cut is justified by figure 2-48b. In this figure, the blue points show the yield when cutting outside the target and subtracting the empty target. Even after subtraction, the normalized yield is not stable outside the target. The red points show the yield

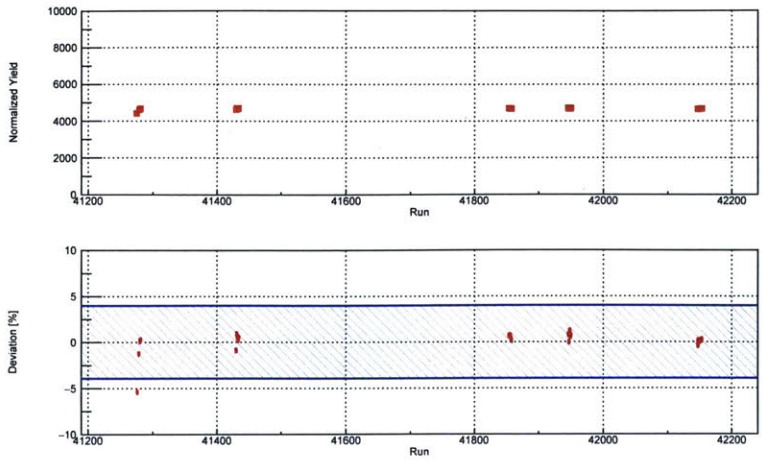

Figure 2-45: Top: Charge normalized yield for the thick aluminum target vs. run number. Bottom: Percent deviation from the weighted average yield vs. run number. The shaded region indicates the runs used.

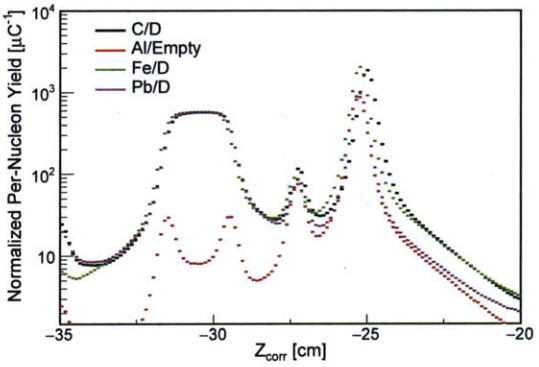

Figure 2-46: Reconstructed corrected electron vertex for all targets. Note that the thick aluminum target was run with the cryotarget cell empty. The data in the figure are normalized by the total beam charge collected for a given target combination.

scaled up to the full cryotarget length (i.e. 2 cm) for different cut widths inside the target. This normalized yield is seen to be stable for all cuts with full width less than 1 cm. However, there is still some background within the 1 cm cut that must be taken into account. This background is very small for low x_B values (i.e. $x_B < 1$), but can become significant at larger values (i.e. $x_B > 1.5$). The green points in figure 2-48b show the result when the background under the specified cut is subtracted using the empty target runs. For the high x_B range shown, the background represents about 7.5% of the events for all cuts with full width less than 1 cm.

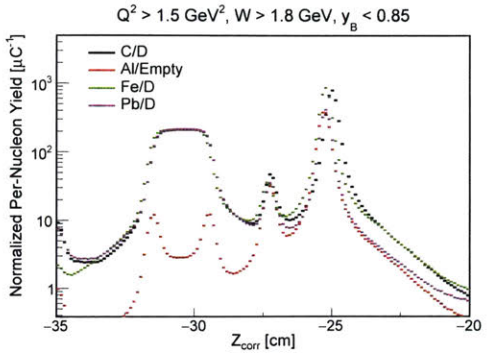

(a) DIS Events.

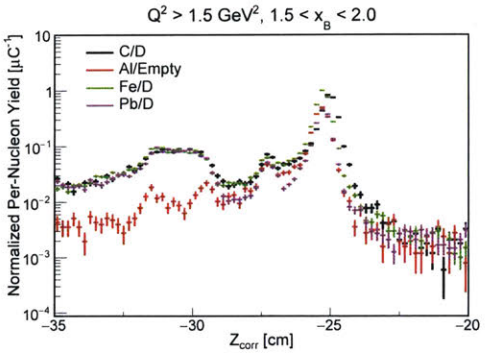

(b) QE Events with large x_B.

Figure 2-47: Reconstructed corrected electron vertex for all targets for different kinematic regions. The normalization is the same as in figure 2-46.

For the DIS events, we have sufficient statistics to perform a background subtraction. In this case, we apply a vertex cut with a full width of 3 cm and subtract the empty target contribution bin-by-bin in x_B. As can be seen in figure 2-48a, the normalized yield after the background subtraction is more stable than in the QE case. We compare the final results to those obtained if we cut inside the target when placing final uncertainties on the data.

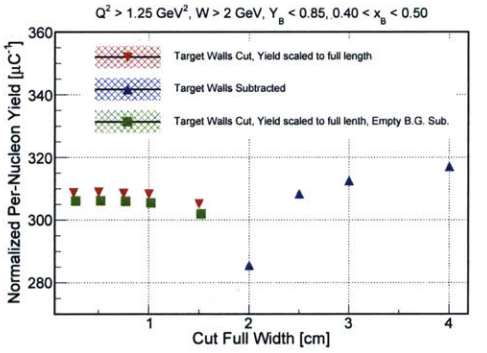

(a) Normalized electron yield from the deuterium target. We apply a cut to select the DIS region and look at a specific range in x_B. The cut stability results are similar for other x_B ranges.

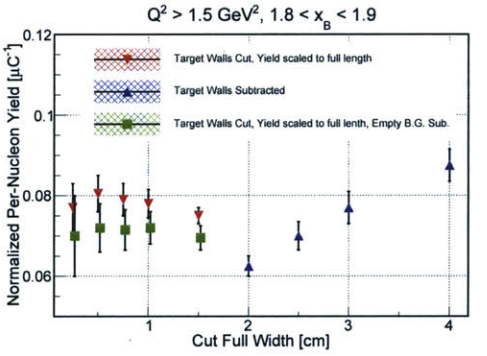

(b) Normalized electron yield from the deuterium target. We apply a cut on Q^2 here and look at a specific range in x_B that is within our QE region of interest. The cut stability results are similar for other x_B ranges.

Figure 2-48: Normalized electron yield from the deuterium target

For the final binning and kinematic cuts selected in sections 2.6.1 and 2.6.2 for the DIS and QE regions, respectively, we plot the ratio of the weighted (see section 2.5) background to the signal-plus-background in figure 2-49.

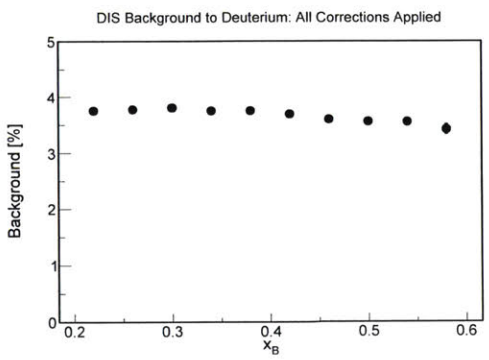

(a) Weighted background (in percent) to DIS deuterium events using a vertex cut with a 3 cm full width.

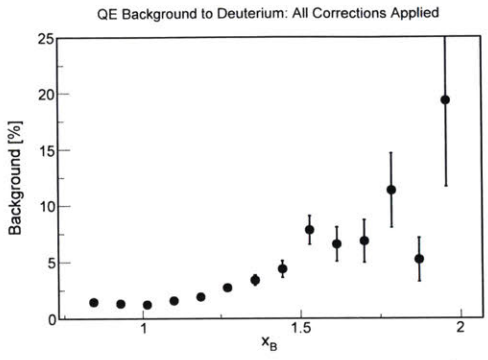

(b) Weighted background (in percent) to QE deuterium events using a vertex cut with a 1 cm full width.

Figure 2-49: Background to the deuterium cryotarget in the two kinematic regions under study.

Background to the Solid Targets

We determined the background to the solid targets by looking at runs where only the deuterium cryotarget was present. In figure 2-50a, we show the reconstructed electron vertex using a DIS cut. The vertex cut used to select the solid target is shown by the red lines. As can be seen there is some background present where the solid target would be located. By normalizing on beam charge and live-time, we determined this background to account for 0.4-0.8% of the yield from the various solid targets run concurrently with deuterium. (For the thick aluminum target run with the empty cryotarget cell, the background was about 0.1%).

We performed a similar analysis for the QE events (figure 2-50b). Here we do not see any background under the solid target, and therefore do not perform any subtraction.

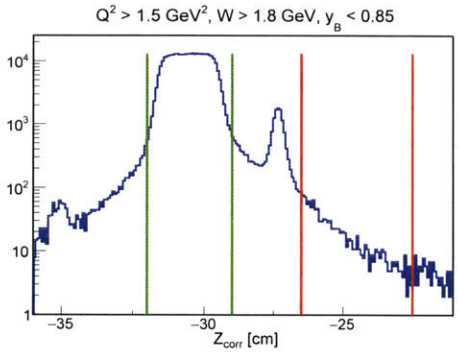

(a) Reconstructed DIS electron vertex when only the deuterium cryotarget is located in the beamline. (See section 2.5.1 for details on the kinematic cut selection.) During the main cross-section ration analysis, we select events originating from the solid target using the vertex cut shown by the red lines; the vertical green lines are used to select events from the deuterium target for the DIS measurement.

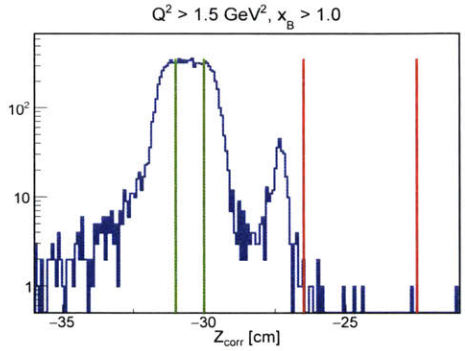

(b) Reconstructed QE electron vertex when only the deuterium cryotarget is located in the beamline. (See section 2.5.1 for details on the kinematic cut selection.) During the main cross-section ration analysis, we select events originating from the solid target using the vertex cut shown by the red lines; the vertical green lines are used to select events from the deuterium target for the QE measurement.

Figure 2-50: Reconstructed electron vertex with no solid target.

2.5 Cross-Section Ratio Extraction

Unlike in a small-acceptance spectrometer which measures a cross-section at nearly a fixed angle and with a small momentum bite, the *CLAS* detector has a large acceptance. We wish to calculate cross-section ratios at fixed x_B values. The cross-section is differential with respect to two independent variables (e.g. $\frac{d^2\sigma}{d\Omega dE}$ or $\frac{d^2\sigma}{dxdQ^2}$). When we calculate the cross-section ratios at a given x_B, we are integrating over whatever range in Q^2 is kinematically allowed by the beam energy, detector acceptance, and our cuts. This integration over Q^2 is not a problem because the EMC ratios and a_2 values are known to be Q^2 independent above a certain threshold [2, 14, 16]. In addition, we study the effects of changing the kinematic cuts in section 2.6.

The procedure to extract the cross-section ratios is then as follows. The data are first binned in x_B, and every event in a given x_B bin is given the following weight:

$$Weight = \frac{1}{NORM} \times \frac{RC \times CC \times ISO}{ACC} \times BC\,, \tag{2.12}$$

where

$$ACC = \frac{N_{Accepted}(x_{event}, Q^2_{event})}{N_{Generated}(x_{event}, Q^2_{event})}\,,$$

$$RC = \frac{\sigma_{Born}(x_{event}, Q^2_{event})}{\sigma_{Rad}(x_{event}, Q^2_{event})}\,,$$

$$CC = \frac{\sigma_{Born}(E, E', \theta)}{\sigma_{Born}(E + \Delta E, E' + \Delta E, \theta)} \times \left(\frac{E}{E + \Delta E}\right)^2 @\,(E', \theta) = (x_{event}, Q^2_{event})\,,$$

$$ISO = \frac{\frac{A}{2} \cdot \left(1 + \frac{\sigma_n}{\sigma_p}\right)}{Z + N \cdot \frac{\sigma_n}{\sigma_p}} @\, x_{event}\,,$$

$$BC = \frac{\sigma_{Born}(x_{center}, Q^2_{event})}{\sigma_{Born}(x_{event}, Q^2_{event})}\,.$$

In equation 2.12, *NORM* is the standard luminosity factor, which is equal to the total number of initial electrons times the target thickness in nucleons per square centimeters times the system live-time. *ACC* is the acceptance correction factor, which will be discussed in section 2.5.3. The term *RC* is the radiative correction factor; the radiative corrections are discussed in section 2.5.4. The term *CC* is the coulomb correction factor; the coulomb corrections are discussed in section 2.5.5. The term *ISO* refers to the isoscalar corrections, which can be applied to the DIS cross-section ratios; the isoscalar corrections are discussed in section 2.5.6. *BC* is the bin-centering correction, and is applied after all other corrections to re-weight the events with their equivalent value at the center of the bin. We note that the bin-centering correction is applied using the Born model cross-section as it applied after the radiative corrections. The effects of the bin-centering correction are discussed in section 2.5.7.

The integrated cross-section at a specific x_B value is equal to the sum of the weights in a given bin. When calculating the cross-section for deuterium, the empty target contribution is weighted event-by-event in the exact same manner and then subtracted. So, the per nucleon cross-section ratio for a nucleus A to deuterium is calculated as follows:

$$\left(\frac{\sigma(A)/A}{\sigma(D)/2}\right) = \frac{Y_A^{Weighted}}{Y_D^{Weighted} - Y_{Empty}^{Weighted}}, \tag{2.13}$$

where $Y_A^{Weighted}$, $Y_D^{Weighted}$, and $Y_{Empty}^{Weighted}$ are the weighted yields of the nuclear target, the deuterium target, and the empty cryotarget, respectively. (When calculating the *NORM* term for the empty runs, the thickness of the deuterium target is used, which is equivalent to subtracting the contribution from the empty target prior to normalizing the deuterium yield by its thickness.)

In order to calculate the statistical uncertainty in equation 2.13, the statistical uncertainties of each of the three yields is correctly propagated. The full uncertainty is the combination in quadrature of the statistical uncertainty and the point-to-point and normalization systematic uncertainties.

2.5.1 Kinematic Selection Cuts

To calculate the inclusive cross-section ratios, we have to select a set of cuts on the standard kinematic variables (figure 2-51). To do this, we make use of the *CLAS* simulation. We uniformly generate electrons in energy and solid angle from the corresponding target location. Then, for every generated event, we apply a weight using our model cross-section described in section 2.5.2 [52]. We generate a grid of our model cross-section at fixed values of Q^2 and x_B. We then radiate the model cross-section [49] to get a radiated cross-section at each grid point. For every generated event, we perform a two-dimensional linear interpolation to calculate the radiated cross-section at the specific Q^2 and x_B value.

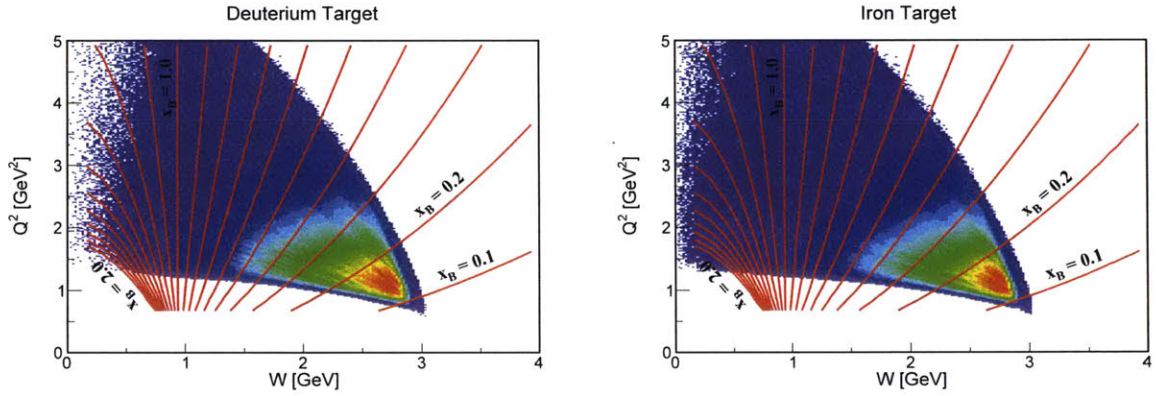

(a) (b)

Figure 2-51: Reconstructed Q^2 vs. W with x_B contours for (e,e') events. (a) Deuterium target. (b) Iron target.

In figure 2-52a, we show four kinematic variables (Q^2, W, x_B, and $y_B = \frac{\nu}{E_{Beam}}$) for the deuterium data compared to the weighted deuterium DIS simulation. We begin by applying a cut above the resonance region at $W > 1.8\ GeV$. Using the resultant distributions (figure 2-52b), we then select a cut on Q^2 based on where the data and reconstructed simulation begin to match well. We apply a cut of $Q^2 > 1.50\ GeV^2$ (figure 2-52c). The last kinematic cut we apply is $y_B < 0.85$, which is equivalent to requiring the scattered electron to have a momentum greater than about 750 MeV/c. After all these cuts are applied, the data and the reconstructed simulation match quite nicely (figure 2-53). Since the cross-section model can describe the data well,

we use it for many of the corrections required in this analysis. In section 2.6.1, we examine the effect of adjusting the kinematic cuts on the DIS cross-section ratios.

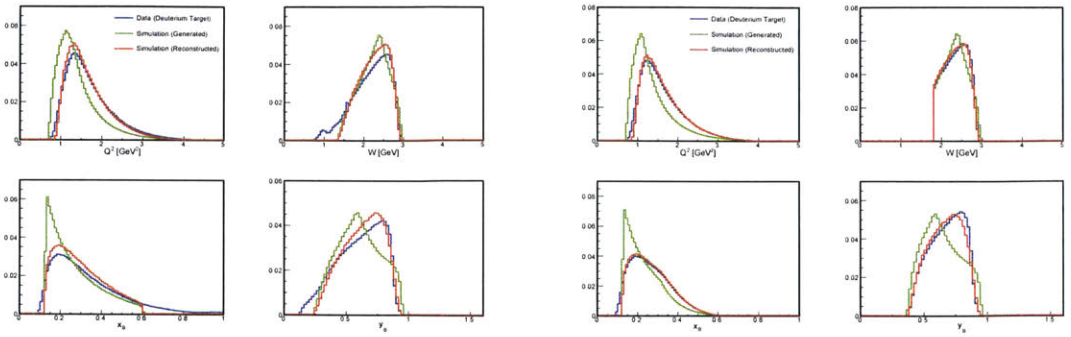

(a) No Kinematic Cuts

(b) $W > 1.8\ GeV$

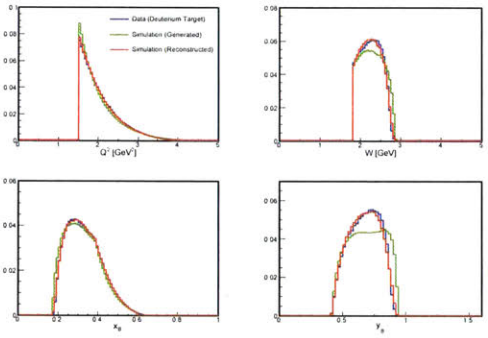

(c) $W > 1.8\ GeV$ & $Q^2 > 1.50\ GeV^2$

Figure 2-52: Comparison of data and radiated DIS model cross-section. The green curves are the generated events in the simulation; the red curves are the accepted and reconstructed events in the simulation; the blue curves are the data from the deuterium target. The yields are normalized to the same integral, so only the shape is compared. Clockwise from Top Left: Q^2, W, y_B, x_B.

For the QE case, we are interested in the range $0.8 < x_B < 2.0$ (primarily in the plateau region from $1.4 < x_B < 2.0$. As discussed in section 1.2, we need to apply a cut of $Q^2 > 1.5\ GeV^2$ in order to select nucleons with high momentum [2]. In figure 2-54, we compare the radiated QE model cross-section to the data for the carbon target.

2.5.2 Model Cross-Section

Model cross-sections for both the DIS and QE region are taken from the code *INCLUSIVE* [52]. These model cross-sections are used to determine the kinematic cuts,

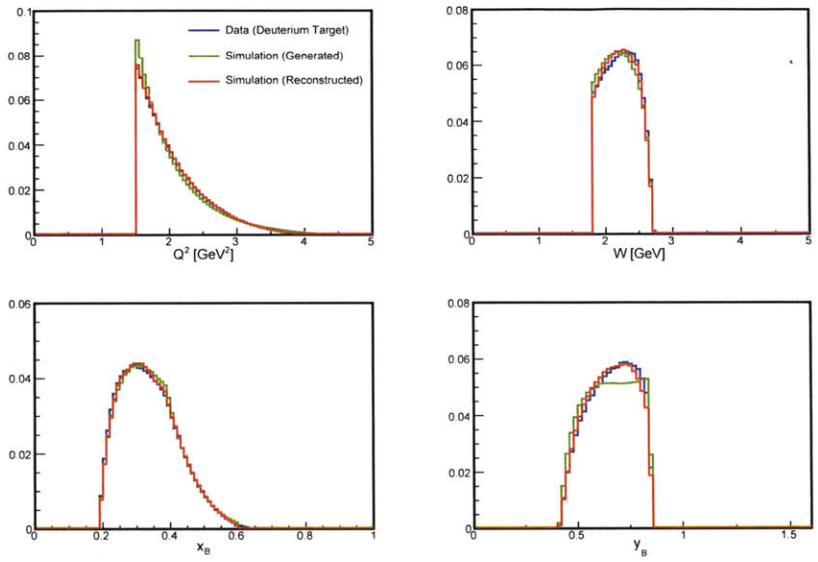

Figure 2-53: Same as figure 2-52a, except now with a cut of $W > 1.8\ GeV$, $Q^2 > 1.50\ GeV^2$ & $y_B < 0.85$ applied.

for the bin-centering corrections, for the radiative corrections, and for the coulomb corrections. The DIS (QE) model cross-sections are shown for all targets in figure 2-55 (2-56). As discussed above, the model cross-sections are generated on a two-dimensional grid, and are linearly interpolated to determine the model cross-section at any location between the grid points.

2.5.3 Acceptance Corrections

Acceptance corrections are applied using the standard *CLAS* simulation (which consists of GSIM, GPP, and RECSIS) [39], with the *EG2c* efficiency maps and calculated resolutions included. Electrons are generated uniformly in solid angle and energy from both the liquid and solid target locations. In order to correctly account for bin-migration effects, the generated events are weighted using the radiated model cross-sections. The acceptance corrections are calculated in two-dimensional bins. For the DIS region, the simulated data is binned in Q^2 and W, because we apply cuts on these kinematic variables. For the QE region, the simulated data is binned in Q^2 and x_B, since only a kinematic cut on Q^2 is applied. For every such bin, the ACC term in equation 2.12 is calculated as

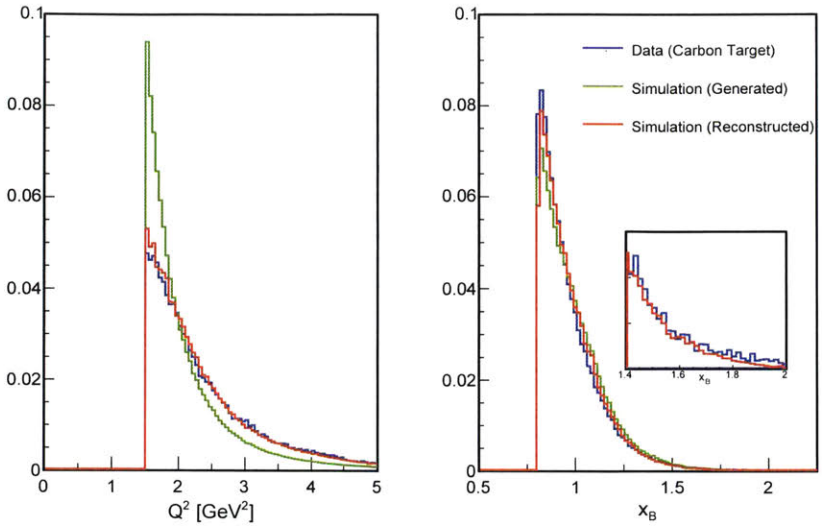

Figure 2-54: Comparison of carbon data and radiated QE model cross-section. The green curves are the generated events in the simulation; the red curves are the accepted and reconstructed events in the simulation; the blue curves are the data from the carbon target. The yields are normalized to the same area, so only the shape is compared. We apply a cut here of $Q^2 > 1.5\ GeV^2$ & $0.8 < x_B < 2.0$. Left: Q^2. Right: x_B. The inset compares the data and reconstructed simulation at high x_B.

$$ACC = \frac{N_{Reconstructed}}{N_{Generated}}, \tag{2.14}$$

where $N_{Reconstructed}$ ($N_{Generated}$) is the number of events reconstructed (generated) in that two-dimensional bin.

The binning is chosen so that the statistical uncertainty for all bins (except at the edges of the acceptance) is less than 0.75% for the DIS acceptance (3.0% for the QE acceptance). In addition, for the DIS region, we made sure that each x_B bin used in the final analysis (section 2.6.1) is covered by multiple acceptance bins in both W and Q^2. In the QE region, the number of x_B bins used for the acceptance correction is equivalent to the number used in the final analysis (section 2.6.2).

The extracted DIS acceptance maps for the deuterium and solid (carbon) targets are shown in figure 2-57; the QE acceptance maps for the deuterium and solid (carbon) targets are shown in figure 2-58. In the final analysis, we remove events which fall inside bins with less than 2% acceptance.

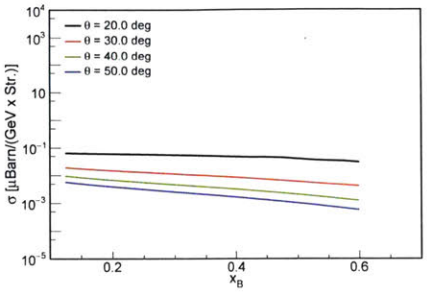

(a) Deuterium Target

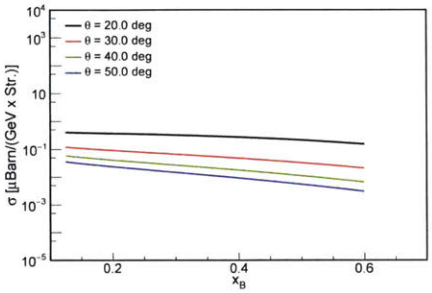

(b) Carbon Target

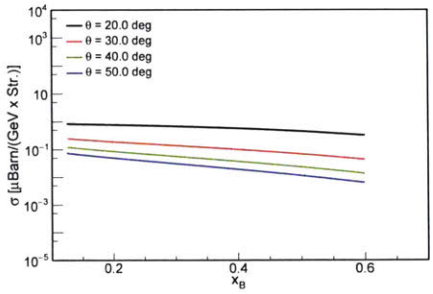

(c) Aluminum Target

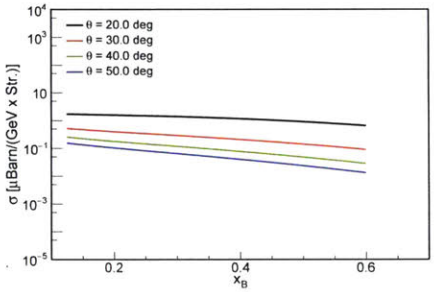

(d) Iron Target

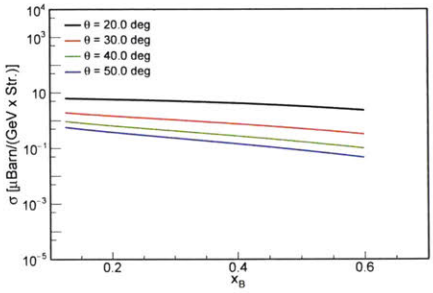

(e) Lead Target

Figure 2-55: DIS model Born cross-sections for the five targets as a function of x_B for various θ values.

In figure 2-59, we show the acceptance correction factors for the QE region for one Q^2 bin.

To estimate the overall effect of the acceptance corrections on the cross-section for each target for the final event selection/binning (sections 2.6.1 and 2.6.2), we calculate the following quantity: for each bin we take the ratio of the cross-section with all corrections applied (equation 2.12) to the cross-section with the acceptance correction weight not applied. These 'effective' acceptance correction factors are shown in figure 2-60.

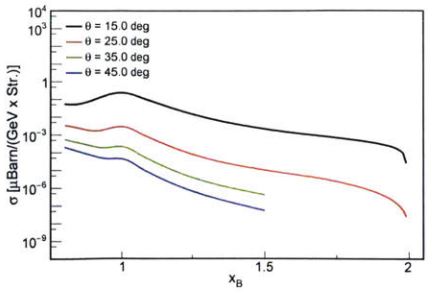

(a) Deuterium Target

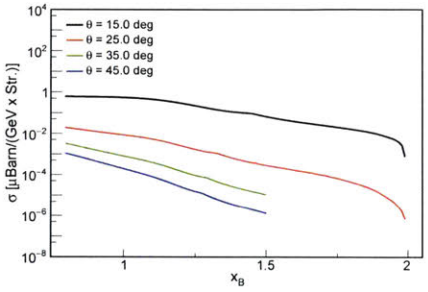

(b) Carbon Target

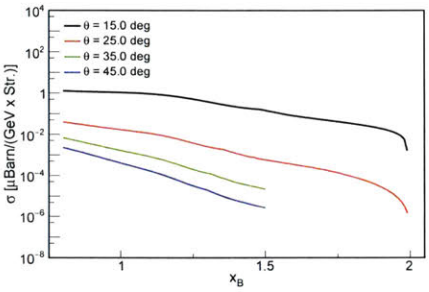

(c) Aluminum Target

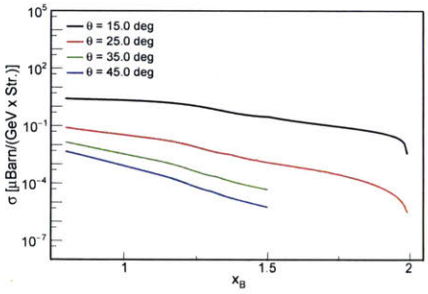

(d) Iron Target

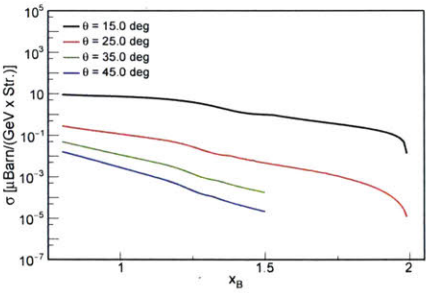

(e) Lead Target

Figure 2-56: QE model Born cross-sections for the five targets as a function of x_B for various θ values.

2.5.4 Radiative Corrections

Radiative corrections must be applied to obtain the underlying Born cross-sections from the measured cross-sections. As described in Ref. [49], an unfolding procedure can be used to extract the Born cross-section from the measured radiated cross-section. In our case, this is obviously not practical, and a different procedure has to be used. Within the code *INCLUSIVE* [52], the model cross-sections are internally and externally radiated according the prescription given in Ref. [49]. A correction factor can then be calculated for any electron scattering angle and energy (or x_B and

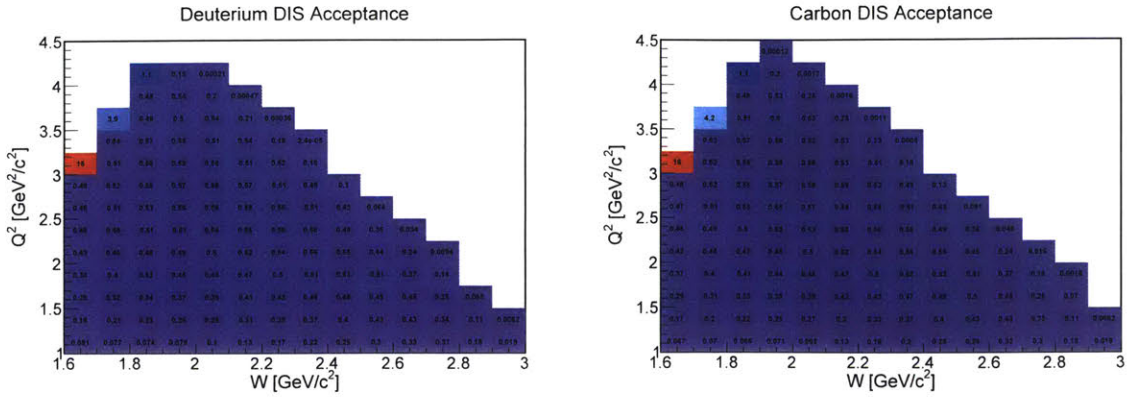

(a) Deuterium Target (b) Solid (carbon) Target

Figure 2-57: Acceptance correction factors in the DIS region.

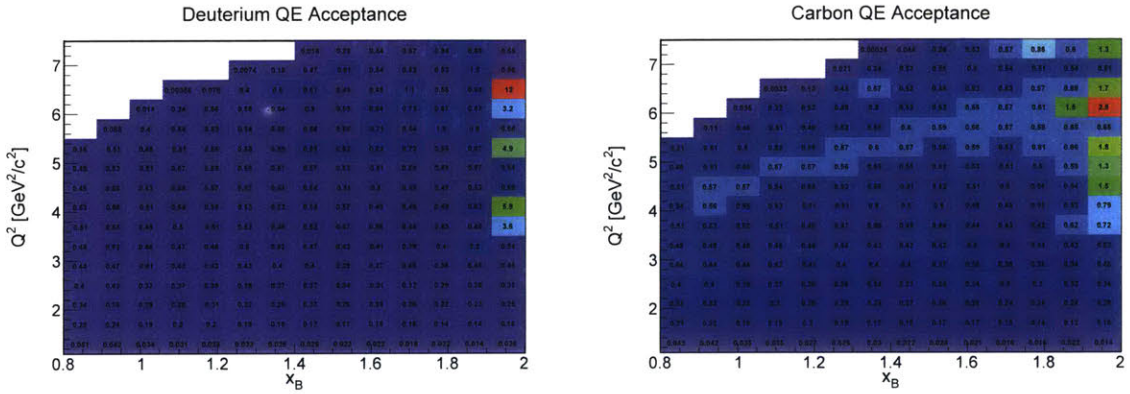

(a) Deuterium Target (b) Solid (carbon) Target

Figure 2-58: Acceptance correction factors in the QE region.

Q^2). The radiative correction factor is defined as the ratio of the model Born to the radiated cross-section:

$$RC = \frac{\sigma_{Born}}{\sigma_{Rad}}. \tag{2.15}$$

In equation 2.12, the Born and radiated cross-sections are evaluated at the measured x_B and Q^2 values. In figure 2-61 (2-62), we show the radiative correction factors as a function of x_B in the DIS (QE) region.

To estimate the overall effect of the radiative corrections on the cross-section for each target for the final event selection/binning (sections 2.6.1 and 2.6.2), we calculate the following quantity: for each bin we take the ratio of the cross-section with all

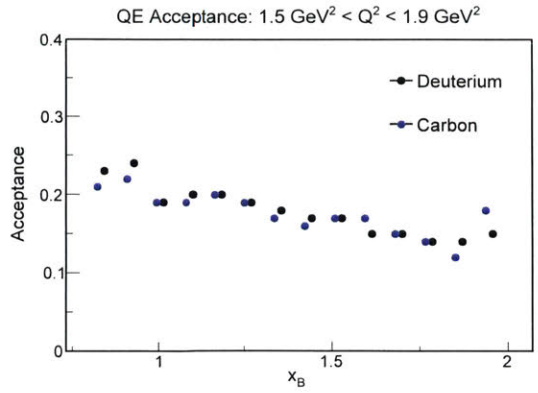

Figure 2-59: QE Acceptance correction factors for one Q^2 bin.

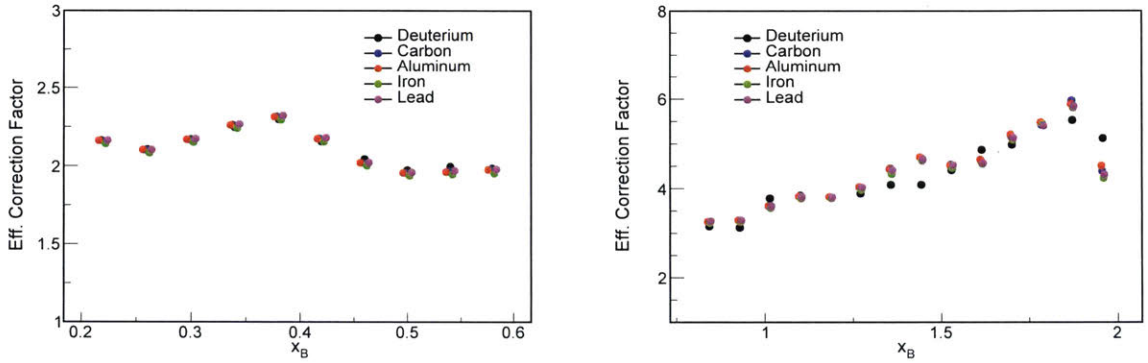

(a) DIS Events.

(b) QE Events.

Figure 2-60: 'Effective' acceptance correction factors.

corrections applied (equation 2.12) to the cross-section with the radiative correction weight not applied. These ratios are shown in figure 2-63, and they qualitatively agree with the curves shown in figures 2-61 and 2-62. We place uncertainties on the applied radiative corrections in section 2.6.3.

2.5.5 Coulomb Corrections

The initial (scattered) electron is accelerated (decelerated) by the coulomb field of the nucleus. This means that the measured beam energy and scattered momentum are not equivalent to the values at the reaction vertex. In the Effective Momentum Approximation (EMA) [53] approach, both the initial and final electron's energies at the reaction vertex are higher by an amount ΔE than the measured values. The

EMA approach has been well validated in the QE region; for the DIS region, recent work [54] suggests that the EMA approach is also reasonable.

The calculation of ΔE was don by a previous *EG2c* analysis [40], and we take the ΔE values from there. The calculated ΔE values are shown in table 2.2.

Target	$\Delta E\,[MeV]$
^{2}D	0
^{12}C	2.9
^{27}Al	5.6
^{56}Fe	9.4
^{208}Pb	20.3

Table 2.2: Coulomb correction ΔE values calculated using the Effective Momentum Approximation (EMA).

Once ΔE is known, we can calculate the coulomb correction factor in equation 2.12 as the ratio of the model cross-section at the unshifted and shifted kinematics times the focusing factor [53]. That is,

$$CC = \frac{\sigma_{Born}(E, E', \theta)}{\sigma_{Born}(E + \Delta E, E' + \Delta E, \theta)} \times \left(\frac{E}{E + \Delta E}\right)^2. \tag{2.16}$$

In equation 2.16, E, E' and θ are taken for the measured event. The ratio of the model cross-section in the equation is used to account for the fact that that we do not modify the initial and scattered electron energies from their nominal or reconstructed values. This coulomb correction factor for all targets in the DIS (QE) region is shown in figure 2-64 (2-65).

To estimate the overall effect of the coulomb corrections on the cross-section for each target for the final event selection/binning (sections 2.6.1 and 2.6.2), we calculate the following quantity: for each bin we take the ratio of the cross-section with all corrections applied (equation 2.12) to the cross-section with the coulomb correction weight not applied. These ratios are shown in figure 2-66, and they qualitatively agree with the curves shown in figures 2-64 and 2-65. We place uncertainties on the applied coulomb corrections in section 2.6.3.

2.5.6 Isoscalar Corrections for DIS Events

Previous studies of the EMC effect [18, 19] have included an isoscalar correction factor to account for the unequal number of protons and neutrons in many nuclei. In this analysis, we present results in section 2.6.1 both with and without this correction applied.

The isoscalar correction will adjust the measured cross-section per nucleon for an asymmetric nucleus A to a new value which represents the cross-section per nucleon for a nucleus A with an equal number of neutrons and protons. This correction factor is given by

$$ISO = \frac{\frac{A}{2} \cdot \left(1 + \frac{\sigma_n}{\sigma_p}\right)}{Z + N \cdot \frac{\sigma_n}{\sigma_p}} \tag{2.17}$$

In Ref. [19], the free neutron to proton cross-section ratio as a function of x_B was simply parametrized as $\frac{\sigma_n}{\sigma_p} = 1 - 0.8 \cdot x_B$. When applying isoscalar corrections in section 2.6.1, we use the updated parametrization from Refs. [11, 18]. (We also develop independent corrections using our data-based phenomenological *EMC* effect model in section 2.6.4.) Both the *JLab Hall C* and *SLAC* parametrizations are shown in figure 2-67a. In figure 2-67b we show the applied isoscalar correction factors for the various nuclei in this experiment using the *JLab Hall C* parametrization.

2.5.7 Bin-Centering Corrections

As stated above, we apply bin-centering corrections using the model Born cross-sections after all other corrections are applied. In order to estimate the overall effect of the bin-centering corrections on the cross-section for each target for the final event selection/binning (sections 2.6.1 and 2.6.2), we calculate the following quantity: for each bin we take the ratio of the cross-section with all corrections applied (equation 2.12) to the cross-section with the bin-centering correction weight not applied. These ratios are shown in figure 2-68. In the DIS region, the bin-centering correction drops for the last bin; this is because the applied kinematic cuts remove events at the

higher side of the bin. In the QE region, the correction is very different for deuterium compared to the other targets for $x_B < 1.4$. This is most likely due to the relative enhancement of the deuterium cross-section at $x_B = 1$.

It is also possible to perform the bin-centering correction using the radiated cross-sections prior to applying the other corrections (except the acceptance correction, which is always applied first). In this case, the radiative, coulomb, and isoscalar corrections are applied at the bin center. We study the effect of changing the order of the corrections on the final cross-section ratios. We then apply a systematic uncertainty on the final EMC slopes and a_2 values to account for the difference. We discuss the uncertainties related to the bin-centering corrections in section 2.6.3.

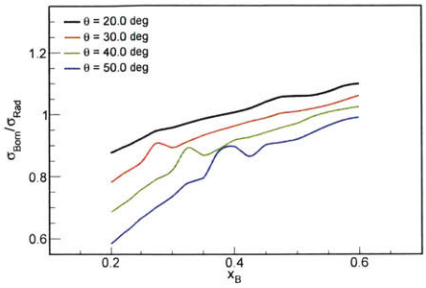

(a) Deuterium Target

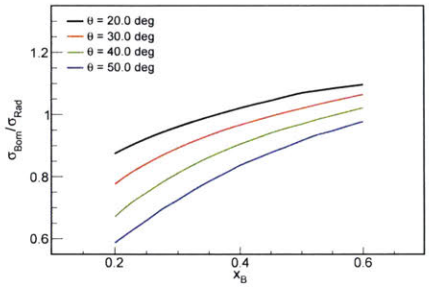

(b) Carbon Target

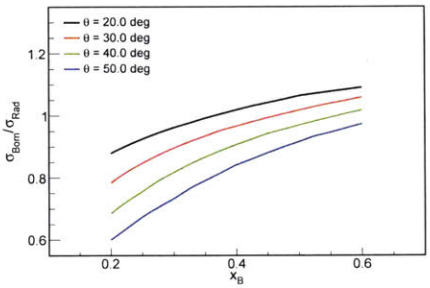

(c) Aluminum Target

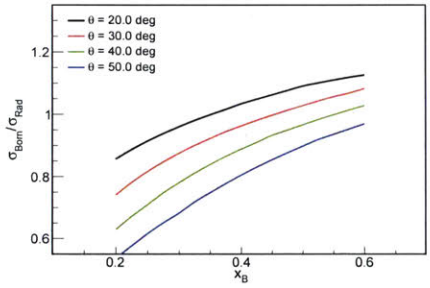

(d) Iron Target

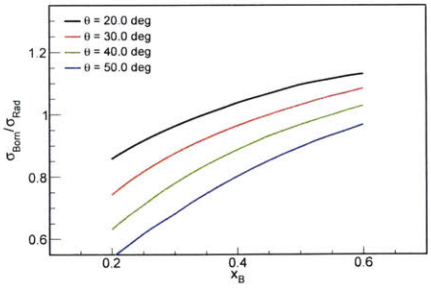

(e) Lead Target

Figure 2-61: DIS Radiative correction factors for the five targets as a function of x_B for various θ values. The correction factors are shown in the range used for the final analysis, $0.2 < x_B < 0.6$.

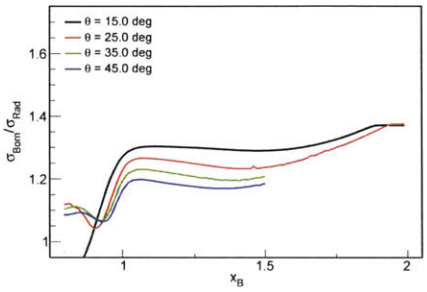

(a) Deuterium Target

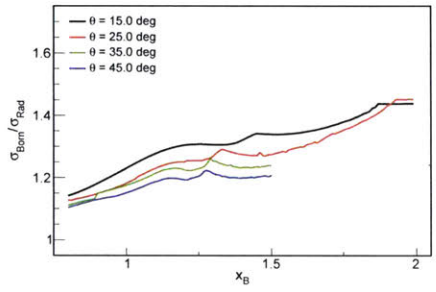

(b) Carbon Target

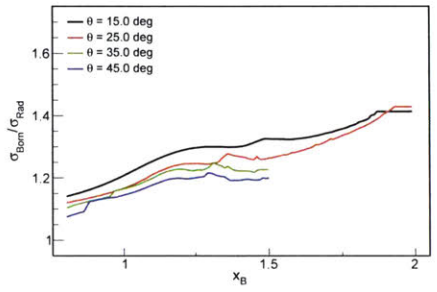

(c) Aluminum Target

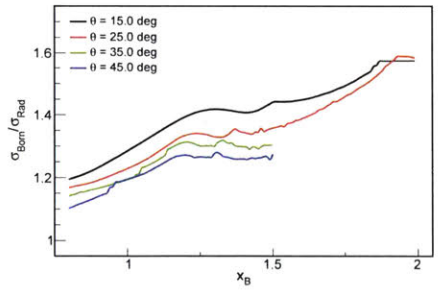

(d) Iron Target

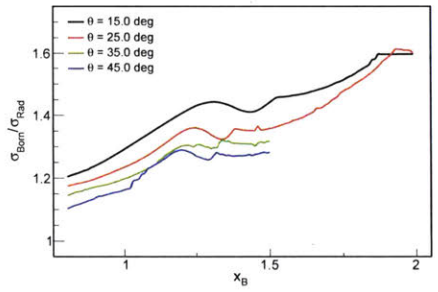

(e) Lead Target

Figure 2-62: QE Radiative correction factors for the five targets as a function of x_B for various θ values.

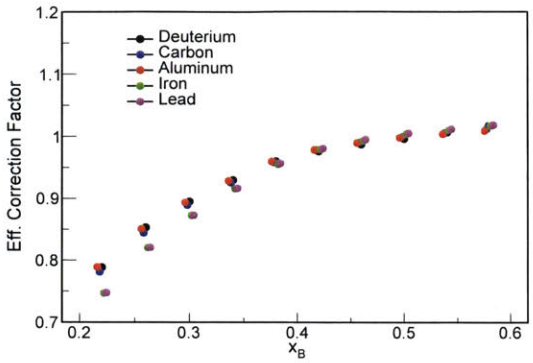

(a) DIS Events.

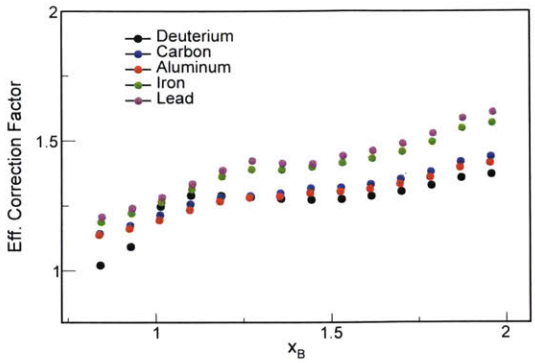

(b) QE Events.

Figure 2-63: 'Effective' radiative correction factors.

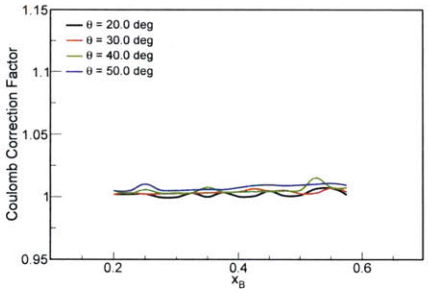

(a) Carbon Target

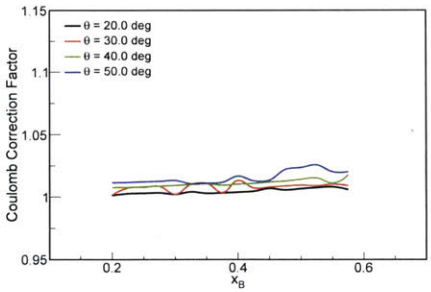

(b) Aluminum Target

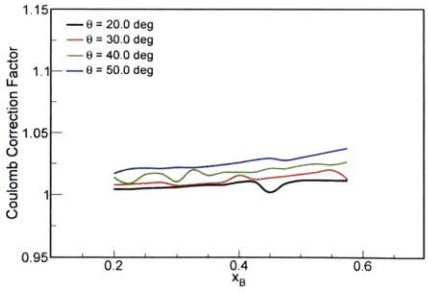

(c) Iron Target

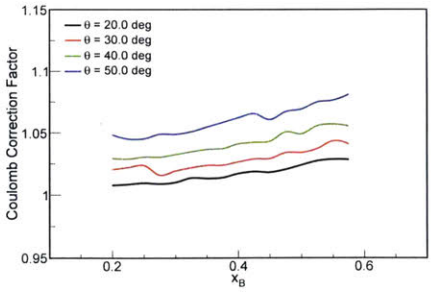

(d) Lead Target

Figure 2-64: DIS Coulomb correction factors for the five targets as a function of x_B for various θ values. The correction factors are shown in the range used for the final analysis, $0.2 < x_B < 0.6$.

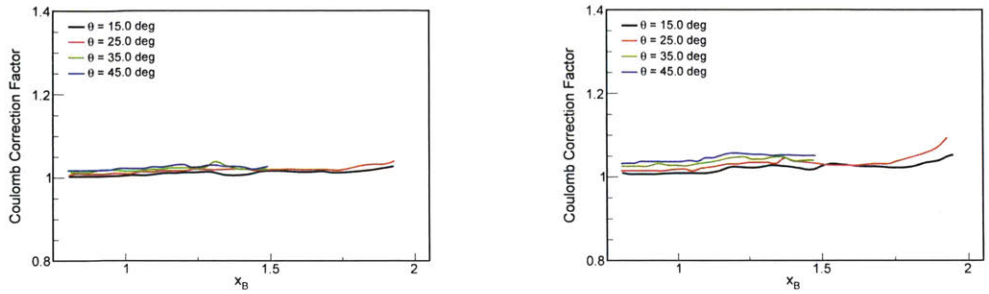

(a) Carbon Target

(b) Aluminum Target

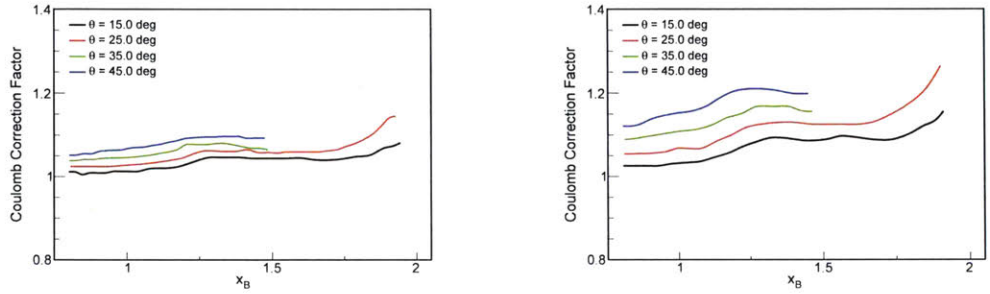

(c) Iron Target

(d) Lead Target

Figure 2-65: QE Coulomb correction factors for the five targets as a function of x_B for various θ values.

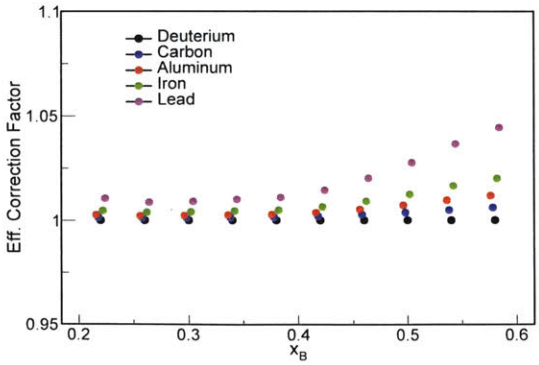

(a) DIS Events.

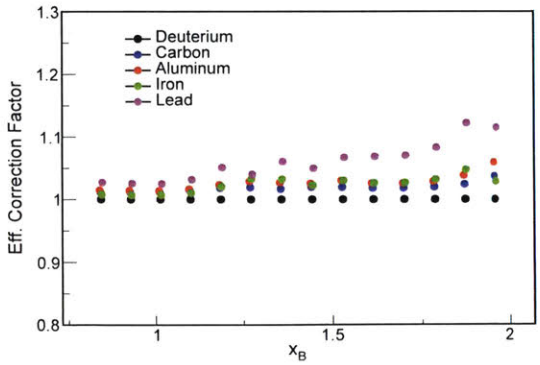

(b) QE Events.

Figure 2-66: 'Effective' coulomb correction factors.

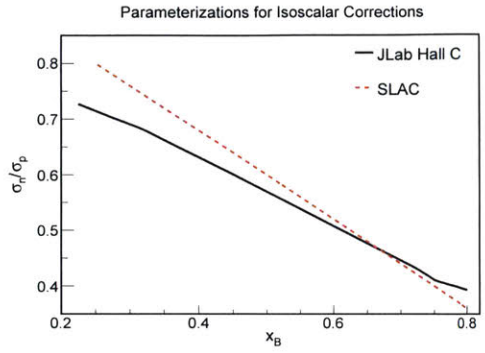

(a) Neutron to proton cross-section ratio as a function of x_B taken from *SLAC* [19] and *JLab Hall C* [18]. When applying the isoscalar corrections in section 2.6.1 for this analysis, we use the parametrization from Ref. [18].

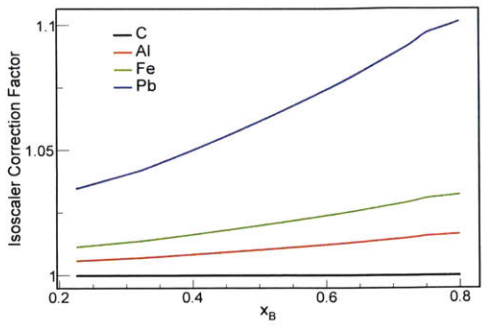

(b) Applied isoscalar correction factors for all solid targets using the *JLab Hall C* parametrization.

Figure 2-67: Isoscalar corrections.

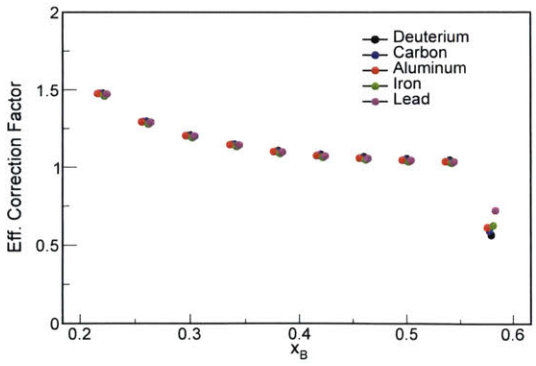

(a) DIS Events.

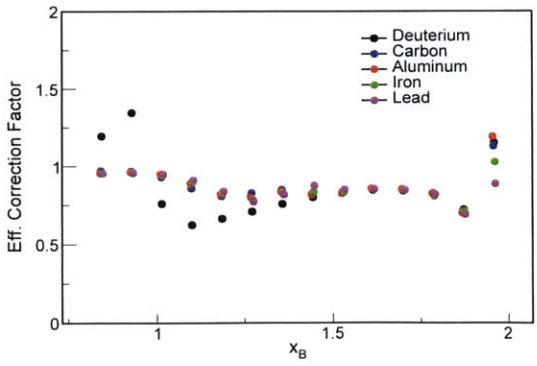

(b) QE Events.

Figure 2-68: 'Effective' bin-centering correction factors.

2.6 Final Results

We present the final cross-section ratio results in both the DIS and QE regions in this section. The DIS ratios are shown both with and without the application of isoscalar corrections. The DIS ratios are also shown with various x_B bin sizes: 0.04, 0.02, 0.0133, and 0.01. The QE ratios are shown using x_B bins of width 0.0857 and 0.0429. In section 2.6.4, we present a data-driven phenomenological model of the *EMC* effect based on nucleon SRCs. We use both our measured cross-section ratios as well as the previously published results when performing this phenomenological study.

2.6.1 DIS Cross-Section Ratios and *EMC* Slopes

The final per-nucleon cross-section ratios are shown in figure 2-69. A kinematic cut of $Q^2 > 1.5\ GeV^2$, $W > 1.8\ GeV$, and $y_B < 0.85$ is applied. The data is divided into x_B bins of width 0.04, with the data covering a range of 0.20-0.60 in x_B. The total electron yield per bin (i.e. the total number of good electrons reconstructed in each bin) for each target is shown in table 2.3 and figure 2-70. As can be seen in both the table and figure, the electron yield is very large in the bins under study, and the statistical uncertainty is negligible.

We list the measured ratios and the associated uncertainties in table 2.4. We apply a linear fit to the data from 0.26-0.54 to obtain the *EMC* slope for each nucleus in the form of

$$\left(\frac{\sigma(A)/A}{\sigma(D)/2}\right)_{ISO} = A_0 + B_0 \cdot x_B\,, \tag{2.18}$$

where A_0 and B_0 are the fit parameters. The magnitude of the slopes (B_0) are shown in table 2.5. In order to determine the stability of our slopes to the kinematic cuts, we recalculated the slopes and ratios for different cuts on Q^2 and W. The slopes for the different kinematic cuts are shown in table 2.6 and figure 2-71; the results are consistent within the uncertainties.

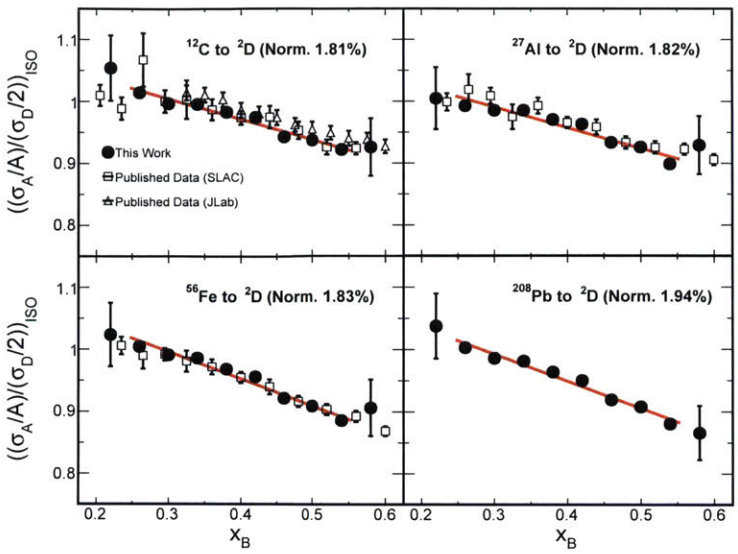

Figure 2-69: Measured DIS per-nucleon isoscalar-corrected cross-section ratios to deuterium for (clockwise from top-left) carbon, aluminum, lead and iron. The error bars on the individual points are the combined statistical and point-to-point systematic uncertainties. The shown published data comes from Refs. [18, 19] and is also isoscalar-corrected.

Results Without Isoscalar Corrections

In order to study the isospin dependence of the *EMC* effect and better understand the connection between the *EMC* effect and SRC, we also present the results without applying isoscalar corrections. This means that we do not include the *ISO* term in equation 2.12. In figure 2-72 and table 2.7, we show the DIS cross-section ratios without applying isoscalar corrections. The extracted *EMC* slopes and their accompanying uncertainties are shown in table 2.8.

Results Without Isoscalar Corrections and Finer Binning

Due to the large statistics available (table 2.3), we can divide every used bin by a factor of 2, 3, or 4 without affecting the uncertainty placed on the final ratio. This will be true as long as we divide the binning used for the acceptance correction by the same factor, and increase the total statistics used for the acceptance correction by the same factor. In figure 2-73, we show the results when we increase the points by a factor of 2, 3, or 4. As in the previous subsection, the results are shown without

x_B	^{2}D Yield	^{12}C Yield	^{27}Al Yield	^{56}Fe Yield	^{208}Pb Yield
0.22	6.2E6 (0.04)	1.3E6 (0.08)	5.1E5 (0.14)	2.7E6 (0.06)	1.0E6 (0.10)
0.26	9.2E6 (0.03)	1.9E6 (0.07)	7.4E5 (0.11)	3.8E6 (0.05)	1.5E6 (0.08)
0.30	9.7E6 (0.03)	2.0E6 (0.07)	7.7E5 (0.11)	3.9E6 (0.05)	1.5E6 (0.08)
0.34	9.2E6 (0.03)	1.9E6 (0.07)	7.3E5 (0.11)	3.6E6 (0.05)	1.3E6 (0.09)
0.38	8.1E6 (0.04)	1.6E6 (0.08)	6.3E5 (0.12)	3.1E6 (0.06)	1.2E6 (0.09)
0.42	5.8E6 (0.04)	1.1E6 (0.09)	4.5E5 (0.15)	2.2E6 (0.07)	8.1E5 (0.11)
0.46	3.6E6 (0.05)	7.2E5 (0.12)	2.8E5 (0.19)	1.4E6 (0.09)	4.9E5 (0.14)
0.50	2.1E6 (0.07)	4.1E5 (0.15)	1.6E5 (0.25)	7.6E5 (0.11)	2.8E5 (0.19)
0.54	1.1E6 (0.09)	2.2E5 (0.22)	8.3E4 (0.35)	1.8E5 (0.24)	1.4E5 (0.27)
0.58	5.0E5 (0.14)	9.7E4 (0.32)	3.8E4 (0.51)	1.8E5 (0.24)	1.4E5 (0.27)

Table 2.3: DIS yield (i.e. number of reconstructed electrons) for the various targets in each used x_B bin. The yields are shown after applying all cuts, including kinematic and vertex cuts. For a given yield, the statistical uncertainty in percent is shown in parentheses. The deuterium yield is shown with the 3 cm vertex cut, prior to any background subtraction.

applying isoscalar corrections. Tables 2.9 - 2.11 show the cross-section ratios for these bin sizes. The extracted *EMC* slopes are shown in table 2.12 and figure 2-74. The extracted slopes are consistent within uncertainties for all bin sizes.

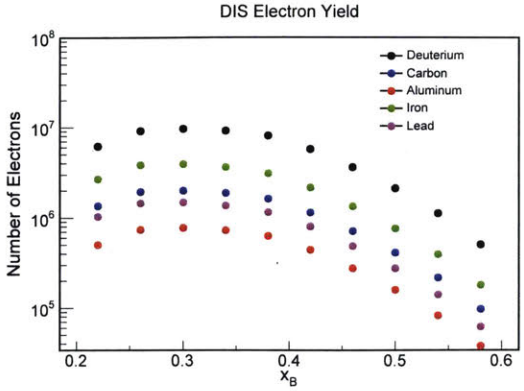

Figure 2-70: DIS yield (i.e. number of reconstructed electrons) for the various targets in each used x_B bin. The yields are shown after applying all cuts, including kinematic and vertex cuts. The deuterium yield is shown with the 3 cm vertex cut, prior to any background subtraction.

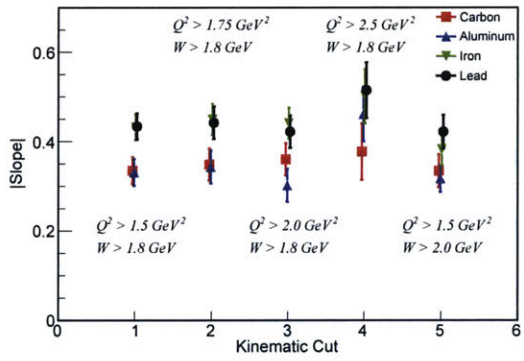

Figure 2-71: Measured *EMC* slopes for different kinematic cuts. Isoscalar corrections were applied to the ratios when extracting the slopes.

x_B	$\left(\frac{\sigma(C)/12}{\sigma(D)/2}\right)_{ISO}$ Norm. 1.81%	$\left(\frac{\sigma(Al)/27}{\sigma(D)/2}\right)_{ISO}$ Norm. 1.82%	$\left(\frac{\sigma(Fe)/56}{\sigma(D)/2}\right)_{ISO}$ Norm. 1.83%	$\left(\frac{\sigma(Pb)/208}{\sigma(D)/2}\right)_{ISO}$ Norm. 1.94%
0.22	1.054 ± 0.053	1.005 ± 0.050	1.023 ± 0.051	1.038 ± 0.052
0.26	1.015 ± 0.008	0.993 ± 0.008	1.004 ± 0.008	1.003 ± 0.008
0.30	0.997 ± 0.008	0.985 ± 0.008	0.991 ± 0.008	0.986 ± 0.008
0.34	0.996 ± 0.008	0.986 ± 0.008	0.986 ± 0.008	0.981 ± 0.008
0.38	0.983 ± 0.008	0.971 ± 0.008	0.969 ± 0.008	0.964 ± 0.008
0.42	0.974 ± 0.008	0.963 ± 0.007	0.956 ± 0.008	0.950 ± 0.008
0.46	0.943 ± 0.007	0.934 ± 0.008	0.921 ± 0.007	0.919 ± 0.007
0.50	0.937 ± 0.008	0.927 ± 0.008	0.909 ± 0.007	0.908 ± 0.007
0.54	0.922 ± 0.008	0.899 ± 0.008	0.886 ± 0.007	0.880 ± 0.007
0.58	0.926 ± 0.047	0.929 ± 0.047	0.907 ± 0.045	0.866 ± 0.044

Table 2.4: Measured DIS per-nucleon isoscalar-corrected cross-section ratios for carbon, aluminum, iron, and lead to deuterium. The error given for each point is the combined statistical and point-to-point uncertainty. The normalization uncertainty for a each ratio is stated at the top of the table.

Target	Measured $\lvert Slope\rvert$	χ^2/Ndf	Fit Err.	Norm. Err.	Z Cut Err.	Acc. Err.	Corr. Or. Err.	Published $\lvert Slope\rvert$
^{12}C	0.335 ± 0.032	4.9/6	0.030	0.006	0.004	0.0025	0.0075	0.292 ± 0.023
^{27}Al	0.330 ± 0.033	9.8/6	0.031	0.006	0.0035	0.003	0.008	-
^{56}Fe	0.435 ± 0.032	7.2/6	0.029	0.008	0.003	0.003	0.0105	0.388 ± 0.032
^{208}Pb	0.436 ± 0.031	5.8/6	0.029	0.008	0.003	0.0025	0.0035	-

Table 2.5: Measured *EMC* slopes from the fit in figure 2-69. The uncertainties shown on the extracted slopes are the combination in quadrature of the fit uncertainties, the normalization uncertainties, and half the values shown in table 2.20, table 2.21, and table 2.23. Published values are taken from Ref. [29]. All slopes come from fitting isoscalar-corrected cross-section ratios.

Applied Q^2, W Cut	Fit Range	C/D $\lvert Slope\rvert$	Al/D $\lvert Slope\rvert$	Fe/D $\lvert Slope\rvert$	Pb/D $\lvert Slope\rvert$
$Q^2 > 1.5GeV^2$ $W > 1.8GeV$	0.26-0.54	0.335 ± 0.030	0.331 ± 0.030	0.432 ± 0.029	0.434 ± 0.029
$Q^2 > 1.5GeV^2$ $W > 2.0GeV$	0.26-0.50	0.334 ± 0.037	0.317 ± 0.038	0.382 ± 0.036	0.422 ± 0.037
$Q^2 > 1.75GeV^2$ $W > 1.8GeV$	0.30-0.54	0.348 ± 0.036	0.343 ± 0.037	0.449 ± 0.035	0.442 ± 0.036
$Q^2 > 2.0GeV^2$ $W > 1.8GeV$	0.30-0.54	0.360 ± 0.036	0.302 ± 0.037	0.441 ± 0.035	0.422 ± 0.036
$Q^2 > 2.5GeV^2$ $W > 1.8GeV$	0.38-0.54	0.377 ± 0.063	0.461 ± 0.061	0.501 ± 0.061	0.515 ± 0.062

Table 2.6: Measured *EMC* slopes for different kinematic cuts. The uncertainties shown in this table are the fit uncertainties only. Isoscalar corrections were applied to the ratios when extracting the slopes.

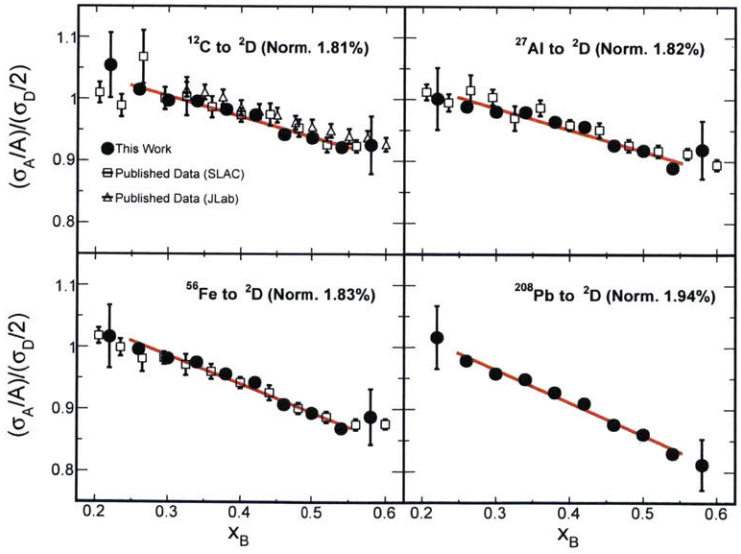

Figure 2-72: DIS cross-section ratios without applying isoscalar corrections. The carbon results are the same as before, but the results for the other nuclei are affected by the change. We also remove the isoscalar corrections for the published aluminum and iron data.

x_B	$\frac{\sigma(C)/12}{\sigma(D)/2}$ Norm. 1.81%	$\frac{\sigma(Al)/27}{\sigma(D)/2}$ Norm. 1.82%	$\frac{\sigma(Fe)/56}{\sigma(D)/2}$ Norm. 1.83%	$\frac{\sigma(Pb)/208}{\sigma(D)/2}$ Norm. 1.94%
0.22	1.054 ± 0.053	1.001 ± 0.050	1.017 ± 0.051	1.016 ± 0.051
0.26	1.015 ± 0.008	0.989 ± 0.008	0.996 ± 0.008	0.979 ± 0.008
0.30	0.997 ± 0.008	0.981 ± 0.008	0.982 ± 0.008	0.958 ± 0.008
0.34	0.996 ± 0.008	0.980 ± 0.008	0.975 ± 0.008	0.949 ± 0.007
0.38	0.983 ± 0.008	0.964 ± 0.008	0.956 ± 0.007	0.928 ± 0.007
0.42	0.974 ± 0.008	0.957 ± 0.008	0.942 ± 0.007	0.910 ± 0.007
0.46	0.943 ± 0.007	0.926 ± 0.007	0.907 ± 0.007	0.9876 ± 0.007
0.50	0.937 ± 0.008	0.918 ± 0.008	0.893 ± 0.007	0.860 ± 0.007
0.54	0.922 ± 0.008	0.890 ± 0.008	0.869 ± 0.007	0.830 ± 0.007
0.58	0.926 ± 0.047	0.919 ± 0.046	0.888 ± 0.045	0.812 ± 0.041

Table 2.7: Measured DIS per-nucleon cross-section ratios for carbon, aluminum, iron, and lead to deuterium. The error given for each point is the combined statistical and point-to-point uncertainty. The normalization uncertainty for each ratio is stated at the top of the table. The ratios shown here are the results without applying isoscalar corrections.

Target	Measured Slope	χ^2/Ndf	Fit Err.
^{12}C	0.335 ± 0.032	4.9/6	0.030
^{27}Al	0.349 ± 0.032	9.8/6	0.030
^{56}Fe	0.465 ± 0.032	7.2/6	0.029
^{208}Pb	0.529 ± 0.030	5.9/6	0.028

Table 2.8: Measured *EMC* slopes from the fit in figure 2-72. No isoscalar corrections were applied to the ratios being fit. The uncertainties shown on the extracted slopes are the combination in quadrature of the fit uncertainties, the normalization uncertainties, and half the values shown in table 2.20, table 2.21, and table 2.23. The fit uncertainty alone is also shown.

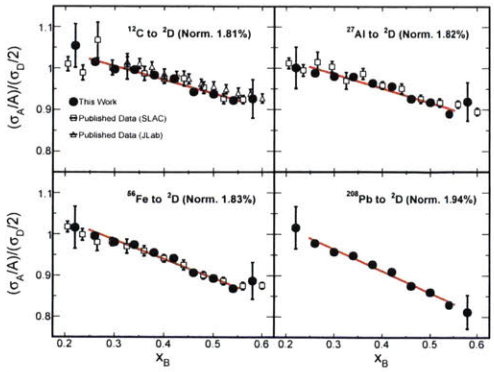

(a) DIS cross-section ratios with original binning.

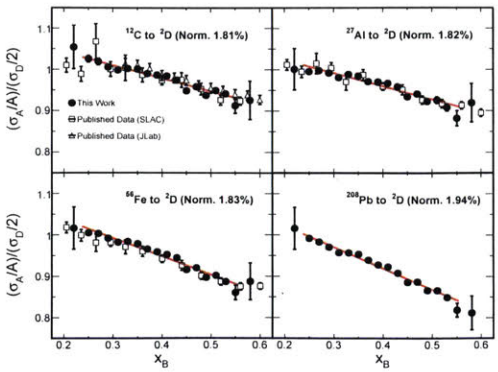

(b) DIS cross-section ratios with x2 binning.

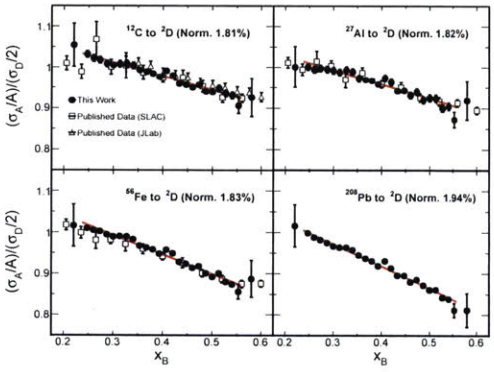

(c) DIS cross-section ratios with x3 binning.

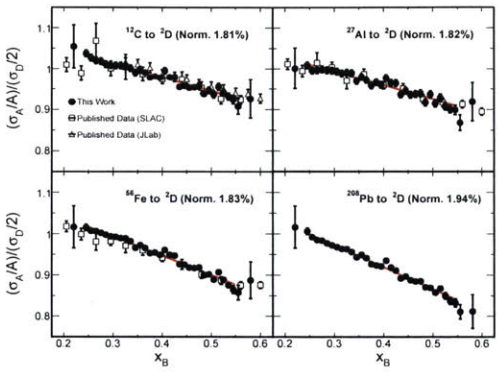

(d) DIS cross-section ratios with x4 binning.

Figure 2-73: Original binning and re-binned DIS cross-section ratios with no isoscalar corrections applied. Isoscalar corrections have also been removed from the published data.

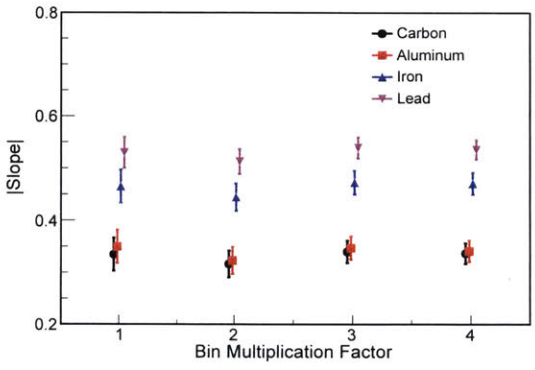

Figure 2-74: Measured EMC slopes from the fits in figure 2-73 vs. the bin size for all nuclei. No isoscalar corrections are applied to the ratios being fit. The slopes are independent of binning within uncertainties.

x_B	$\frac{\sigma(C)/12}{\sigma(D)/2}$ Norm. 1.81%	$\frac{\sigma(Al)/27}{\sigma(D)/2}$ Norm. 1.82%	$\frac{\sigma(Fe)/56}{\sigma(D)/2}$ Norm. 1.83%	$\frac{\sigma(Pb)/208}{\sigma(D)/2}$ Norm. 1.94%
0.220	1.054 ± 0.053	1.001 ± 0.050	1.017 ± 0.051	1.016 ± 0.051
0.250	1.026 ± 0.008	0.996 ± 0.008	1.005 ± 0.008	0.992 ± 0.008
0.270	1.020 ± 0.008	0.998 ± 0.008	1.004 ± 0.008	0.983 ± 0.008
0.290	1.006 ± 0.008	0.992 ± 0.008	0.992 ± 0.008	0.971 ± 0.008
0.310	0.999 ± 0.008	0.981 ± 0.008	0.982 ± 0.008	0.958 ± 0.008
0.330	1.003 ± 0.008	0.988 ± 0.008	0.984 ± 0.008	0.957 ± 0.008
0.350	1.002 ± 0.008	0.985 ± 0.008	0.979 ± 0.008	0.954 ± 0.008
0.370	0.991 ± 0.008	0.971 ± 0.008	0.966 ± 0.008	0.940 ± 0.007
0.390	0.987 ± 0.008	0.970 ± 0.008	0.959 ± 0.008	0.928 ± 0.007
0.410	0.985 ± 0.008	0.967 ± 0.008	0.953 ± 0.008	0.924 ± 0.007
0.430	0.975 ± 0.008	0.958 ± 0.008	0.945 ± 0.007	0.909 ± 0.007
0.450	0.949 ± 0.008	0.934 ± 0.008	0.916 ± 0.007	0.886 ± 0.007
0.470	0.959 ± 0.008	0.941 ± 0.008	0.920 ± 0.007	0.887 ± 0.007
0.490	0.938 ± 0.008	0.923 ± 0.008	0.897 ± 0.007	0.866 ± 0.007
0.510	0.950 ± 0.008	0.926 ± 0.008	0.902 ± 0.007	0.866 ± 0.007
0.530	0.941 ± 0.008	0.908 ± 0.008	0.887 ± 0.007	0.850 ± 0.007
0.550	0.913 ± 0.019	0.882 ± 0.018	0.861 ± 0.017	0.819 ± 0.017
0.580	0.926 ± 0.047	0.919 ± 0.046	0.888 ± 0.045	0.812 ± 0.041

Table 2.9: Measured DIS per-nucleon cross-section ratios for carbon, aluminum, iron, and lead to deuterium. All the original points (except for the first and last) have been divided into 2. The error given for each point is the combined statistical and point-to-point uncertainty. A larger point-to-point uncertainty of 2% is placed on the ratio at x_B of 0.55 due to worse statistical precision on the acceptance correction for that bin. The normalization uncertainty for each ratio is stated at the top of the table. The results are shown without applying isoscalar corrections.

x_B	$\frac{\sigma(C)/12}{\sigma(D)/2}$ Norm. 1.81%	$\frac{\sigma(Al)/27}{\sigma(D)/2}$ Norm. 1.82%	$\frac{\sigma(Fe)/56}{\sigma(D)/2}$ Norm. 1.83%	$\frac{\sigma(Pb)/208}{\sigma(D)/2}$ Norm. 1.94%
0.220	1.054 ± 0.053	1.001 ± 0.050	1.017 ± 0.051	1.016 ± 0.051
0.247	1.032 ± 0.008	1.002 ± 0.008	1.010 ± 0.008	0.999 ± 0.008
0.260	1.022 ± 0.008	0.995 ± 0.008	1.005 ± 0.008	0.988 ± 0.008
0.273	1.018 ± 0.008	0.998 ± 0.008	1.003 ± 0.008	0.982 ± 0.008
0.287	1.009 ± 0.008	0.996 ± 0.008	0.995 ± 0.008	0.975 ± 0.008
0.300	1.005 ± 0.008	0.993 ± 0.008	0.990 ± 0.008	0.967 ± 0.008
0.313	1.008 ± 0.008	0.989 ± 0.008	0.991 ± 0.008	0.964 ± 0.008
0.327	1.009 ± 0.008	0.994 ± 0.008	0.990 ± 0.008	0.964 ± 0.008
0.340	1.005 ± 0.008	0.990 ± 0.008	0.983 ± 0.008	0.958 ± 0.008
0.353	0.994 ± 0.008	0.973 ± 0.008	0.968 ± 0.008	0.945 ± 0.008
0.367	0.989 ± 0.008	0.970 ± 0.008	0.963 ± 0.008	0.937 ± 0.008
0.380	0.985 ± 0.008	0.967 ± 0.008	0.959 ± 0.008	0.931 ± 0.007
0.393	0.976 ± 0.008	0.959 ± 0.008	0.948 ± 0.008	0.919 ± 0.007
0.407	0.991 ± 0.008	0.974 ± 0.008	0.958 ± 0.008	0.931 ± 0.008
0.420	0.980 ± 0.008	0.964 ± 0.008	0.949 ± 0.008	0.914 ± 0.007
0.433	0.959 ± 0.008	0.942 ± 0.008	0.928 ± 0.007	0.896 ± 0.007
0.447	0.957 ± 0.008	0.943 ± 0.008	0.924 ± 0.007	0.896 ± 0.007
0.460	0.950 ± 0.008	0.932 ± 0.008	0.914 ± 0.007	0.880 ± 0.007
0.473	0.956 ± 0.008	0.940 ± 0.008	0.918 ± 0.007	0.886 ± 0.007
0.487	0.940 ± 0.008	0.920 ± 0.008	0.901 ± 0.007	0.872 ± 0.007
0.500	0.939 ± 0.008	0.925 ± 0.008	0.892 ± 0.007	0.861 ± 0.007
0.513	0.948 ± 0.008	0.924 ± 0.009	0.901 ± 0.007	0.861 ± 0.008
0.527	0.936 ± 0.008	0.901 ± 0.009	0.880 ± 0.007	0.843 ± 0.008
0.540	0.931 ± 0.008	0.905 ± 0.009	0.874 ± 0.007	0.839 ± 0.008
0.553	0.906 ± 0.019	0.873 ± 0.019	0.856 ± 0.017	0.812 ± 0.017
0.580	0.926 ± 0.047	0.919 ± 0.046	0.888 ± 0.045	0.812 ± 0.041

Table 2.10: Measured DIS per-nucleon cross-section ratios for carbon, aluminum, iron, and lead to deuterium. All the original points (except for the first and last) have been divided into 3. The error given for each point is the combined statistical and point-to-point uncertainty. A larger point-to-point uncertainty of 2% is placed on the ratio at x_B of 0.553 due to worse statistical precision on the acceptance correction for that bin. The normalization uncertainty for each ratio is stated at the top of the table. The results are shown without applying isoscalar corrections.

x_B	$\frac{\sigma(C)/12}{\sigma(D)/2}$ Norm. 1.81%	$\frac{\sigma(Al)/27}{\sigma(D)/2}$ Norm. 1.82%	$\frac{\sigma(Fe)/56}{\sigma(D)/2}$ Norm. 1.83%	$\frac{\sigma(Pb)/208}{\sigma(D)/2}$ Norm. 1.94%
0.220	1.054 ± 0.053	1.001 ± 0.050	1.017 ± 0.051	1.016 ± 0.051
0.245	1.038 ± 0.008	1.009 ± 0.008	1.016 ± 0.008	1.006 ± 0.008
0.255	1.027 ± 0.008	0.996 ± 0.008	1.007 ± 0.008	0.992 ± 0.008
0.265	1.021 ± 0.008	0.997 ± 0.008	1.007 ± 0.008	0.985 ± 0.008
0.275	1.019 ± 0.008	0.999 ± 0.008	1.003 ± 0.008	0.984 ± 0.008
0.285	1.011 ± 0.008	0.997 ± 0.008	0.998 ± 0.008	0.978 ± 0.008
0.295	1.009 ± 0.008	0.996 ± 0.008	0.994 ± 0.008	0.973 ± 0.008
0.305	1.008 ± 0.008	0.994 ± 0.008	0.993 ± 0.008	0.968 ± 0.008
0.315	1.008 ± 0.008	0.989 ± 0.008	0.990 ± 0.008	0.964 ± 0.008
0.325	1.008 ± 0.008	0.991 ± 0.008	0.989 ± 0.008	0.964 ± 0.008
0.335	1.002 ± 0.008	0.990 ± 0.008	0.982 ± 0.008	0.956 ± 0.008
0.345	0.991 ± 0.008	0.970 ± 0.008	0.966 ± 0.008	0.943 ± 0.008
0.355	0.998 ± 0.008	0.980 ± 0.008	0.973 ± 0.008	0.950 ± 0.008
0.365	0.991 ± 0.008	0.972 ± 0.008	0.966 ± 0.008	0.941 ± 0.008
0.375	0.978 ± 0.008	0.959 ± 0.008	0.953 ± 0.008	0.927 ± 0.008
0.385	0.981 ± 0.008	0.967 ± 0.008	0.955 ± 0.008	0.924 ± 0.007
0.395	0.978 ± 0.008	0.960 ± 0.008	0.949 ± 0.008	0.921 ± 0.007
0.405	0.996 ± 0.008	0.977 ± 0.008	0.961 ± 0.008	0.935 ± 0.008
0.415	0.980 ± 0.008	0.965 ± 0.008	0.949 ± 0.008	0.919 ± 0.008
0.425	0.980 ± 0.008	0.964 ± 0.008	0.947 ± 0.008	0.911 ± 0.007
0.435	0.955 ± 0.008	0.936 ± 0.008	0.927 ± 0.007	0.892 ± 0.007
0.445	0.958 ± 0.008	0.946 ± 0.008	0.926 ± 0.007	0.897 ± 0.007
0.455	0.953 ± 0.008	0.936 ± 0.008	0.918 ± 0.007	0.888 ± 0.007
0.465	0.954 ± 0.008	0.938 ± 0.008	0.917 ± 0.007	0.885 ± 0.007
0.475	0.957 ± 0.008	0.939 ± 0.008	0.919 ± 0.007	0.885 ± 0.008
0.485	0.938 ± 0.008	0.917 ± 0.008	0.900 ± 0.007	0.871 ± 0.008
0.495	0.947 ± 0.008	0.937 ± 0.009	0.902 ± 0.007	0.869 ± 0.008
0.505	0.936 ± 0.008	0.915 ± 0.009	0.889 ± 0.007	0.858 ± 0.008
0.515	0.956 ± 0.008	0.929 ± 0.009	0.907 ± 0.008	0.868 ± 0.008
0.525	0.941 ± 0.008	0.908 ± 0.009	0.889 ± 0.008	0.850 ± 0.008
0.535	0.932 ± 0.009	0.902 ± 0.010	0.875 ± 0.008	0.837 ± 0.008
0.545	0.924 ± 0.010	0.899 ± 0.011	0.865 ± 0.009	0.833 ± 0.010
0.555	0.908 ± 0.019	0.868 ± 0.019	0.858 ± 0.018	0.811 ± 0.017
0.580	0.926 ± 0.047	0.919 ± 0.046	0.888 ± 0.045	0.812 ± 0.041

Table 2.11: Measured DIS per-nucleon cross-section ratios for carbon, aluminum, iron, and lead to deuterium. All the original points (except for the first and last) have been divided into 4. The error given for each point is the combined statistical and point-to-point uncertainty. A larger point-to-point uncertainty of 1(2)% is placed on the ratio at x_B of 0.545(0.555) due to worse statistical precision on the acceptance correction for that bin. The normalization uncertainty for each ratio is stated at the top of the table. The results are shown without applying isoscalar corrections.

Target	Slope: Original Binning	Slope: x2 Binning	Slope: x3 Binning	Slope: x4 Binning
^{12}C	0.335 ± 0.032	0.317 ± 0.026	0.340 ± 0.022	0.337 ± 0.020
^{27}Al	0.349 ± 0.032	0.323 ± 0.026	0.347 ± 0.022	0.341 ± 0.020
^{56}Fe	0.465 ± 0.032	0.445 ± 0.026	0.472 ± 0.022	0.470 ± 0.021
^{208}Pb	0.529 ± 0.030	0.513 ± 0.024	0.539 ± 0.020	0.535 ± 0.019

Table 2.12: Measured EMC slopes from the fits in figure 2-73 for all bin sizes. No isoscalar corrections are applied to the ratios being fit. The uncertainties shown on the extracted slopes are the combination in quadrature of the fit uncertainties, the normalization uncertainties, and half the values shown in table 2.20, table 2.21, and table 2.23.

2.6.2 QE Cross-Section Ratios and a_2 Values

The final per-nucleon cross-section ratios are shown in figure 2-75. The data is divided into 14 equally sized bins in x_B in the range 0.8-2.0. We apply a kinematic cut of $Q^2 > 1.5\ GeV^2$. The total electron yield per bin for each target is shown in table 2.13 and figure 2-76. A table with the measured ratios and the associated uncertainties is shown in table 2.14. We take a weighted average of the ratios from 1.529-1.871 for each nucleus to extract the a_2 values; these measured a_2 values are shown in table 2.15.

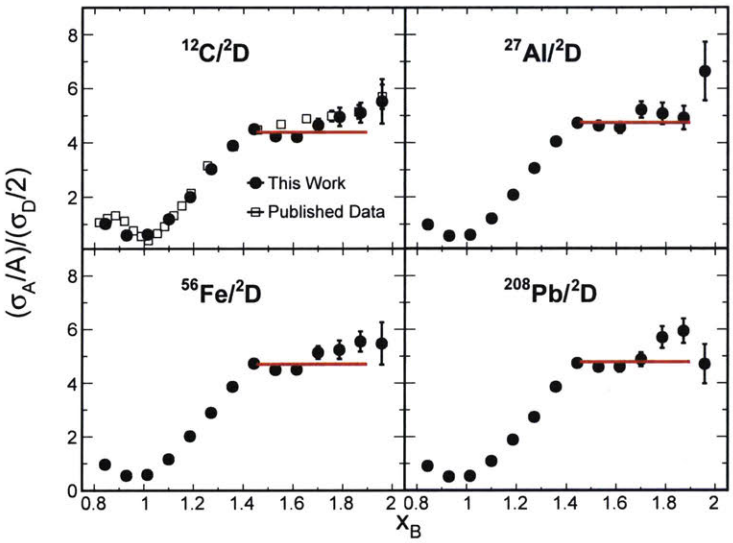

Figure 2-75: Final QE cross-section ratios to deuterium for (clockwise from top-left) carbon, aluminum, lead and iron. The error bars on the individual points are the combined statistical and point-to-point systematic uncertainties. The published data shown in the figure comes from Ref. [55].

Results With Finer Binning

In order to better characterize the scaling region, we also extract the QE ratios when we divide all bins except for the last three by a factor of 2. In order to keep the point-to-point systematics the same and account for bin migration correctly, we divide the x_B binning used for the acceptance correction by the same factor, and increase the total statistics used for the acceptance correction by the same factor. In figure 2-77

x_B	^{2}D Yield	^{12}C Yield	^{27}Al Yield	^{56}Fe Yield	^{208}Pb Yield
0.843	6.4E5 (0.12)	2.9E5 (0.18)	1.1E5 (0.29)	5.2E5 (0.14)	1.8E5 (0.23)
0.929	6.1E5 (0.13)	1.9E5 (0.23)	7.4E4 (0.37)	3.3E5 (0.17)	1.2E5 (0.29)
1.014	5.1E5 (0.14)	1.2E5 (0.28)	4.7E4 (0.46)	2.1E5 (0.22)	7.4E4 (0.37)
1.100	1.9E5 (0.23)	7.5E4 (0.36)	3.0E4 (0.58)	1.3E5 (0.28)	4.5E4 (0.47)
1.186	6.2E4 (0.40)	4.4E4 (0.48)	1.8E4 (0.74)	7.7E4 (0.36)	2.7E4 (0.61)
1.271	2.3E4 (0.65)	2.4E4 (0.64)	1.0E4 (0.99)	4.3E4 (0.48)	1.5E4 (0.81)
1.357	1.0E4 (0.99)	1.4E4 (0.86)	5643 (1.33)	2.4E4 (0.64)	8894 (1.06)
1.443	5017 (1.42)	7761 (1.14)	3227 (1.76)	1.4E4 (0.84)	5205 (1.39)
1.529	2848 (1.87)	4514 (1.49)	1992 (2.24)	8467 (1.09)	3177 (1.77)
1.614	1637 (2.47)	2804 (1.89)	1202 (2.88)	5307 (1.37)	2031 (1.77)
1.700	1036 (3.11)	1756 (2.39)	780 (3.58)	3420 (1.71)	1206 (2.88)
1.786	658 (3.89)	1186 (2.90)	483 (4.55)	2193 (2.14)	880 (3.37)
1.871	451 (4.70)	790 (3.56)	310 (5.68)	1497 (2.59)	591 (4.11)
1.957	293 (5.84)	572 (4.18)	251 (6.31)	1065 (3.06)	403 (4.98)

Table 2.13: QE yield (i.e. number of reconstructed electrons) for the various targets in each used x_B bin. The yields are shown after applying all cuts, including kinematic and vertex cuts. For a given yield, the statistical uncertainty in percent is shown in parentheses. The deuterium yield is shown with the 1 cm vertex cut, prior to any background subtraction.

and table 2.16, we show the results when we increase the points by a factor of 2. The extracted a_2 values are shown in table 2.17 and can be seen to be consistent with those extracted from the original binning.

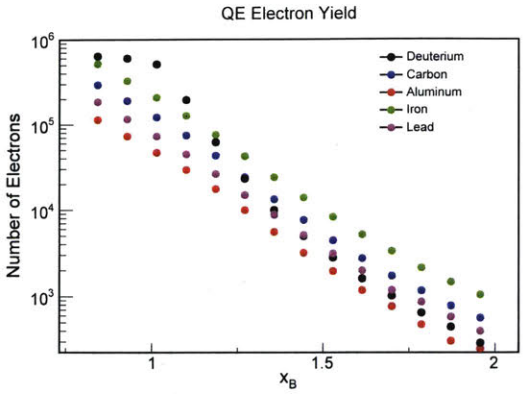

Figure 2-76: QE yield (i.e. number of reconstructed electrons) for the various targets in each used x_B bin. The yields are shown after applying all cuts, including kinematic and vertex cuts. The deuterium yield is shown with the 1 cm vertex cut, prior to any background subtraction.

x_B	$\frac{\sigma(C)/12}{\sigma(D)/2}$ Norm. 1.82%	$\frac{\sigma(Al)/27}{\sigma(D)/2}$ Norm. 1.85%	$\frac{\sigma(Fe)/56}{\sigma(D)/2}$ Norm. 1.95%	$\frac{\sigma(Pb)/208}{\sigma(D)/2}$ Norm. 2.18%
0.843	1.023 ± 0.014	0.991 ± 0.014	0.972 ± 0.013	0.918 ± 0.012
0.929	0.601 ± 0.009	0.575 ± 0.008	0.558 ± 0.008	0.521 ± 0.007
1.014	0.629 ± 0.009	0.611 ± 0.009	0.591 ± 0.008	0.544 ± 0.008
1.100	1.191 ± 0.017	1.213 ± 0.018	1.167 ± 0.016	1.100 ± 0.015
1.186	2.003 ± 0.030	2.080 ± 0.034	2.023 ± 0.030	1.890 ± 0.029
1.271	3.030 ± 0.051	3.066 ± 0.058	2.896 ± 0.047	2.733 ± 0.049
1.357	3.892 ± 0.079	4.053 ± 0.093	3.869 ± 0.074	3.860 ± 0.082
1.443	4.503 ± 0.114	4.738 ± 0.138	4.735 ± 0.113	4.745 ± 0.126
1.529	4.365 ± 0.143	4.778 ± 0.178	4.632 ± 0.143	4.746 ± 0.162
1.614	4.339 ± 0.175	4.711 ± 0.218	4.642 ± 0.176	4.750 ± 0.200
1.700	4.651 ± 0.232	5.232 ± 0.301	5.146 ± 0.241	4.881 ± 0.258
1.786	4.951 ± 0.340	5.088 ± 0.398	5.245 ± 0.342	5.705 ± 0.405
1.871	5.107 ± 0.395	4.931 ± 0.453	5.553 ± 0.403	5.942 ± 0.481
1.957	5.527 ± 1.019	6.645 ± 1.130	5.477 ± 0.992	4.711 ± 0.893

Table 2.14: Measured QE per-nucleon cross-section ratios for carbon, aluminum, iron, and lead to deuterium. The error given for each point is the combined statistical and point-to-point uncertainty. The normalization uncertainty for a each ratio is stated at the top of the table.

Target	Measured a_2	χ^2/Ndf	Fit Err.	Norm. Err.	Acc. Err.	Corr. Or. Err.	Published $\|a_2\|$
^{12}C	4.49 ± 0.17	6.3/4	0.09	0.08	0.095	0.075	4.75 ± 0.16
^{27}Al	4.86 ± 0.19	2.6/4	0.12	0.09	0.10	0.07	-
^{56}Fe	4.81 ± 0.23	9.4/4	0.09	0.09	0.155	0.105	-
^{208}Pb	4.89 ± 0.20	10.1/4	0.11	0.11	0.11	0.08	-

Table 2.15: Measured a_2 values from the fit in figure 2-75. The uncertainties shown on the extracted a_2 values are the combination in quadrature of the fit uncertainties, the normalization uncertainties, and half the values shown in tables 2.22 and 2.24. Published values are taken from Ref. [29].

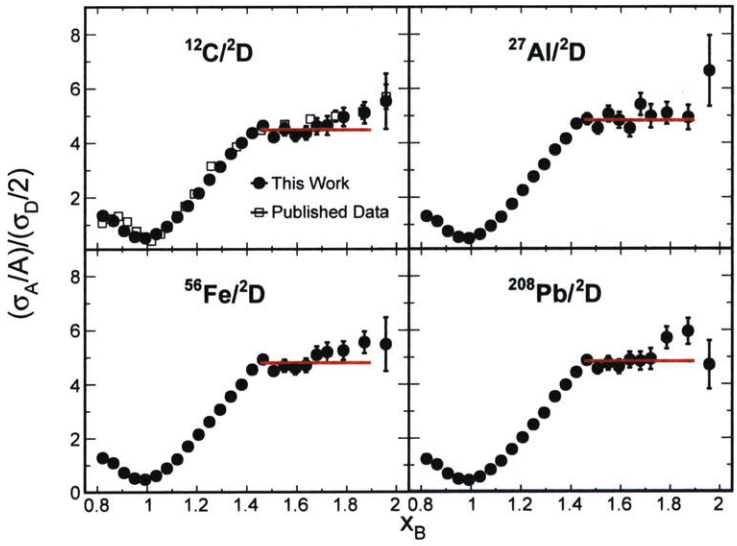

Figure 2-77: Final QE cross-section ratios to deuterium for (clockwise from top-left) carbon, aluminum, lead and iron. The error bars on the individual points are the combined statistical and point-to-point systematic uncertainties. The shown published data comes from Ref. [55]. The results shown here are equivalent to the original data with each point divided into two (except for the 3 points at highest x_B).

x_B	$\frac{\sigma(C)/12}{\sigma(D)/2}$ Norm. 1.82%	$\frac{\sigma(Al)/27}{\sigma(D)/2}$ Norm. 1.85%	$\frac{\sigma(Fe)/56}{\sigma(D)/2}$ Norm. 1.95%	$\frac{\sigma(Pb)/208}{\sigma(D)/2}$ Norm. 2.18%
0.821	1.335 ± 0.018	1.304 ± 0.018	1.278 ± 0.017	1.221 ± 0.017
0.864	1.140 ± 0.016	1.114 ± 0.016	1.087 ± 0.015	1.018 ± 0.014
0.907	0.777 ± 0.011	0.747 ± 0.011	0.727 ± 0.010	0.677 ± 0.010
0.950	0.557 ± 0.008	0.531 ± 0.008	0.517 ± 0.007	0.484 ± 0.007
0.992	0.509 ± 0.007	0.487 ± 0.007	0.474 ± 0.007	0.436 ± 0.006
1.036	0.660 ± 0.009	0.635 ± 0.010	0.610 ± 0.009	0.561 ± 0.008
1.079	0.928 ± 0.014	0.937 ± 0.015	0.885 ± 0.013	0.825 ± 0.013
1.121	1.278 ± 0.019	1.267 ± 0.021	1.224 ± 0.018	1.145 ± 0.018
1.164	1.686 ± 0.027	1.739 ± 0.031	1.704 ± 0.026	1.576 ± 0.026
1.207	2.152 ± 0.037	2.245 ± 0.044	2.145 ± 0.035	2.013 ± 0.037
1.250	2.651 ± 0.050	2.746 ± 0.059	2.613 ± 0.047	2.495 ± 0.050
1.293	3.128 ± 0.066	3.195 ± 0.079	3.067 ± 0.061	2.926 ± 0.066
1.336	3.604 ± 0.085	3.738 ± 0.103	3.552 ± 0.079	3.532 ± 0.089
1.379	4.002 ± 0.109	4.144 ± 0.133	3.992 ± 0.102	3.963 ± 0.115
1.421	4.362 ± 0.136	4.690 ± 0.171	4.544 ± 0.133	4.428 ± 0.147
1.464	4.634 ± 0.164	4.869 ± 0.203	4.920 ± 0.163	4.872 ± 0.184
1.507	4.209 ± 0.169	4.529 ± 0.212	4.490 ± 0.169	4.563 ± 0.194
1.550	4.501 ± 0.228	5.062 ± 0.288	4.684 ± 0.225	4.765 ± 0.252
1.593	4.289 ± 0.226	4.828 ± 0.291	4.590 ± 0.227	4.634 ± 0.256
1.636	4.368 ± 0.251	4.525 ± 0.307	4.701 ± 0.252	4.883 ± 0.294
1.679	4.610 ± 0.301	5.408 ± 0.406	5.088 ± 0.310	4.847 ± 0.337
1.721	4.644 ± 0.348	4.978 ± 0.431	5.188 ± 0.363	4.924 ± 0.389
1.786	4.951 ± 0.340	5.088 ± 0.398	5.245 ± 0.342	5.705 ± 0.405
1.871	5.107 ± 0.395	4.931 ± 0.453	5.553 ± 0.403	5.942 ± 0.481
1.957	5.527 ± 1.019	6.645 ± 1.303	5.477 ± 0.992	4.711 ± 0.893

Table 2.16: Measured QE per-nucleon cross-section ratios for carbon, aluminum, iron, and lead to deuterium for the binning shown in figure 2-77. The error given for each point is the combined statistical and point-to-point uncertainty. The normalization uncertainty for each ratio is stated at the top of the table.

Target	Measured Slope	χ^2/Ndf	Fit Err.
^{12}C	4.49 ± 0.17	9.2/8	0.079
^{27}Al	4.83 ± 0.18	6.3/8	0.098
^{56}Fe	4.80 ± 0.22	12.4/8	0.079
^{208}Pb	4.84 ± 0.20	12.7/8	0.090

Table 2.17: Measured a_2 values from the fits in figure 2-77. The uncertainties shown on the extracted a_2 values are the combination in quadrature of the fit uncertainties, the normalization uncertainties, and half the values shown in tables 2.22 and 2.24. The fit uncertainty alone is also shown.

2.6.3 Systematic Uncertainties

The systematic uncertainties are divided into two groups: the point-to-point uncertainties are uncorrelated between different bins and are treated in the same manner as the statistical uncertainties; the normalization uncertainties affect the overall scale but do not vary between kinematic points.

In table 2.18 (2.19), the sources of systematic uncertainties and their effect on the final per-nucleon cross-section ratios are shown for DIS (QE) events. These uncertainties are discussed in some detail in the following subsections.

Source	Point-to-Point (%)	Normalization (%)
Beam Charge/ Time-Dependent Instabilities	-	1.0
Target Thickness and Cuts	-	1.42-1.58
Acceptance Corrections	0.6 (5)	-
Radiative Corrections	-	0.5
Coulomb Corrections	-	0.1
Bin-Centering Corrections	0.5	-
Total	0.78	1.81-1.94

Table 2.18: Sources of systematic uncertainties on the final DIS ratios, and their relative contributions. For the acceptance uncertainty, the value listed in the parenthesis is for the first and last x_B bins.

Source	Point-to-Point (%)	Normalization (%)
Beam Charge/ Time-Dependent Instabilities	-	1.0
Target Thickness and Cuts	-	1.42-1.58
Acceptance Corrections	1.2 (2.5, 10)	-
Radiative Corrections	-	0.5
Coulomb Corrections	-	0.2-1.0
Bin-Centering Corrections	0.5	-
Kinematic Corrections	0.3	-
Total	1.33	1.82-2.18

Table 2.19: Sources of systematic uncertainties on the final QE ratios, and their relative contributions. For the acceptance uncertainty, the values listed in the parenthesis are for the last two x_B bins, respectively.

Beam Charge and Time-Dependent Instabilities

Since we combine all the deuterium runs when calculating the cross-section ratios, we are sensitive to changes in the beam charge monitoring devices, fluctuations in the cryotarget, and changes to the *CLAS* detector components over the run period. Since this uncertainty will affect all points in the same way, it is a normalization uncertainty. The simplest way to estimate this uncertainty is by looking at the systematic changes in the normalized yield for the deuterium target in figure 2-43.

We make a histogram of the percent deviation of the normalized yield for every run from the mean weighted yield for all runs (figure 2-78). The fitted width of the main peak in this plot is approximately 0.65%. In addition, the standard deviation of the distribution for all the runs used in the final analysis is 1.2%. So, we choose to place a final uncertainty of 1% on the ratio.

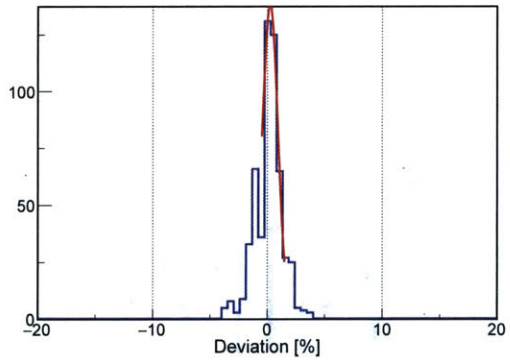

Figure 2-78: Percent deviation from the mean of the charge normalized deuterium yield for every run. We find that the width of the main peak is approximately 0.65%. The standard deviation of the distribution for all the runs used in the final analysis is 1.2%.

Target Thickness and Vertex Cuts

We place a normalization uncertainty on our measured ratios due to the target thicknesses and software vertex cuts.

The uncertainty in the *EG2c* cryotarget thickness has been estimated to be 1.0% [56]. The thicknesses of the solid targets were measured to about the 1 micron level [35]. This translates to a relative uncertainty of 0.1-0.7%.

For the solid targets, since we apply a vertex cut much larger than the solid target reconstruction resolution, there is no significant cut uncertainty.

For the cryotarget, in the DIS case we apply a vertex cut with a full width of 3 cm. We then vary this cut by 0.25 cm and look at the change in the windows-subtracted yield in each x_B bin. We find that the yield always increases with a wider cut for all bins. The maximum change in the yield is 1.0%. In addition, we note that if we calculate the cross-section ratios using the 1 cm cut inside the deuterium, all the ratios increase by about 1.5%. We therefore take 1.0% as our $\pm 1\sigma$ normalization uncertainty.

We study the effect of using the 1 cm cut for the DIS events on the measured *EMC* slopes, and we include this effect in the uncertainty on the slopes. The cross-section ratios with the 1 cm cut are shown in figure 2-79. The difference between the slopes using the 3 cm cut compared to the 1 cm cut is shown in table 2.20.

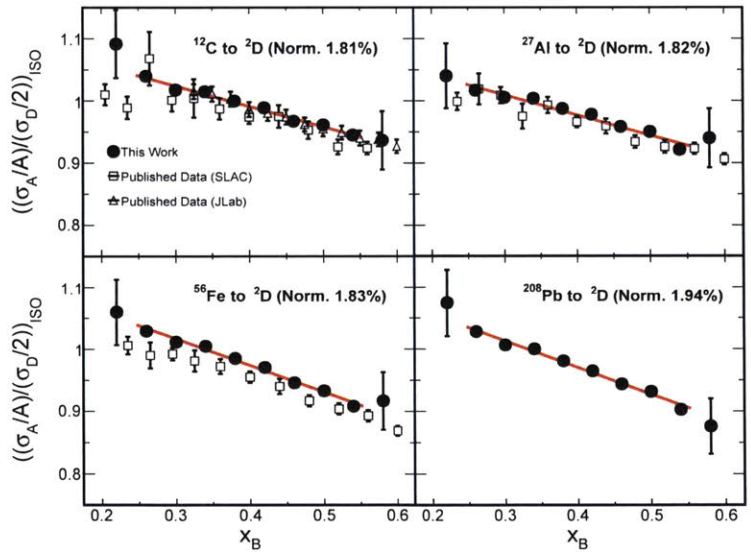

Figure 2-79: Measured DIS per-nucleon cross-section ratios to deuterium for (clockwise from top-left) carbon, aluminum, lead and iron. The deuterium data is extracted using a vertex cut with a full width of 1 cm. Note how all the ratios shift up by about 1.5% compared to those in figure 2-69. The error bars on the individual points are the combined statistical and point-to-point systematic uncertainties. The data is shown here with the original binning and the application of isoscalar corrections. The published data comes from Refs. [18, 19].

In the QE case, we apply a cut of 1 cm in the center of the target. The main

Target	$\lvert\Delta Slope\rvert$
^{12}C	0.008
^{27}Al	0.007
^{56}Fe	0.006
^{208}Pb	0.006

Table 2.20: The differences in the measured *EMC* slopes using a 1 cm cryotarget vertex cut compared to a 3 cm cut.

question here concerns the reconstruction 'optics' (i.e. is the 2 cm long cryo-target really reconstructed to the correct length?). To test this, we look at the reconstructed window locations for the empty target runs (figure 2-46) and compare to the ideal target length. We make Gaussian fits to the two target foils for the empty target runs, and calculate the deviation of the difference in the fit means from the ideal target length. We repeat this fit several times with different ranges around the peaks, and monitor how well the peaks are fitted. In figure 2-80, we show the percent deviation from the ideal target length vs. the used fit range around each peak. We do not see any region where the deviation is constant. Thus we only consider the points where both fits' calculated χ^2 are reasonable, indicating that using a Gaussian fit is valid. Given the spread of the points in this range, we place a conservative uncertainty of 1% on our 1 cm cut.

For the effect on the cross-section ratios, we combine the cryotarget thickness uncertainty, the solid-target thickness uncertainty, and the vertex cut uncertainties. This gives a normalization uncertainty of 1.42-1.58% in both the DIS and QE regions.

Acceptance Corrections and Bin Migration

We place a point-to-point uncertainty based on the statistical uncertainty on the extracted acceptance correction factors. As noted in section 2.5.3, we limited the uncertainty in the acceptance correction factor to 0.75% (3.0%) in the DIS (QE) region in each two-dimensional bin. When summing the data into a one-dimensional function of x_B, this uncertainty will be decreased by the square-root of the number of bins in the sum due to our use of a uniform monte-carlo generator. In the DIS (QE)

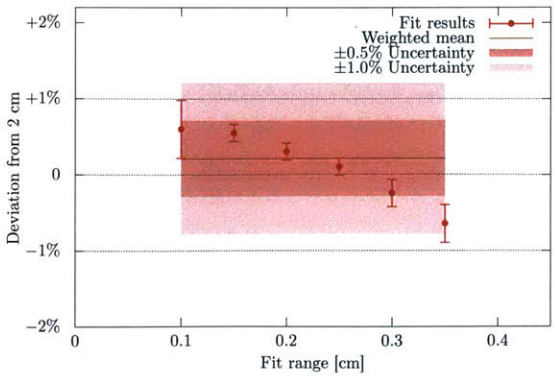

Figure 2-80: Percent deviation of the target length determined by the fit from the assumed cryotarget length vs. Gaussian fit range around the peak.

region, for each x_B point, we have about 9 (16) acceptance bins. This allows us to place an uncertainty of 0.25% (0.75%) on the DIS (QE) region. (The uncertainties are higher near the edges of the acceptance.) Since the acceptance correction factors are applied to the deuterium and solid target separately, the effect on the cross-section ratios is 0.35% (1.06%) for the DIS (QE) region. In addition, we place a 0.5% uncertainty on the acceptance due to imperfections in the detector simulation.

It is also important to consider the effects of bin migration. In figure 2-81, we show the resolution on x_B for events generated in different x_B ranges. The plots cover the lower range of the QE analysis region. As can be seen, the resolution becomes worse with increasing x_B. This trend continues to larger x_B values and down to the DIS region. In the DIS case, the resolution is better than our initially chosen bin size of 0.04, and the cross-sections do not vary as rapidly with x_B (figure 2-55). The resolution becomes similar to the bin size when we calculate the ratios using smaller bins. In the QE region, however, the cross-sections fall quickly with increasing x_B (figure 2-56), and the x_B resolution degrades.

We correct for bin migration effects by using our model cross-sections when applying the acceptance corrections. Then we consider the question of how much would bin migration have affected the final ratios if no correction were applied. We study this by performing the acceptance corrections using the uniform generator without weighting the events with the cross-section model. The difference in the measured

EMC slopes and a_2 values when using the two types of acceptance maps are shown in tables 2.21 and 2.22, respectively. We include this difference when determining the final uncertainties on the *EMC* slopes and a_2 values.

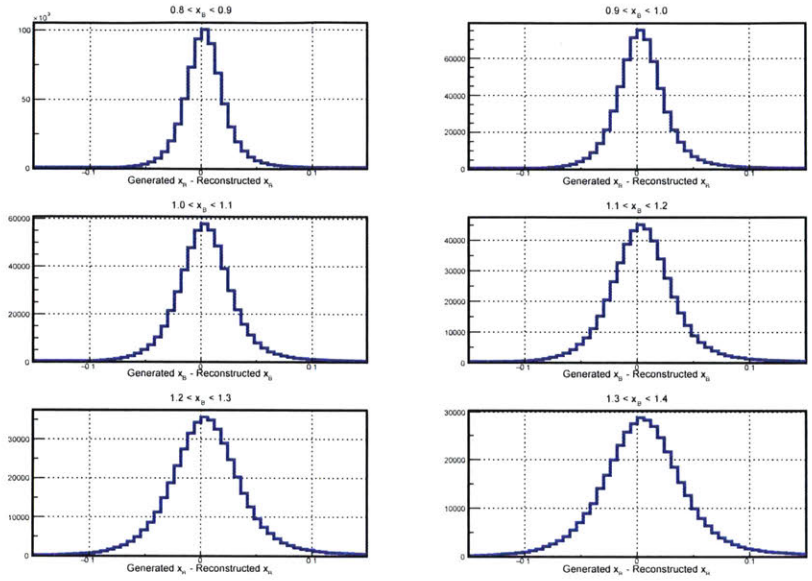

Figure 2-81: Resolutions for x_B determined from the *CLAS* simulation in the x_B range 0.8-1.4 for bins of size 0.1.

Target	$\lvert\Delta Slope\rvert$
^{12}C	0.005
^{27}Al	0.006
^{56}Fe	0.006
^{208}Pb	0.005

Table 2.21: The differences in the measured *EMC* slopes using the unweighted compared to the weighted acceptance maps.

Radiative, Coulomb, and Bin-Centering Corrections

Point-to-point uncertainties due to the radiative corrections can arise due to detector resolution and bin migration. We study this effect using the simulation. In figure 2-82 (2-83), we show the generated and reconstructed weighted simulation in the DIS (QE) region after applying acceptance corrections to the reconstructed events. Then we consider the average radiative correction in each bin using both the generated events

Target	$\lvert\Delta a_2\rvert$
^{12}C	0.19
^{27}Al	0.20
^{56}Fe	0.31
^{208}Pb	0.22

Table 2.22: The differences in the measured a_2 values using the unweighted compared to the weighted acceptance maps.

(i.e. the true correction) and the acceptance-corrected reconstructed events (i.e. the used correction). We take the ratio of the true correction to the used correction to determine the size of the resolution effect (figures 2-84 and 2-85). We see that the effect cancels in the final cross-section ratio. Point-to-point uncertainties not due to the resolution are also expected to cancel in the ratio [19]. The normalization uncertainty on the cross-section ratios due to radiative corrections is estimated to be 0.5% [18, 19].

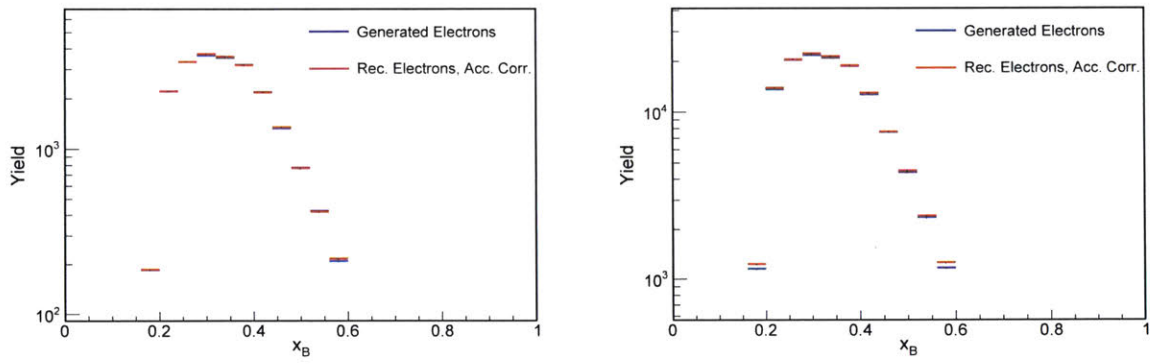

(a) Deuterium Target

(b) Solid (carbon) Target

Figure 2-82: DIS weighted simulation: generated and acceptance-corrected reconstructed events.

The coulomb corrections range from 0-5% for the DIS region and from 0-15% for the QE region. There is a 10% uncertainty in the coulomb potential [53]. To study the effect of this uncertainty on ΔE on the coulomb correction factors, we recalculate the factors with ΔE changed by 10% [57]. For the DIS region, this changes the coulomb correction factor by a maximum of only 0.1%. For the QE region, the factor changes by a maximum of 0.2% for carbon, 0.4% for aluminum, 0.7% for iron, and

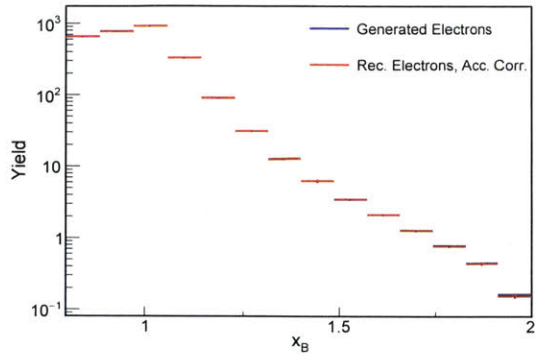

(a) Deuterium Target

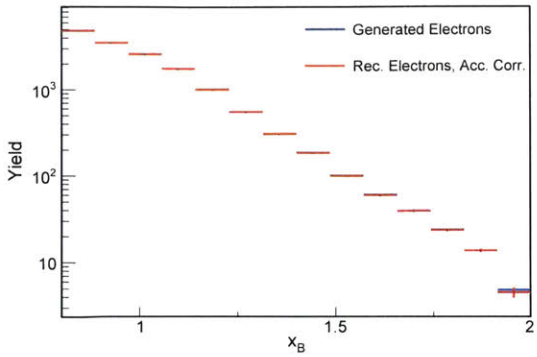

(b) Solid (carbon) Target

Figure 2-83: QE weighted simulation: generated and acceptance-corrected reconstructed events.

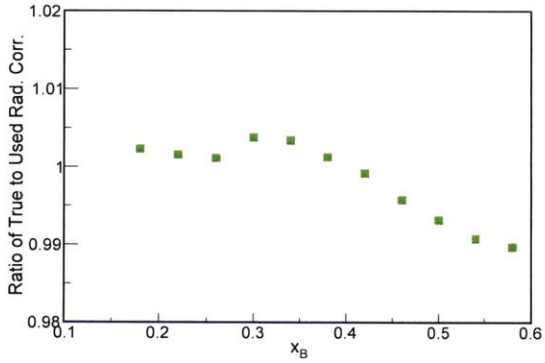

(a) Deuterium Target

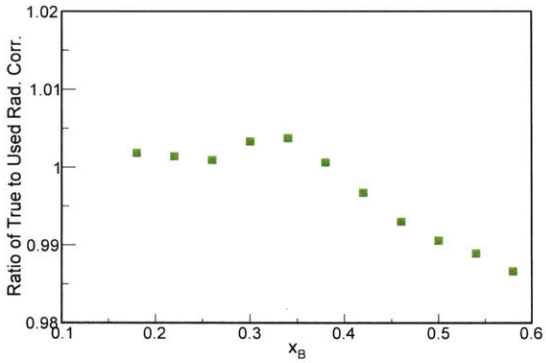

(b) Solid (carbon) Target

Figure 2-84: DIS ratio of true to used average radiative correction.

1.0% for lead. Although there is some x_B dependence to the amount the correction factor changes, the changes are correlated. So, we choose to conservatively use the maximum change for each target as a normalization uncertainty.

The uncertainty due to the bin-centering correction will depend on the bin size chosen. Our original binning was similar to the previously published results [57, 58]. Following these results, we place a 0.5% point-to-point uncertainty on the bin-centering correction factor. When we divide our original bins into smaller bins, we conservatively choose to keep the same uncertainty.

As discussed in section 2.5.7, it is also possible to apply the bin-centering corrections prior to some to the other corrections. The differences in the measured *EMC*

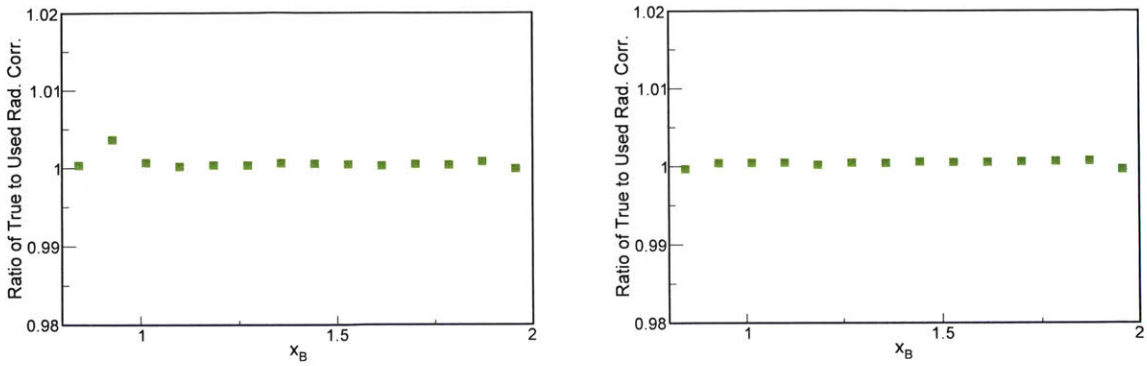

(a) Deuterium Target

(b) Solid (carbon) Target

Figure 2-85: QE ratio of true to used average radiative correction.

slopes and a_2 values when applying the corrections in a different order are shown in tables 2.23 and 2.24, respectively.

Target	$\lvert\Delta Slope\rvert$
^{12}C	0.015
^{27}Al	0.016
^{56}Fe	0.021
^{208}Pb	0.007

Table 2.23: The differences in the measured *EMC* slopes after changing the order of the corrections.

Target	$\lvert\Delta a_2\rvert$
^{12}C	0.15
^{27}Al	0.14
^{56}Fe	0.21
^{208}Pb	0.16

Table 2.24: The differences in the measured a_2 values after changing the order of the corrections.

Kinematic Corrections

For the QE case, we estimated the maximum amount that the electron momentum may be reconstructed incorrectly in section 2.3.4. To check the effect of this potential mis-reconstruction on the cross-section ratios, we look at how much every measured

cross-section ratio changes if we shift the momentum by 20 MeV/c. We find that the ratio changes between 0.2-0.3%. So, we place a point-to-point uncertainty of 0.3% on all bins.

We applied momentum corrections to the scattered electron for the DIS region. These corrections are on the order of 0.5%, and we do not place any uncertainty on this correction.

Polar angle corrections are on the order of 0.2%, and are applied to both the DIS and QE analyses. We also do not place any uncertainty on this correction.

2.6.4 The EMC Effect and Short Range Correlations

As discussed in chapter 1, the slope of the *EMC* effect is known to linearly correlate with a_2 [28, 29]. Based on this correlation and the isospin dependence of nucleon SRCs, we model the *EMC* effect as being due entirely to the modification of *np*-SRC pairs. We can then write the structure function of a nucleus A, $F_2^A(x_B, Q^2)$, as

$$\begin{aligned} F_2^A &= (Z - n_{SRC}^A)F_2^p + (N - n_{SRC}^A)F_2^n + n_{SRC}^A(F_2^{p*} + F_2^{n*}) \\ &= ZF_2^p + NF_2^n + n_{SRC}^A(\Delta F_2^p + \Delta F_2^n)\,, \end{aligned} \tag{2.19}$$

where n_{SRC}^A is the number of *np*-SRC pairs in a nucleus A, $F_2^{p(n)}(x_B, Q^2)$ is the free proton (neutron) structure function, and $F_2^{p*(n*)}(x_B, Q^2)$ is the modified proton (neutron) structure function. In the above equation, $\Delta F_2^p = F_2^{p*} - F_2^p$ and $\Delta F_2^n = F_2^{n*} - F_2^n$. (Note that the definition of F_2^A used here is equivalent to $A \cdot F_2^A$ in some other works.)

In the model quantified in equation 2.19, the term $F_2^{p*} + F_2^{n*}$ is nucleus independent (i.e. universal). The question is then whether we can consistently describe the *EMC* effect for all nuclei using this model.

We can first apply equation 2.19 to deuterium as

$$F_2^d = F_2^p + F_2^n + n_{SRC}^d(\Delta F_2^p + \Delta F_2^n)\,, \tag{2.20}$$

and form *EMC* ratios ($\frac{F_2^A/A}{F_2^d/2}$). Since the free neutron structure function is not well constrained, we can use this equation to solve for F_2^n. In our model, the *EMC* ratios are then written as

$$\frac{F_2^A/A}{F_2^d/2} = (a_2 - 2\frac{N}{A})(n_{SRC}^d \frac{\Delta F_2^p + \Delta F_2^n}{F_2^d}) + 2 \cdot \frac{Z-N}{Z+N} \cdot \frac{F_2^p}{F_2^d} + 2\frac{N}{A}\,, \tag{2.21}$$

with $a_2 = \frac{n_{SRC}^A/A}{n_{SRC}^d/2}$. Notice in this equation, the nucleus-independent quantity is $n_{SRC}^d \frac{\Delta F_2^p + \Delta F_2^n}{F_2^d}$.

Because we eliminated F_2^n when calculating the *EMC* ratio in equation 2.21, we are

left with a term that depends on $\frac{F_2^p}{F_2^d}$. This quantity has almost no Q^2 dependence (like the *EMC* effect) and is well-constrained as a function of x_B [59]. We can parametrize the data from Ref. [59] using a 3^{rd} order polynomial (figure 2-86). For every nucleus and x_B point for which there is an *EMC* measurement, we can now extract the quantity $n_{SRC}^d \frac{\Delta F_2^p + \Delta F_2^n}{F_2^d}$ as

$$n_{SRC}^d \frac{\Delta F_2^p + \Delta F_2^n}{F_2^d} = \frac{\frac{F_2^A}{F_2^d} - (Z-N)\frac{F_2^p}{F_2^d} - N}{(A/2)a_2 - N}. \tag{2.22}$$

In figure 2-87, we plot both the measured *EMC* ratios and the quantity calculated using equation 2.22. As can be seen in the figure, the quantity $n_{SRC}^d \frac{\Delta F_2^p + \Delta F_2^n}{F_2^d}$ is indeed universal (i.e. nucleus independent). We quantify the universality in figure 2-88, where we show the slopes of both the measured *EMC* ratios and our universal modification function.

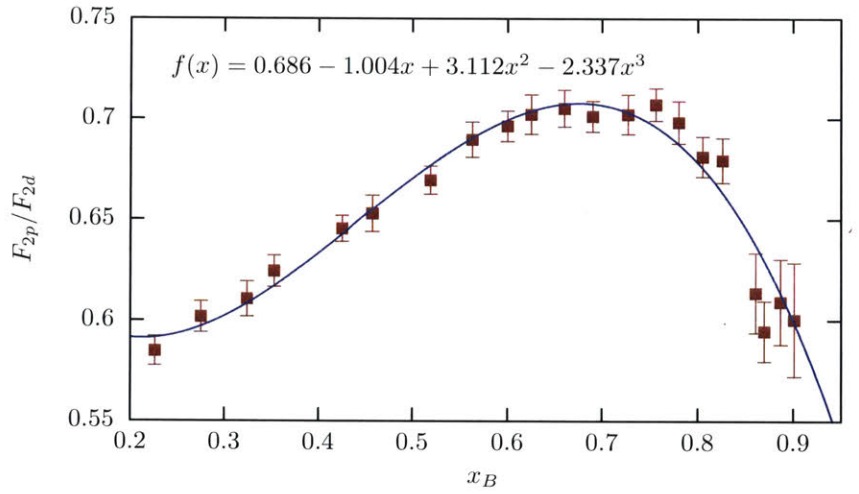

Figure 2-86: Ratio of proton to deuteron structure function. The points are taken from Ref. [59]. For this work we use the continuous parametrization shown in the figure.

To gain further insight into the *EMC*-SRC relationship, we calculate two additional quantities, the per-neutron and per-proton cross-section ratios: $\left(\frac{\sigma(A)/N}{\sigma(D)/1}\right)$ and $\left(\frac{\sigma(A)/Z}{\sigma(D)/1}\right)$. This allows us to calculate the per-neutron and per-proton EMC slopes and a_2 values as

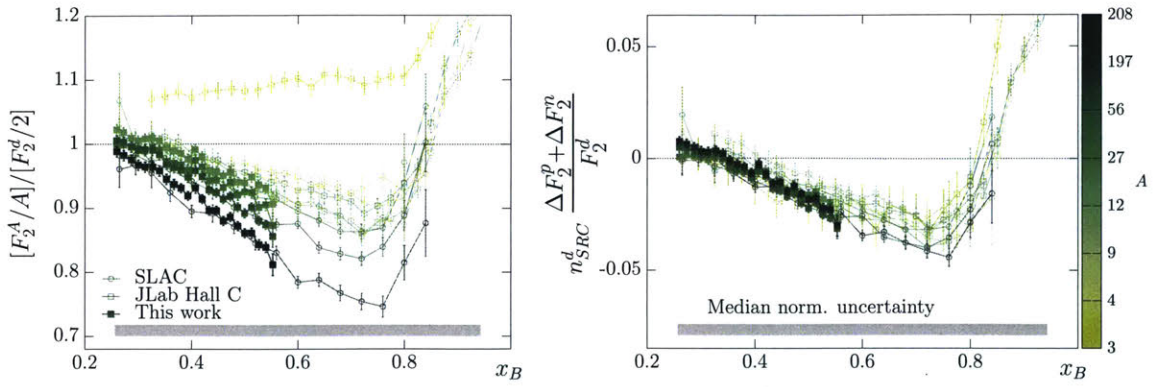

Figure 2-87: Left: Measured *EMC* ratios from three data sets: Ref. [18], Ref. [19] and this work. The ^3He data from Ref. [18] is re-normalized up by 3% following the global fits performed in Ref. [60]. Right: The universal modification function from our model calculated using equation 2.22.

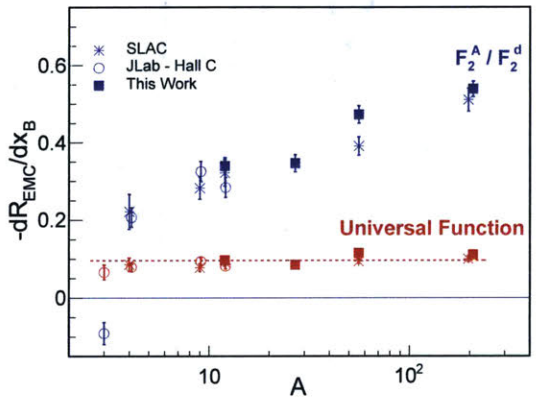

Figure 2-88: Slopes of the measured *EMC* ratios (blue) and the universal modification function (red) from figure 2-87.

$$
\begin{aligned}
R_{EMC}^n &= R_{EMC}^A \times A/N \times 1/2\,, \\
R_{EMC}^p &= R_{EMC}^A \times A/Z \times 1/2\,, \\
a_2^n &= a_2^A \times A/N \times 1/2\,, \\
a_2^p &= a_2^A \times A/Z \times 1/2\,.
\end{aligned}
\tag{2.23}
$$

In the above equation $R_{EMC}^{A(n,p)}$ represents the per-nucleon (neutron, proton) *EMC* slope, and $a_2^{A(n,p)}$ represents the per-nucleon (neutron, proton) SRC scaling coefficient.

Our model makes the following prediction for the per-neutron *EMC* ratios:

$$\frac{F_2^A/N}{F_2^d/1} = (a_2^n - 1)(n_{SRC}^d \frac{\Delta F_2^p + \Delta F_2^n}{F_2^d}) + (\frac{Z}{N} - 1) \cdot \frac{F_2^p}{F_2^d} + 1\,, \tag{2.24}$$

and for the per-proton ratios:

$$\frac{F_2^A/Z}{F_2^d/1} = (a_2^p - \frac{N}{Z})(n_{SRC}^d \frac{\Delta F_2^p + \Delta F_2^n}{F_2^d}) + (\frac{Z}{N} - 1) \cdot \frac{F_2^p}{F_2^d} + \frac{N}{Z}\,. \tag{2.25}$$

These equations make predictions for the per-neutron and per-proton *EMC* slopes as a function of the per-neutron and per-proton a_2 values, respectively. In figure 2-89, we plot the per-neutron (proton) *EMC* slope vs. the per-neutron (proton) a_2. We do this for the measured data and compare the results to our model's predictions. For example, the dashed curves in the plots show our model's predictions for nuclei with N = Z. We also show what our model predicts for nuclei with Z = 2N (e.g. ^3He) and for nuclei with N > Z. The model predictions are in agreement with the data.

The reason we calculate these per-neutron and per-proton quantities is because an SRC-based *EMC* effect should show saturation for the neutrons and continued growth for the protons [61]. The per-neutron and per-proton quantities allow us to see whether there is this saturation and growth behavior.

In order to check for this behavior, it is useful to apply isoscalar corrections to the *EMC* data. We can use the extracted universal modification function along with equation 2.20 to make a calculation of F_2^n/F_2^p. This calculation is shown in figure 2-90. We can then apply isoscalar corrections to the data in a model-consistent way (figure 2-91). In figure 2-92, we show the *EMC*-SRC correlation plot after applying isoscalar corrections to the *EMC* data using the parametrization extracted from our model.

As can be seen in figure 2-92, the per-neutron *EMC* effect saturates beginning at carbon, while the per-proton effect continues to grow all the way up to lead. This saturation and growth is consistent with a SRC-based *EMC* effect as well as the expectation of our model.

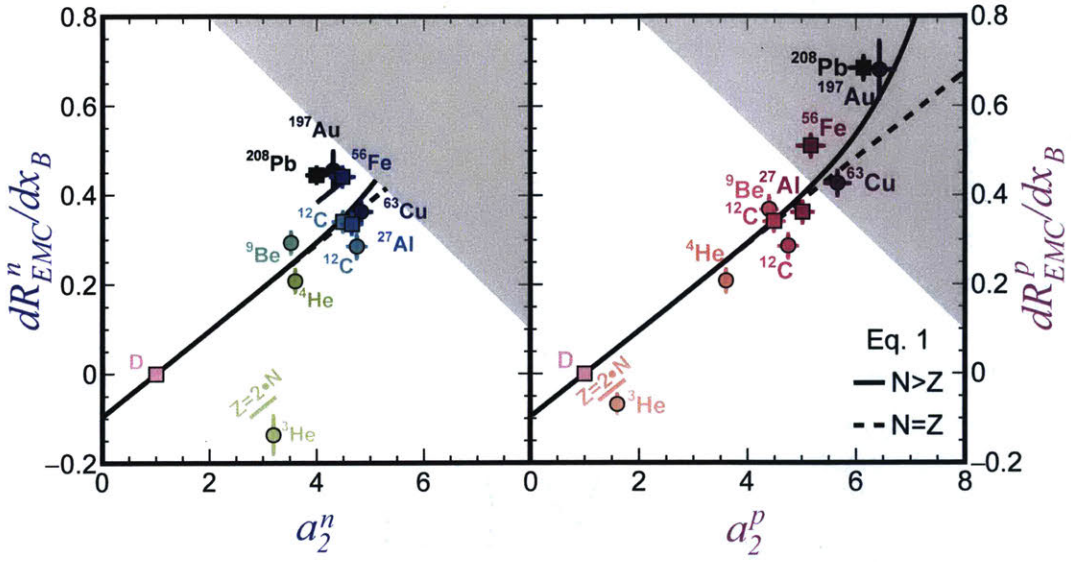

Figure 2-89: Left (Right): Per-neutron (proton) *EMC* slope vs. the per-neutron (proton) a_2. The square data points are extracted from the cross-section ratio measurements performed in this thesis; the circular data points are extracted from previously published data. The *EMC* slopes are extracted without applying isoscalar corrections to the DIS ratios. The dashed curves show our model's predictions for isoscalar nuclei, while the solid curves show predications for various non-isoscalar N/Z values. The shaded triangle in the top right corner of each panel shows the area of the plots only occupied by the per-proton quantities.

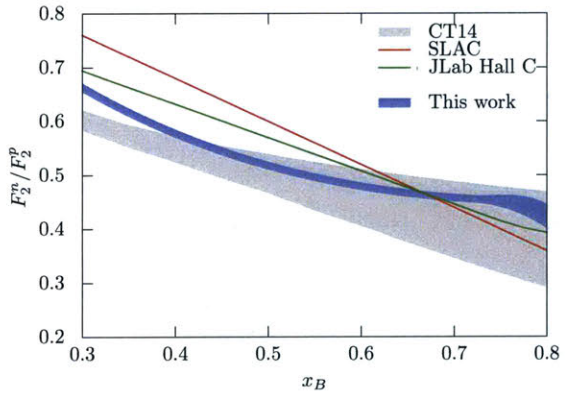

Figure 2-90: Extraction of the free neutron to proton structure function ratio using the model developed in this section (blue band). Previous parametrizations are also shown on the plot: *SLAC* [19], *JLab Hall C* [18], and *CT14* [62].

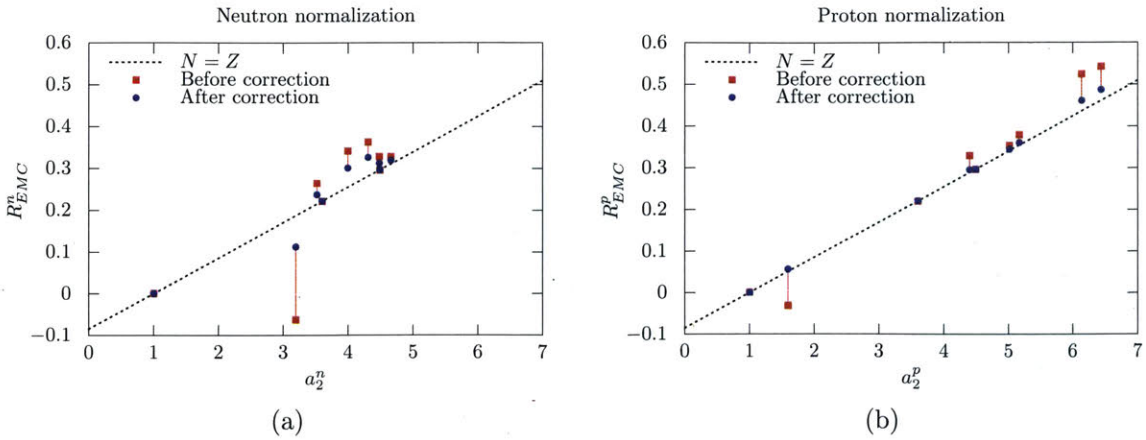

Figure 2-91: Left: Prediction of our model for the per-neutron *EMC* slopes after applying isoscalar corrections. Right: Prediction of our model for the per-proton *EMC* slopes after applying isoscalar corrections.

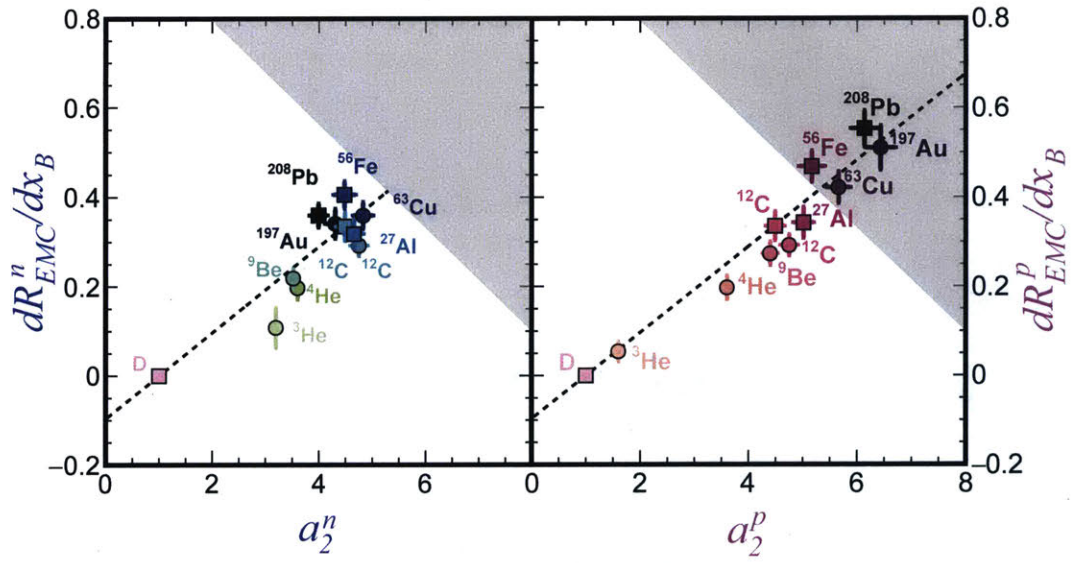

Figure 2-92: Per-neutron (proton) *EMC* slope vs. the per-neutron (proton) a_2. The square data points are extracted from the cross-section ratio measurements performed in this thesis; the circular data points are extracted from previously published data. The *EMC* slopes are extracted from isoscalar-corrected DIS ratios. The dashed curves show our model's predictions for isoscalar nuclei. The shaded triangle in the top right corner of each panel shows the area of the plots only occupied by the per-proton quantities.

Chapter 3

Measuring the Elastic *ep* Cross-Section in Hall A at JLab

The *GMp* experiment [30] was performed in Hall A at JLab during the spring and fall of 2016. It was the first experiment completed in Hall A after the 12 GeV CEBAF upgrade. The data collected by the *GMp* experiment during the spring and fall 2016 run periods is shown in figure 3-1. The values of G_{Mp} shown for the red, green, and blue points are arbitrary; the points are used to show the Q^2 value and the error bar for each measured cross-section. For the majority of kinematic points, the statistical uncertainty is less than 1%. The total systematic uncertainty (point-to-point and normalization) is expected to be approximately 2%.

In order to extract elastic cross-sections and the form factors, the experiment needs to reconstruct for every event the detected particle's type, reaction vertex, and momentum vector. The experiment also needs to know the efficiencies of the various detector and data-acquisition components in order to make a precise measurement. This chapter will discuss the experimental setup and the calibrations used to correctly reconstruct the events. We will also briefly discuss how a cross-section is calculated for a small-acceptance spectrometer once the events are correctly reconstructed. Then the chapter will discuss the detailed efficiency studies which we conducted for the *GMp* experiment. Lastly, we will present preliminary cross-section results for the high Q^2 data.

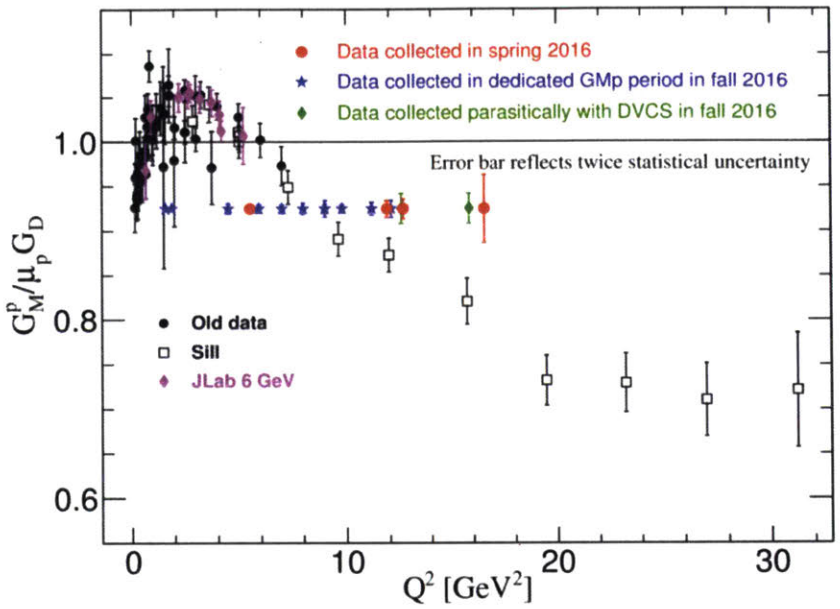

Figure 3-1: The data collected during the Spring and Fall 2016 run periods. Unlike for the shown published data, for the *GMp* data the form factor value displayed is arbitrary. Figure taken from Ref. [63].

3.1 Experimental Setup

Hall A at JLab

The High-Resolution Spectrometers

Hall A has two spectrometers, the right arm (RHRS) and the left arm (LHRS) [64]. These arms are almost identical in architecture and operation, and they function independently of one another. The spectrometers are of a Quadrupole-Quadrupole-Dipole-Quadrupole design. Due to the spectrometers' optics design and large momentum dispersion, the spectrometers have an excellent momentum resolution of 10^{-4}.

Particles which pass through the HRSs are detected and have their trajectories reconstructed using standard detector packages. A picture and schematic of the new RHRS detector stack is shown in figure 3-2. Particles pass through the detector stack in the direction shown by the arrow in the figure. Each spectrometer contains two scintillator detectors: the S0 scintillator and the S2m scintillator. The S0 scintillator consists of a single paddle with a photo-multiplier tube (PMT) located at both the top

and bottom of the detector (the X direction in the spectrometer transport coordinate system). The S2m scintillator consists of 16 paddles with a PMT a located at both the left and the right (the Y direction in the spectrometer transport coordinate system) of each paddle. The signals from these scintillators in coincidence are used to form a fast trigger. There are three chambers for tracking (two vertical drift chambers, collectively called the VDC, and a straw chamber). These tracking detectors are used to reconstruct the physics quantities at the reaction vertex. Lastly, the gas cherenkov detector and a lead-glass calorimeter are used for particle identification.

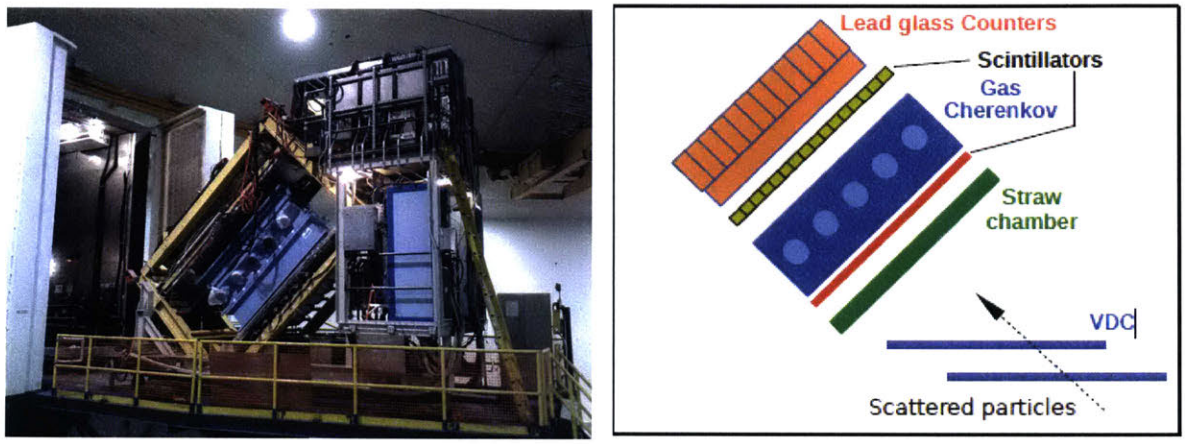

(a) (b)

Figure 3-2: Left: Photo of RHRS detector stack after upgrade (but prior to removal of old S1 detector). Right: Schematic of the RHRS detector stack. The package for the LHRS is similar; however, the calorimeter blocks are arranged differently.

Target System for the *GMp* Experiment

During the experiment, multiple targets were placed on a target ladder inside a vacuum scattering chamber. The ladder was remotely controlled from the Hall A counting house, which allowed for a given target to be placed in the beam path. A picture of a portion of the target ladder during the Fall 2016 run period is shown in figure 3-3. This figure shows Loop 1 (a 4 cm long cryotarget cell), Loops 2 and 3 (both 15 cm long cryotarget cells), the 4 cm long aluminum dummy target, and the multi-foil carbon target.

During the fall of 2016, loop 2 was filled with liquid hydrogen (LH_2) for the production running. It operated at a temperature of 19 K, a pressure of 25 psi, and a density of 0.0732 g/ml. A 15 cm long aluminum dummy target (not shown in figure 3-3) was used to perform background subtractions. The other targets, including the single-foil carbon target, the multi-foil carbon target, and the carbon-hole target, were used to perform various calibrations and stability tests.

Figure 3-3: Picture of a portion of the Hall A target cryotarget system used during the Fall 2016 *GMp* experiment.

3.2 Cross-Section Extraction

Prior to extracting absolute cross-sections, several types of calibrations need to be performed for an inclusive scattering experiment like *GMp*. The first kind are calibrations related to identifying the type of particle. These calibrations include converting the raw ADC signals of the gas cherenkov PMTs into the number of detected photoelectrons, converting the raw ADC signals of the electromagnetic calorimeter into energy deposition, and converting the raw TDC signals of the scintillators into relative times. These calibrations were performed immediately after data-taking and are described elsewhere [65]. In section 3.3, we will use the calibrated quantities when calculating the various efficiencies.

The next class of calibrations are related to calculating the total luminosity of the electron beam and target. The beam-current monitors (BCMs) have to be calibrated relative to a Parametric Current Transformer called an Unser [64], and the change in the target density with current has to be studied. Special runs were taken during the experiment in order to perform these calibrations, allowing for the calibrations to be performed during the data taking.

Lastly, calibrations need to be performed in order to correctly reconstruct the quantities at the reaction vertex. These calibrations are called the optics calibrations and are discussed in Ref. [6]. The coordinate system for describing aspects of the data such as acceptance and the magnetic transport through the spectrometer is called the transport coordinate system. This coordiante system is discussed in detail in Ref. [64]. In figure 3-4, we show a diagram of the transport coordinate system at the target in the horizontal plane and its relationship to the lab coordinate system.

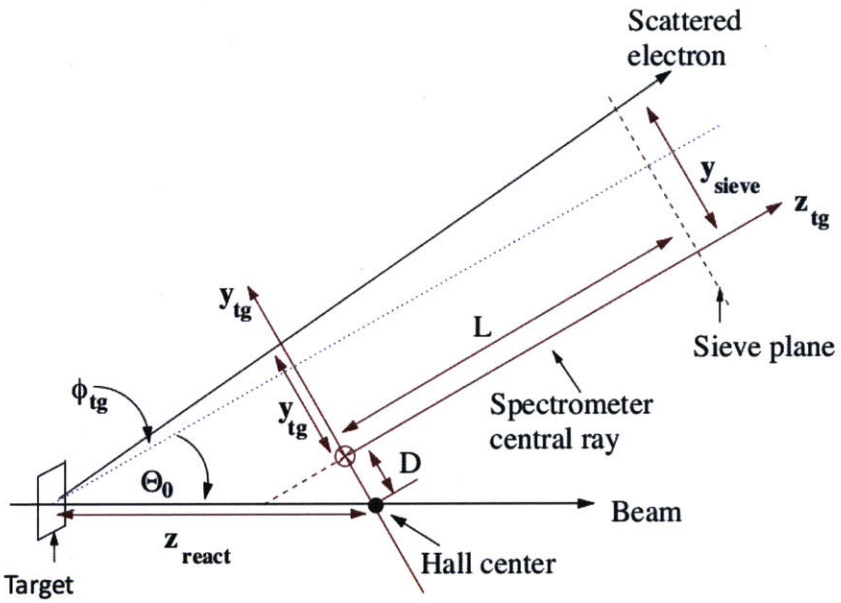

Figure 3-4: Diagram showing a top view of the transport and lab coordinate systems in Hall A.

Once all the calibrations are performed, the cross-section can be calculated from the measured electron yield as

$$\frac{d\sigma}{d\Omega} = \int dE' \frac{N_{det}(E',\theta) - N_{BG}(E',\theta)}{\mathcal{L} \cdot \epsilon_{eff} \cdot LT \cdot \Delta\Omega_{eff}} \cdot RC \tag{3.1}$$

In the above equation, N_{det} is the number of scattered elastic events detected; N_{bg} is the number of events from background processes; $\mathcal{L}$ is the integrated luminosity; ϵ_{eff} is the efficiency correction, composed of the trigger efficiency, the particle identification efficiency, and the tracking efficiency; LT is the live-time; $\Delta\Omega_{eff}$ is the effective solid angle, which characterizes the spectrometer acceptance; and RC is the radiative correction factor. The integral is performed in E' over the elastic peak. The integral should be wide enough to not be sensitive to resolution effects, but needs to be cut off below the pion production threshold.

3.3 Efficiency Studies for the *GMp* Experiment

Total Scintillator Efficiency

The scintillator efficiency, $\epsilon_{S0(S2m)}$, is defined as $\frac{N_{good}}{N_{total}}$, where N_{total} is a sample of clean electron events with S0 (S2m) not in the trigger and N_{good} is the number of these events that contain above-threshold signals within a wide time window in both PMTs of a S0 (S2m) paddle. (Since the discriminated signals are sent to multi-hit TDCs, only the hit closest to the main timing peak is kept for analysis.) The total scintillator efficiency is defined as the result of $\epsilon_{S0} \times \epsilon_{S2m}$.

For the *GMp* experiment, the main trigger (T1) was a coincidence of S0 and S2m [66]. So, the evaluation of the scintillator efficiencies is necessary to determine the main trigger efficiency. In order to accomplish this, two other triggers, T2 and T3, were always enabled. T2 (T3) is a coincidence of S0 (S2m) and the Gas Cherenkov detector, and events of this type can be used to evaluate the efficiency of S2m (S0).

S0 Scintillator Efficiency (ϵ_{S0})

A T3 event sample is used to evaluate the S0 efficiency. Since the S0 detector is smaller than the T3 detectors and located in front of these detectors, the event sample

consists of two categories. In the first category are the events which missed the S0 detector, and they will not be considered for efficiency calculations. In the second category are the events which fell inside the scintillator boundaries and should give signals with large amplitude in both S0 PMTs. The procedure for the S0 scintillator efficiency calculation has the following steps:

- A cut is applied to the particle identification (PID) and tracking detectors to select good electrons. The gas cherenkov vs. calorimeter response is shown in figure 3-5 for one kinematic setting. The tracking and PID cuts applied here are: one track in the VDC, greater than 5 photoelectrons (N_{pe}) in the gas cherenkov counter, and a total momentum-normalized energy deposition ($\frac{E}{p}$) in the calorimeter of at least 0.6 (0.7) for the LHRS (RHRS).

- As mentioned above, only events that should fire the S0 scintillator are included in the efficiency calculation. To select these events, the track is projected to the S0 detector plane as shown in figure 3-6a. Then only events which project inside the boundary of the detector are included for the efficiency study. (Of course, if the track projection is to be used in this manner, it is necessary for the position of the S0 detector relative to the VDC to be well known [67].) For GMp production data, an additional cut is used to select a clean sample of elastic electrons by a cut on the invariant mass as shown in figure 3-6b.

The S0 efficiency was calculated for every production run. The efficiency was found to be stable within every individual kinematic. In addition, an inelastic run which gave reasonably uniform illumination across the focal plane was used to test the efficiency across the entire S0 detector (i.e. in different bins of the track X and Y projection). As shown in figures 3-7 and 3-8, the efficiency is stable across the entire S0 detector. So, a single efficiency was extracted for each kinematic; these efficiencies are shown in table 3.1.

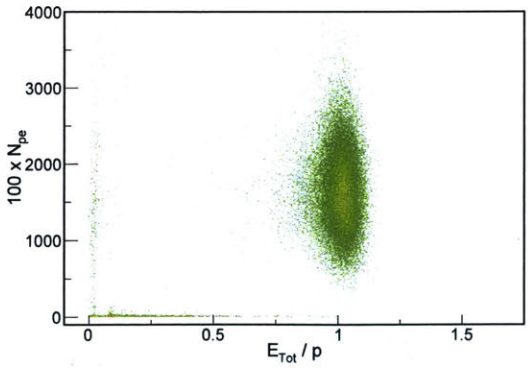

Figure 3-5: Number of photoelectrons produced in the gas cherenkov vs. total momentum-normalized energy deposited in the calorimeter for GMp kinematic k3-6. Good electrons are selected by the cut described in the text.

S2m Scintillator Efficiency (ϵ_{S2m})

A T2 event sample is used to evaluate the S2m efficiency. The S2m scintillator is located behind the S0 and the gas cherenkov detectors, but in front of the lead-glass calorimeter. Therefore, for events that have a T2 trigger (S0 and gas cherenkov) and large energy deposited in the calorimeter, S2m is expected to fire as well. The procedure to calculate the S2m efficiency is as follows:

- The same tracking and PID cuts as described for the S0 efficiency are used to select a clean sample of electrons.
- Only events where the track projects inside the S2m detector are used for the efficiency calculation, as shown in figure 3-9a. For GMp production data, an additional cut is used to select a clean sample of elastic electrons by a cut on the invariant mass as shown in figure 3-9b.

The S2m efficiency was calculated for every production run. The efficiency was found to be stable within every individual kinematic. In addition, an inelastic run which gave reasonably uniform illumination across the focal plane was used to test the efficiency for every S2m paddle. Since the location of the S2m detector is well known, the paddle that should fire for a given event is also known (based on the track projection). Therefore the efficiency of every individual paddle can be calculated.

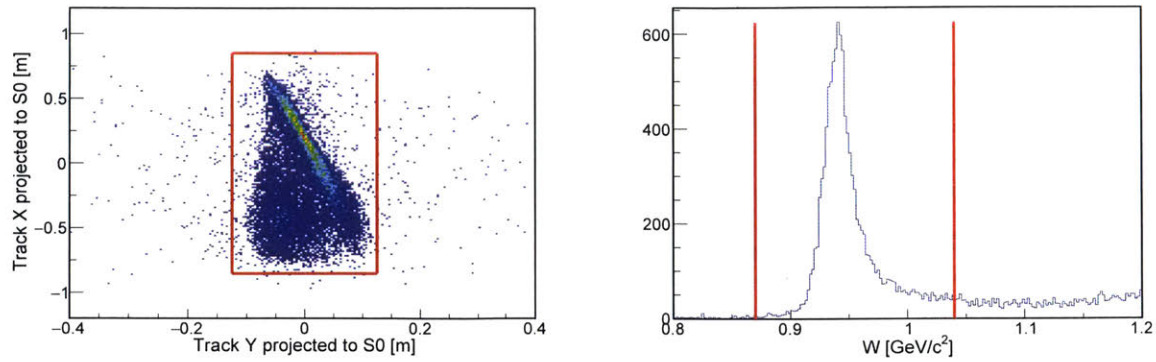

(a) (b)

Figure 3-6: (a) Good electron projection to the S0 scintillator for kinematic k3-9. The red lines indicate the S0 detector edges. (b) Additional cut on the invariant mass (W) used to select a clean elastic electron sample ($0.87\frac{GeV}{c^2} < W < 1.04\frac{GeV}{c^2}$ for kinematic k3-9).

The efficiency as a function of paddle number is shown in figure 3-10, after removing events with large multiple scattering between the VDC detector and S2m detector. Since the calculated efficiency is stable for all the paddles (except at the edge of the acceptance), a single efficiency was extracted for each kinematic. These efficiencies are shown in table 3.1.

Trigger Efficiency

The main trigger for the GMp experiment, T1, consists of a coincidence between the two scintillator detectors (S0 and S2m). There are two procedures that can be used to calculate the trigger efficiency. In the first procedure, we can use a sample of electron events that fired either trigger T2 or T3 or both (call this sample N_T). Then, for this event sample, we can determine the number of events where trigger T1 is present (N_{T1}). If all pre-scale factors are set equal to one (as they were for GMp production data), the trigger efficiency is equal to $\frac{N_{T1}}{N_T}$. In the second procedure, one can calculate the trigger efficiency from the individual scintillator efficiencies as the product of the S0 efficiency and S2m efficiency. The trigger efficiency determined from both methods was found to be consistent. In table 3.2, the trigger efficiency for all kinematics is shown using the second method.

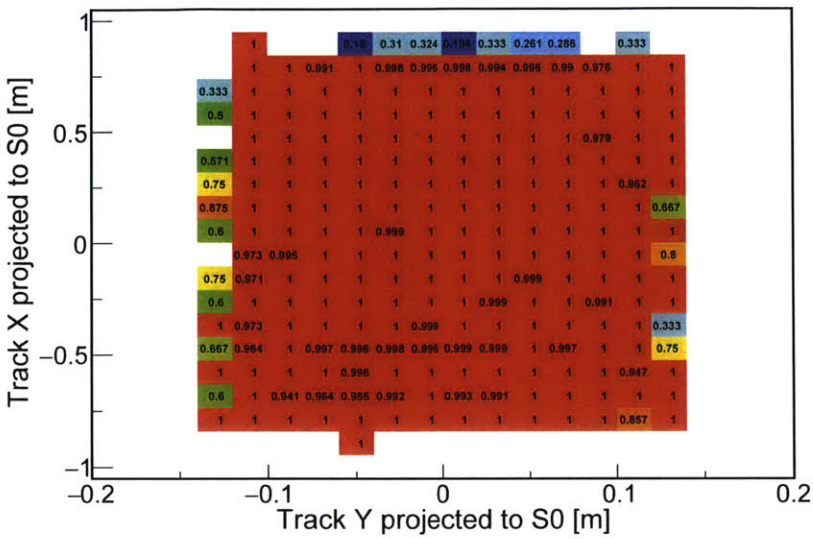

Figure 3-7: Two-Dimensional S0 efficiency in bins of track projection. A LHRS inelastic run is used here. The efficiency is stable across the entire detector area.

Uncertainties and Cross-Talk Check

In addition to the standard binomial uncertainty, several other factors affect the determination of the efficiency. For the individual scintillator efficiencies, the timing windows used and the knowledge of the exact positions of the scintillators relative to the VDC can have an effect. The effect on the efficiencies of changing the timing window around the main TDC peak from a very wide cut to a cut with a full-width of 200 ns is at most 5×10^{-4}. The effect on the efficiencies of changing the assumed distance of the scintillators from the VDC by 0.5 cm is about 1×10^{-3} for S0 and 5×10^{-4} for S2m. The individual scintillator efficiencies, along with the accompanying uncertainties, are shown in table 3.1. For the trigger T1 efficiency, in addition to the propagation of the individual scintillator uncertainties, we looked at the difference between extracting the efficiency using the two methods mentioned above. We place an uncertainty on the T1 efficiency of 1×10^{-4} on this. The trigger 1 efficiencies, along with the accompanying uncertainties, are shown in table 3.2.

Lastly, we looked into the question of cross-talk artificially enhancing the trigger T1 efficiency. Since all the triggers are formed by coincidences in a Majority Logic Unit (MLU), an independent method was developed to make sure that no artificial T1

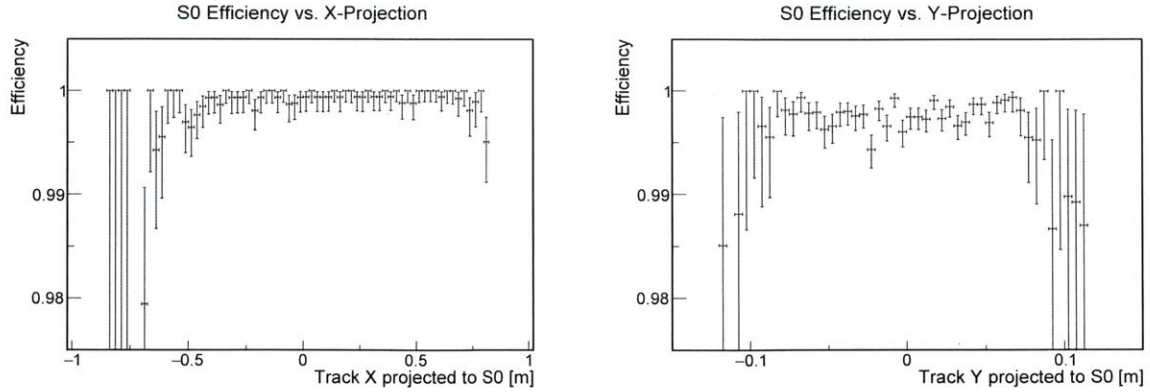

(a) (b)

Figure 3-8: One-Dimensional projections of the plot in figure 3-7. Left: Efficiency vs. Track X projection. Right: Efficiency vs. Track Y projection.

signals were generated in the MLU. For every T1 event, we determined whether both S0 and S2m had signals in the TDCs for their individual channels. For all kinematics, we found that fewer than 1 in 100,000 T1 events lacked an S0 or S2m signal. So, we conclude that there was no issue with trigger cross-talk during data taking. The fact that the trigger efficiency is the same using the two methods described above demonstrates this as well.

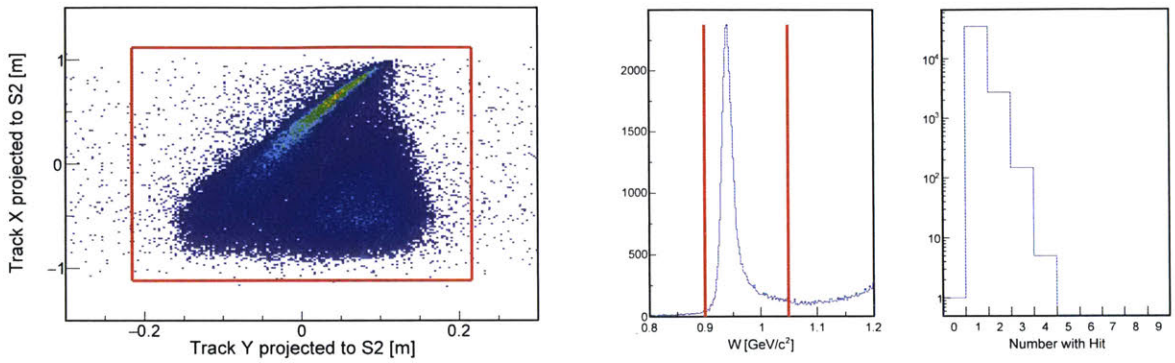

(a) (b)

Figure 3-9: (a) Good electron projection to the S2m scintillator for kinematic k3-7. The red lines indicate the S2m detector edges. (b) Left: Additional cut used to select a clean electron sample of interest in the elastic peak for k3-7. Right: Number of S2m paddles with left + right coincidence after applying all cuts. The small number of events where more than 2 paddles fire are due to the wide time window used to determine whether a PMT hit occurred.

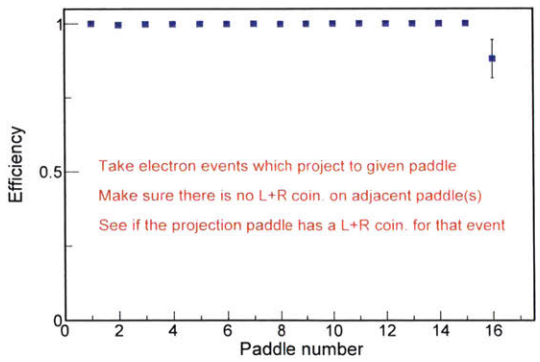

Figure 3-10: S2m Efficiency vs. paddle number. An inelastic run is used here. As stated on the plot, a procedure was developed to limit the effects of multiple scattering by requiring no signal on adjacent paddles.

Kinematic	Spectrometer	ϵ_{S0}	ϵ_{S2m}
k1-0.4	LHRS	$0.999\ (1.1 \times 10^{-3})$	$0.999\ (7 \times 10^{-4})$
k1-1.5	LHRS	$0.999\ (1.1 \times 10^{-3})$	$0.999\ (7 \times 10^{-4})$
k1-1.8	RHRS	$0.995\ (1.1 \times 10^{-3})$	$0.999\ (7 \times 10^{-4})$
k1-1.9	RHRS	$0.998\ (1.1 \times 10^{-3})$	$0.999\ (7 \times 10^{-4})$
k3-4	LHRS	$0.998\ (1.1 \times 10^{-3})$	$0.999\ (7 \times 10^{-4})$
k3-6	LHRS	$0.999\ (1.1 \times 10^{-3})$	$0.999\ (7 \times 10^{-4})$
k3-7	LHRS	$0.999\ (1.1 \times 10^{-3})$	$0.999\ (7 \times 10^{-4})$
k3-8	LHRS	$0.999\ (1.1 \times 10^{-3})$	$1.000\ (7 \times 10^{-4})$
k4-9	LHRS	$0.998\ (1.1 \times 10^{-3})$	$0.999\ (7 \times 10^{-4})$
k4-10	LHRS	$0.998\ (1.1 \times 10^{-3})$	$0.999\ (7 \times 10^{-4})$
k4-11	LHRS	$0.999\ (1.1 \times 10^{-3})$	$0.999\ (7 \times 10^{-4})$
k3-9	RHRS	$0.996\ (1.3 \times 10^{-3})$	$0.999\ (7 \times 10^{-4})$
k4-12	RHRS	$0.995\ (1.3 \times 10^{-3})$	$0.999\ (7 \times 10^{-4})$

Table 3.1: S0 and S2m efficiencies for all Fall 2016 GMp kinematics. The relative (i.e. fractional) total uncertainty for each efficiency is shown in parenthesis. The total uncertainty for each efficiency is the binomial uncertainty combined with the uncertainties discussed in the text. Each kinematic is named based on the beam energy (pass number) and the central Q^2 value.

Kinematic	Spectrometer	ϵ_{T1}
k1-0.4	LHRS	$0.998\ (1.3 \times 10^{-3})$
k1-1.5	LHRS	$0.998\ (1.3 \times 10^{-3})$
k1-1.8	RHRS	$0.994\ (1.3 \times 10^{-3})$
k1-1.9	RHRS	$0.997\ (1.3 \times 10^{-3})$
k3-4	LHRS	$0.997\ (1.3 \times 10^{-3})$
k3-6	LHRS	$0.998\ (1.3 \times 10^{-3})$
k3-7	LHRS	$0.998\ (1.3 \times 10^{-3})$
k3-8	LHRS	$0.999\ (1.3 \times 10^{-3})$
k4-9	LHRS	$0.997\ (1.3 \times 10^{-3})$
k4-10	LHRS	$0.997\ (1.3 \times 10^{-3})$
k4-11	LHRS	$0.998\ (1.3 \times 10^{-3})$
k3-9	RHRS	$0.995\ (1.5 \times 10^{-3})$
k4-12	RHRS	$0.994\ (1.5 \times 10^{-3})$

Table 3.2: Trigger 1 efficiencies calculated as the product of S0 and S2m efficiencies for all Fall 2016 GMp kinematics. The relative (i.e. fractional) total uncertainty for each efficiency is shown in parenthesis. The total uncertainty for each efficiency is the binomial uncertainty combined with the uncertainties discussed in the text. There are two methods that can be used to extract the trigger efficiency; as discussed in the text, we apply an uncertainty to account for this.

Particle Identification Efficiency

In many experiments, including the GMp experiment, the main trigger collects particles other than those needed for the measurement. In experiments where electrons are desired, the background particles are primarily pions and cosmic rays. To remove these background events and preserve the electrons, software cuts are applied based on the number of photoelectrons in the gas cherenkov detector and the momentum-normalized energy deposited in the calorimeter. A correction has to be made based on the number of electrons which fail the final particle identification (PID) cuts and the number of pions which pass those same cuts. (The success of all the final cuts, including tracking and timing cuts, in removing cosmic events is discussed in section 3.3).

The question then is what are the best quantities to extract to make this correction. We want to determine the total number of electrons, N_e^t; but what we measure before the PID cuts is $N^t = N_e^t + N_\pi^t$, where N^t is the total number of measured events and $N_{e(\pi)}^t$ is the total number of electrons (pions); after the PID cuts, we have $N^f = N_e^f + N_\pi^f$, where N^f is the total number of final events and $N_{e(\pi)}^f$ is the final number of electrons (pions). We can determine the electron cut efficiency for the gas cherenkov (calorimeter) by selecting a sample of clean electrons in the calorimeter (gas cherenkov), and then looking at the response of the gas cherenkov (calorimeter) for that sample. We can determine the pion rejection efficiencies (i.e. the fraction that fail to pass all PID cuts) in a similar manner. Once we know the total electron efficiency (ϵ_e) and the total pion rejection efficiency (ϵ_π)[1], we can relate the yields before and after the PID cuts as $N_e^f = \epsilon_e \times N_e^t$ and $N_\pi^f = (1 - \epsilon_\pi) \times N_\pi^t$. Since we know $N^t, N^f, \epsilon_e \,\&\, \epsilon_\pi$, we can solve for $N_e^t, N_\pi^t, N_e^f \,\&\, N_\pi^f$.

However, if we write $N^f = N_e^f + N_\pi^f$ as

$$N^f = N_e^f \cdot (1 + \frac{N_\pi^f}{N_e^f}), \tag{3.2}$$

[1]Some prefer to define a pion suppression faction instead of a pion rejection efficiency; both quantities contain the same information. *De gustibus non est disputandum.*

and the final pion-to-electron ratio, $\frac{N_\pi^f}{N_e^f}$, as $\left(\frac{\pi}{e}\right)_f$, we can solve for N_e^t as

$$N_e^t = \frac{N_e^f}{\epsilon_e \cdot (1 + \left(\frac{\pi}{e}\right)_f)}. \tag{3.3}$$

So, for each run we need to determine ϵ_e and $\left(\frac{\pi}{e}\right)_f$ in order to correct for the PID cut efficiency.

Event Categorization

In addition to the background cosmic and pion events, we found a set of events which gave a large signal in the gas cherenkov detector and no signal in the calorimeter. These events were rare compared to good events during runs with high rates, but became quite prominent at high-pass GMp production settings. The events are easily removed with a standard calorimeter cut; but since they have a large signal in the gas cherenkov, these events will artificially reduce the calorimeter efficiency that we extract using the standard method. So, prior to performing PID cut efficiency studies, we tried to better understand these events and suppress them without using the PID detectors.

In figure 3-11, we plot the number of photoelectrons in the gas cherenkov detector vs. the momentum-normalized total energy deposited in the calorimeter for GMp kinematic k3-7 on the LHRS. The plot is for all events with the standard trigger and a single cluster present in all 4 VDC planes. As shown on the plot, we divide the events into four categories: events with a large response in both detectors (red box), events with a large response in the cherenkov but no response in the calorimeter (green box), events with no response in the either detector (black box), and events with no response in the cherenkov but a small response in the calorimeter (blue box).

For these four categories of events, we then show in figure 3-12 the beta spectrum as determined from the track and scintillator timing information. As can be seen in the plot, the red and green events have similar spectra with the events peaked at beta equal to one. This, combined with the large cherenkov response, seems to indicate that the green events are actually electrons; the question is whether they are missing

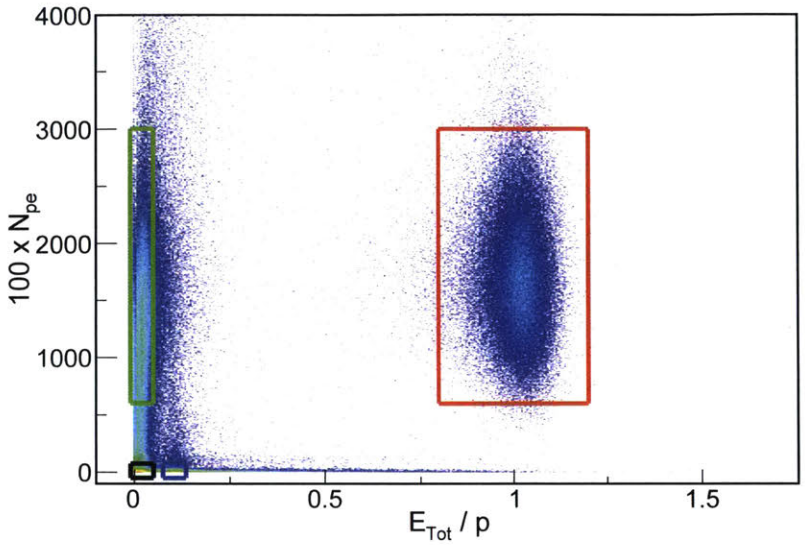

Figure 3-11: Number of photoelectrons in the gas cherenkov vs. momentum-normlalized energy deposition in the calorimeter for GMp kinematic k3-7. The meaning of the various rectangles are discussed in the text.

the calorimeter or are low-energy events produced somewhere upstream of the VDC. In the same plot, we see that the black and blue events have peaks at both positive and negative beta. The events at negative beta are cosmic events, and we cut them out by requiring $\beta > 0.2$. The remaining blue events are most likely negative pions originating from the target, while it is unclear what constitutes the black events.

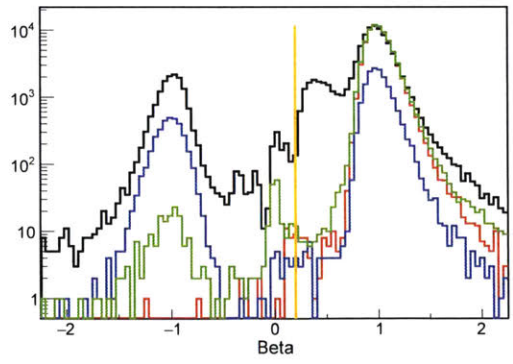

Figure 3-12: Beta (β) spectra calculated from the scintillator times and VDC track for the four types of events shown in figure 3-11. We apply a cut of $\beta > 0.2$ for all additional results shown in this subsection.

To test some of the conjectures in the above paragraph, we consider several ad-

ditional spectra. First, in figure 3-13 we plot the reconstructed target quantities for the four types of events. As can be seen, the red events fall within the spectrometer acceptance, as expected for good electrons. A large fraction of the blue events originate from the aluminium windows of the 15 cm long hydrogen target, suggesting that these events are indeed pions. The green and the black events do not seem to track back solely to the target, which may indicate that these events do not pass through the entire spectrometer and thus are not being correctly reconstructed. These events could conceivably originate from the beam line and in-scatter into the spectrometer detector hut. However, from beam halo studies, we know that the beam is not scrapping the beam line; so the events more likely either originate from some aperture inside the spectrometer upstream of the detector hut (or, as mentioned above, are missing the calorimeter).

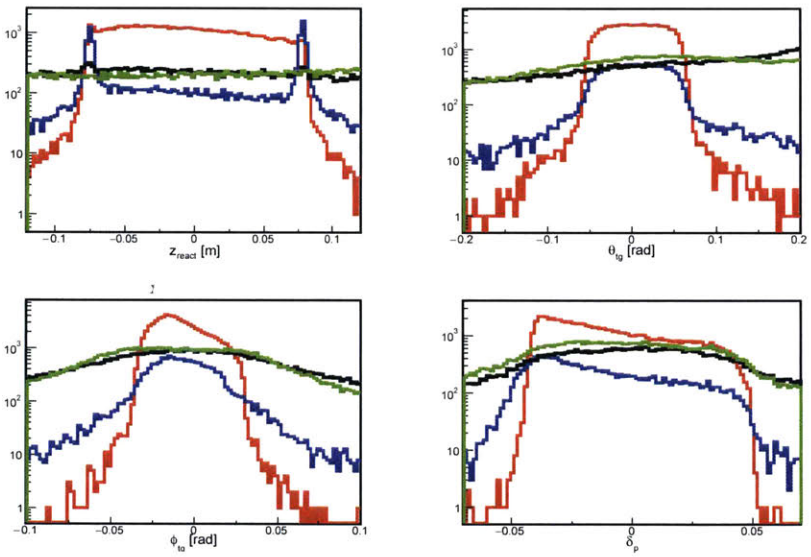

Figure 3-13: Reconstructed quantities in the spectrometer coordinate system for the four types of events shown in figure 3-11. Clockwise from the top left: reconstructed vertex (z_{react}), reconstructed out-of-plane angle (θ_{tg}), reconstructed fraction momentum deviation (δ_p), and reconstructed in-plane angle (ϕ_{tg}).

We can check if those events with high cherenkov response and no signal in the calorimeter are simply missing the detector. We do this by projecting the VDC track to the known position of the calorimeter. In figure 3-14, we show the events projected to the first layer of the calorimeter. The physical size of the calorimeter is shown by

the purple box. As can be seen, the bulk of the green events fall within the calorimeter detector. So, in addition to the strange target reconstruction, there is no reason to think the green events are actually good electrons that track outside the calorimeter.

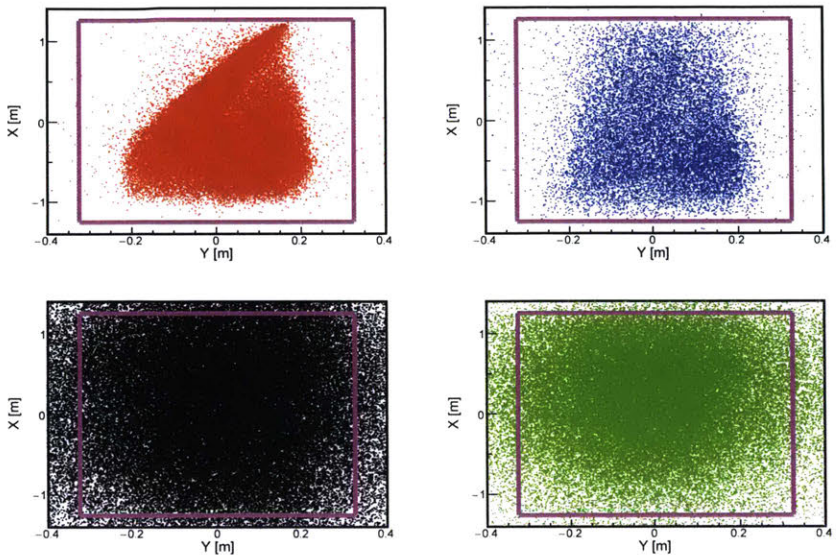

Figure 3-14: Track from VDC projected to calorimeter layer 1 for the four types of events shown in figure 3-11. The physical size of the calorimeter is shown by the purple box.

Next, we attempted to determine the origin of these background events. In figure 3-15, we plot the events at the VDC U1 plane. The green events consist of two bands close to the edge of the VDC in the non-dispersive direction. Although all the events are within the VDC active area, their proximity to the edge may indicate that these events are produced by an aperture somewhere near the VDC. We checked this by projecting the events forward to the second VDC plane, as well as backwards to the vacuum exit window, the end-of-bellows aperture, and the Q3 exit. Although for many of these projections some of the green events were outside the aperture, many events were situated inside the aperture. So while it was not entirely clear from where the green events originate, it is possible that the events are low-energy electrons that are produced when a high-energy particle hits an aperture near the VDC.

While it seems that no cut besides the calorimeter energy deposition can cleanly remove the background events, we can apply several cuts to significantly reduce their

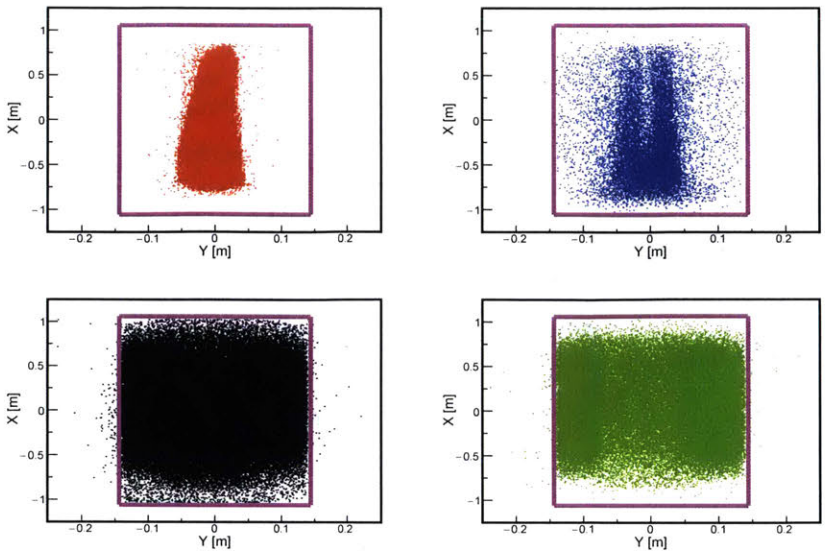

Figure 3-15: Track at VDC U1 plane for the four types of events shown in figure 3-11. The physical size of the VDC is shown by the purple box.

presence. In figure 3-16, we show the deviation of track projection from the center of the struck S2m paddle; requiring this deviation to be small will reduce the background events relative to the electron and pion events under study. Likewise, in figure 3-17, we show the deviation of the track projection from the energy-weighted hit position in the calorimeter. In figure 3-18, we show the reconstructed invariant mass. As can be seen, only the good electron sample shows an elastic peak. Since the GMp experiment is interested in elastic scattering, it is appropriate to apply a cut around the elastic peak when studying the PID efficiency.

Extraction of ϵ_e and $\left(\frac{\pi}{e}\right)_f$

For the calculation of the electron efficiency and pion rejection efficiency, we begin by applying the following cuts:

1. Trigger 1 is present for the event.

2. Only 1 cluster is present in all 4 VDC planes.

3. The track beta is between 0.3 and 2.0. See figure 3-12.

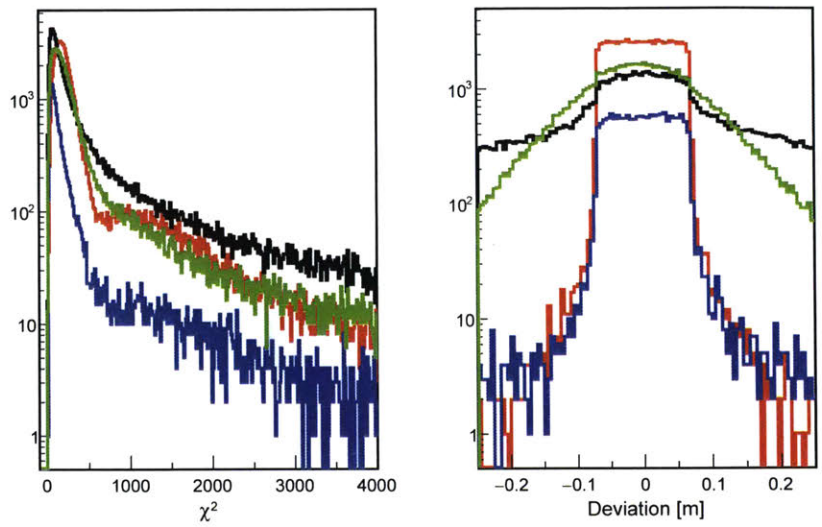

Figure 3-16: Left: VDC track quality as determined from a fit of the clusters in all the VDC planes. We don't apply any cuts on this variable for the PID efficiency study. Right: VDC track projection deviation (in the dispersive plane) from hit S2m paddle center for the four types of events shown in figure 3-11. The individual S2m paddles have a full-width of 14 cm. The 'good' electron sample (red) distribution is flat from -0.7 cm to +0.7 cm, and then falls sharply. The pion distribution (blue) is also flat from -0.7 cm to +0.7 cm, but it has a larger fraction of events in the tails. The green events, however, show much less structure, which means that they experience a large amount of multiple scattering between the VDC and S2m. The is additional evidence that these events are low-energy particles.

4. The following 'sanity' cuts are applied on the acceptance (figure 3-13):

   - The reconstructed out-of-plane angle is between -100 mrad and +100 mrad.
   - The reconstructed in-plane angle is between -50 mrad and +50 mrad.
   - The reconstructed momentum deviation is between -5.5% and +5.5%.
   - The reconstructed reaction vertex is between -10 cm and +10 cm (-6.5 cm and +6.5 cm when calculating the electron efficiency). The hydrogen cryo-target is 15 cm long, and while many of the pion events originate from the cell windows, very few of the electrons do. So when calculating the electron efficiency, we remove the windows with a vertex cut to obtain a cleaner electron sample.

5. The absolute value of the S2m track deviation is less than 0.09 m. See figure

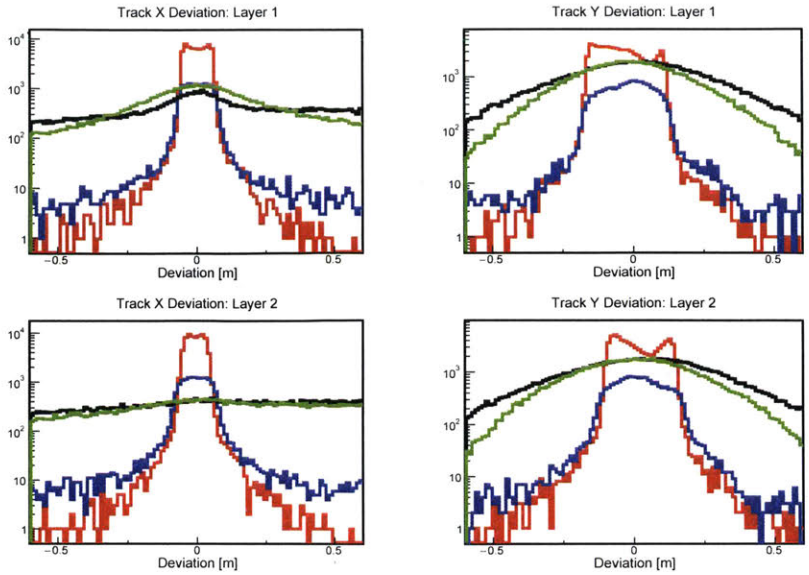

Figure 3-17: The VDC track projection deviation from the energy-weighted hit position in the calorimeter for both calorimeter layers and directions. The distributions are shown for the four types of events in figure 3-11. Since the green and black events have essentially no response in the calorimeter, the energy-weighted position for these events is just pedestal noise.

3-16.

6. The reconstructed invariant mass is between 0.8 GeV/c^2 and 1.1 GeV/c^2. See figure 3-18.

We should note that some of these cuts (e.g. the S2m track deviation cut) may not necessarily be used during the final cross-section extraction. They are used here in order to select the cleanest possible sample of electrons (and pions). Since the applied cuts remove electrons and pions with different probabilities, the initial pion-to-electron ratio that we extract here depends somewhat on the cuts used. However, as we show, the final pion-to-electron ratio is very small for all kinematics; and the effect of small changes to the initial sample on the final contamination are negligible. (In addition, since many of the pion events originate from the target windows, there is probably some vertex dependence to the pion contamination which we ignore.)

For each kinematic, we first extract the software-cut-dependent electron efficiency and pion rejection efficiency for the gas cherenkov detector. We do this by selecting a

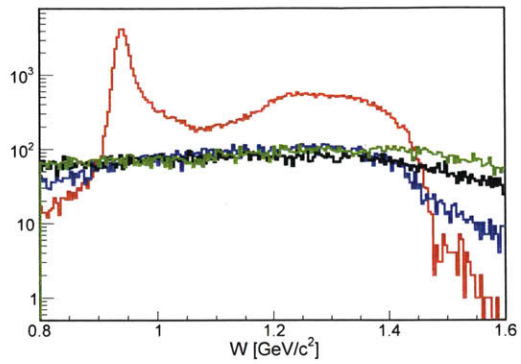

Figure 3-18: Reconstructed invariant mass (W) assuming electron scattering for the four types of events shown in figure 3-11. Only the 'good' electron (red) events display the elastic peak, as expected.

clean sample of both electrons and pions based on the response in the calorimeter. In figure 3-19, we show the momentum-normalized energy deposition in each calorimeter layer for GMp kinematic k3-7. The selected electrons are the events contained within the red lines, while the selected pions are those within the blue lines. In the bottom left corner of the plot, one can see a small number of events which correspond to the 'low-energy' background discussed in the previous sub-section.

For the selected electron and pion samples, we plot the number of photoelectrons detected in the gas cherenkov in figure 3-20a. Then for each possible software cut on the number of collected photoelectrons, we calculate the electron efficiency and pion rejection efficiency (figure 3-20b). The electron efficiency is simply the fraction of the events above a given cut; the pion rejection efficiency is the fraction of events below the cut.

We repeat the process to calculate the electron efficiency and pion rejection efficiency for the calorimeter. We select a sample of electrons and pions in the gas cherenkov (figure 3-21), and consider their response in the calorimeter (figure 3-22a) for GMp kinematic k3-7. However, as can be seen, both the electron and pion samples are contaminated by the 'low-energy' background discussed in the previous subsection. To remove this background, we first isolate these events and then study the calorimeter response. The way that we isolate the 'low-energy' background events is by requiring both a large cherenkov response and a large S2m track deviation. That

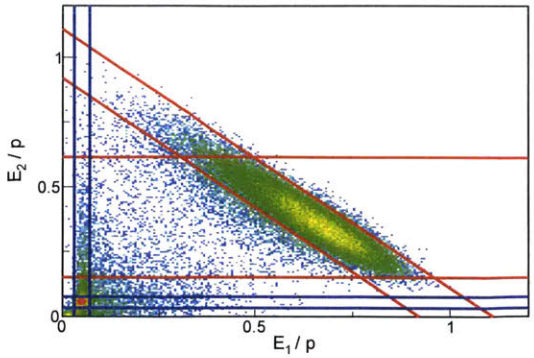

Figure 3-19: Electron and pion sample selection in the calorimeter for studying the gas cherenkov efficiency. The horizontal (vertical) axis in the momentum-normalized energy deposited in calorimeter layer 1 (2). The events contained within the red lines are the electrons; those contained within the blue lines are the pions. The events displayed on the plot pass the cuts listed at the beginning of this subsection. In addition, when selecting the event samples to study the gas cherenkov efficiency, we require the energy-weighted hit position in the calorimeter to be close to the track projection (see figure 3-17). The data shown here are for GMp kinematic k3-7.

is, we are essentially trying to isolate the green events in figure 3-16, for example. After selecting these events, we then plot the calorimeter momentum-normalized energy deposition (E/p) for GMp kinematic k3-7 in figure 3-22b. As can be seen, nearly all the events have E/p < 0.3. Based on this information, as well as the electron and pion peaks at lower E/p in figure 3-22a, we choose to use only events above a certain minimum E/p when calculating the calorimeter efficiencies. When calculating the electron efficiency, we require the electron event sample to have E/p > 0.3; when calculating the pion rejection efficiency, we require the pion event sample to have E/p > 0.05.

Since there are two layers in the calorimeter, we apply a software cut on both the total energy deposited in the calorimeter and on the energy deposited in layer 1 of the calorimeter. (The motivation for requiring a minimum energy to be deposited in layer 1 of the calorimeter comes from the vertical tail that can be seen in figure 3-19). In figures 3-23a and 3-23b we show grids for the calorimeter electron efficiency and pion rejection efficiency, respectively.

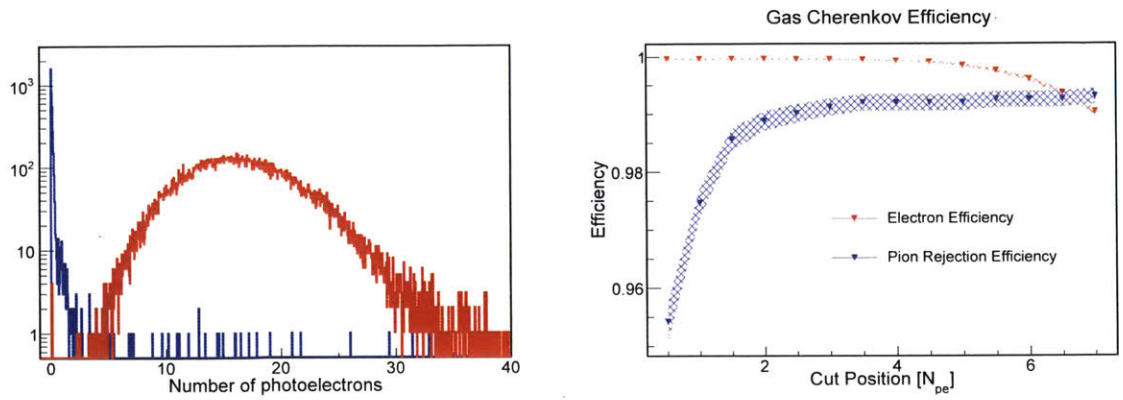

(a) (b)

Figure 3-20: (a) Number of photoelectrons collected in the gas cherenkov detector for the electron (red) and pion (blue) samples selected in figure 3-19. (b) Electron and pion gas cherenkov cut efficiencies for the samples selected in figure 3-19. The error bands shown are calculated assuming standard binomial uncertainties.

Similarly to what was done for the S0 and S2m scintillators, we checked for any dependence to the extracted efficiencies across the gas cherenkov and calorimeter detector planes. We did this by projecting the track to the given detector under study and looking for any dependence to the efficiency. For both the gas cherenkov and the calorimeter, the electron detection efficiency and pion rejection efficiency showed no position dependence.

The total electron efficiency is calculated from the individual cherenkov and calorimeter electron efficiencies as $\epsilon_e = \epsilon_{cer,e} \times \epsilon_{cal,e}$. The total pion rejection efficiency is calculated from the individual cherenkov and calorimeter pion rejection efficiencies as $\epsilon_\pi = 1 - (1 - \epsilon_{cer,\pi}) \times (1 - \epsilon_{cal,\pi})$. In table 3.3, we show the final total electron detection efficiencies, the total pion rejection efficiencies, the initial pion-to-electron ratios, and the final pion-to-electron ratios for the following set of PID cuts:

$$N_{pe} > 4, \left(\frac{E}{P}\right)_{Total} > 0.7, \left(\frac{E}{P}\right)_{Layer1} > 0.08\,.$$

We calculate a standard binomial statistical uncertainty for each measured efficiency. In addition, we consider two additional potential sources of error. First, when selecting samples of either electrons or pions in a given detector, we assume that those

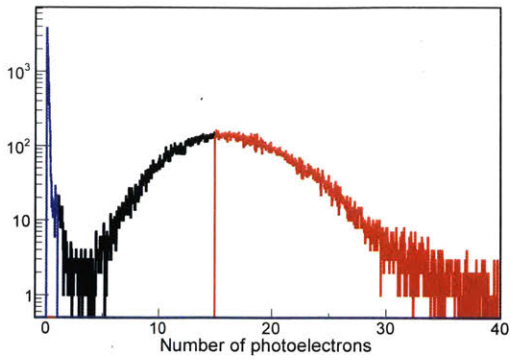

Figure 3-21: Electron and pion sample selection in the gas cherenkov for studying the calorimeter efficiency. Events with greater than 15 photoelectrons constitute the electron sample; those with less than 1 photoelectron constitute the pion sample. The events displayed on the plot pass the cuts listed at the beginning of this subsection. The data shown here are for GMp kinematic k3-7.

samples are completely 'clean' (i.e. that they only contain the particle under study). This is of course not necessarily true, and we can study the effect of contamination in the samples by varying the sample-selection cuts. Second, we make the (quite justified) assumption that all the good electron events have $E/p > 0.3$, while all the 'low-energy' background events have $E/p < 0.3$. We study the effect of changing this E/p threshold by a reasonable amount on the calorimeter efficiencies, and apply an uncertainty on this. The relative total uncertainties on the electron efficiencies and pion rejection efficiencies are shown in table 3.4.

As can be seen in table 3.3, the final pion-to-electron ratios are very small. These ratios are determined by the cut efficiencies and by the initial pion-to-electron ratio. The relative uncertainty on the final pion-to-electron ratio is also shown in table 3.4 for each kinematic.

Finally, we consider an alternative method for determining the PID cut efficiencies and rates of pion contamination. If one could determine functional forms for the electron, pion, and 'low-energy' background distributions in the gas cherenkov and calorimeter, all the efficiencies and pion-to-electron ratios can be easily extracted. The way to determine these spectra for a given detector would be to once again select a sample of the particle under study in the other detector. Then the resulting

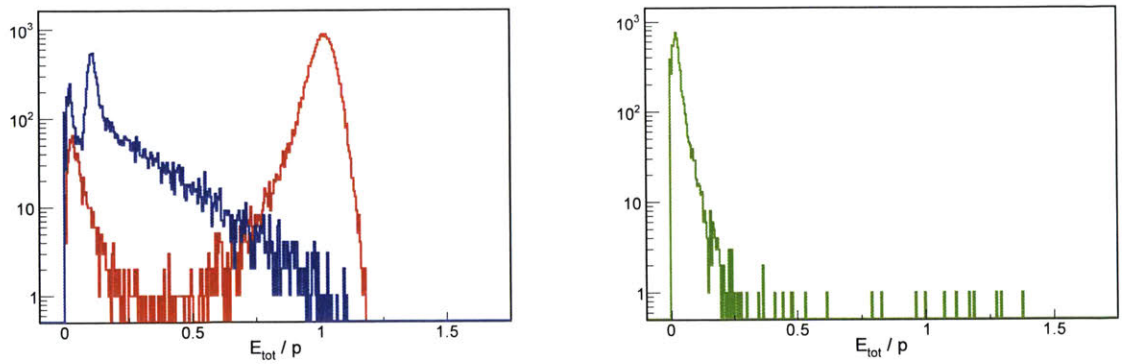

Figure 3-22: (a) Total momentum-normalized energy deposited in the calorimeter for the electron (red) and pion (blue) samples selected in figure 3-21. As can be seen, there are clearly some events in both samples that correspond to the 'low-energy' background discussed in the last subsection. Since these events should not be included when calculating the calorimeter efficiencies, we only consider events above a certain threshold. More details are given in the text. (b) Total momentum-normalized energy deposited in the calorimeter for 'low-energy' background events selected by requiring a large cherenkov response and a significant amount of multiple scattering between the VDC and S2m. This plot shows us that very few of the 'low-energy' events have E/p greater than 0.3. As can be seen in (a), good electron events have E/p peaked at 1 with a small tail going to lower E/p. This means that we can remove the 'low-energy' contamination by requiring E/p >0.3.

spectrum can be fit with an appropriate functional form. For example, one would fit the electron and pion spectra in figure 3-20a and then extract the efficiency for any cut. To determine the pion-to-electron ratios, one would simply scale the amplitude of the each spectrum to match the true distribution.

We attempted this fitting method, but we ran into several difficulties. We were able to fit the cherenkov spectra quite well, and the uncertainties on the extracted parameters gave uncertainties comparable to what we achieved with our cut method. For the calorimeter, however, we had to fit the good electron events and the 'low-energy' background simultaneously (see figure 3-22a). This led to a dependence of the extracted electron efficiency on the functional form that we chose for both the electrons and the background. So we decided that the preferable method is the one discussed in detail in this section.

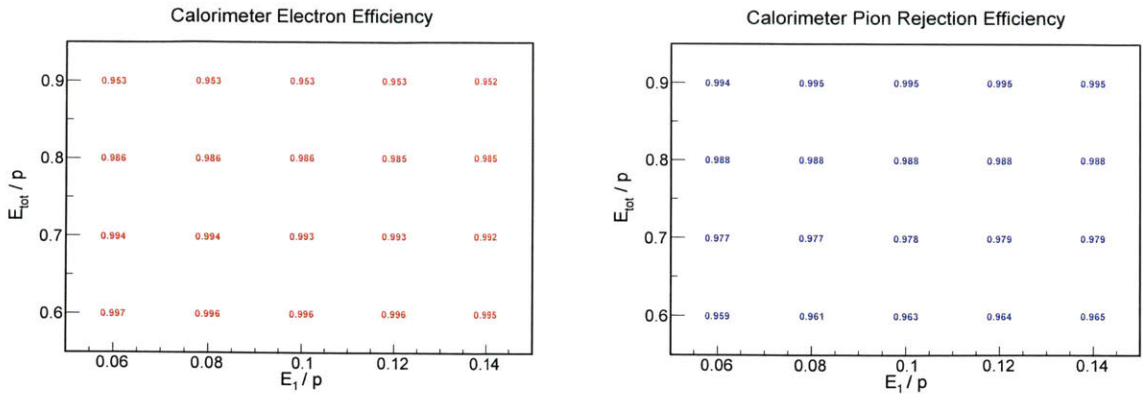

(a) (b)

Figure 3-23: (a) Grid showing calorimeter electron detection efficiencies for various cuts on the total energy deposited in the calorimeter and the energy deposited in layer 1. The results are shown for GMp kinematic k3-7. (b) Grid showing calorimeter pion rejection efficiencies for various cuts on the total energy deposited in the calorimeter and the energy deposited in layer 1. The results are shown for GMp kinematic k3-7.

Other Cut Efficiencies

Besides the standard PID cuts discussed in the previous subsection, an analysis may choose to apply other software cuts which require an efficiency correction. (Of course, not all software cuts require an efficiency correction. An applied cut on the reconstructed in-plane and out-of-plane angles at the target, for example, simply defines the solid angle.) For example, in the GMp experiment, it is likely that the final cross-section analysis will use a cut on the time difference between the S0 and S2m scintillators (i.e. a beta cut) to remove any remaining cosmic events. To study the efficiency of any chosen cut on the track beta, we once again begin by selecting a good sample of electron events. That is, we select events with a good trigger, a good track in the VDC, and good responses in both PID detectors. The track beta for events passing this sample-selection cut for GMp kinematic k3-7 is shown in figure 3-24. For a selected software cut on the track beta of greater than 0.2, we show the efficiencies for all Fall 2016 GMp kinematics in table 3.5.

Kinematic	Spectrometer	ϵ_e	ϵ_π	$\left(\frac{\pi}{e}\right)_i$	$\left(\frac{\pi}{e}\right)_f$
k1-0.4	LHRS	0.995	0.977	7.4×10^{-4}	1.7×10^{-5}
k1-1.5	LHRS	0.995	0.999	9.3×10^{-4}	5.7×10^{-6}
k1-1.8	RHRS	0.992	0.999	0.025	2.9×10^{-6}
k1-1.9	RHRS	0.991	0.999	0.020	2.8×10^{-6}
k3-4	LHRS	0.992	0.999	8.7×10^{-3}	2.8×10^{-6}
k3-6	LHRS	0.993	0.999	0.057	2.3×10^{-5}
k3-7	LHRS	0.993	0.999	0.25	4.0×10^{-5}
k3-8	LHRS	0.994	0.999	1.07	1.8×10^{-4}
k4-9	LHRS	0.991	0.999	0.20	7.6×10^{-5}
k4-10	LHRS	0.992	0.999	0.55	2.3×10^{-4}
k4-11	LHRS	0.992	0.999	2.91	6.6×10^{-4}
k3-9	RHRS	0.984	0.999	7.28	4.2×10^{-4}
k4-12	RHRS	0.984	0.999	10.42	8.4×10^{-4}

Table 3.3: Particle identification (PID) cut efficiencies and initial and final pion contamination for all Fall 2016 GMp kinematics. The applied PID cut is discussed in the text. The initial (final) pion-to-electron ratio is defined as the ratio before (after) applying the PID cuts.

Kinematic	Spectrometer	$d\epsilon_e/\epsilon_e$	$d\epsilon_\pi/\epsilon_\pi$	$d\left(\frac{\pi}{e}\right)_f / \left(\frac{\pi}{e}\right)_f$
k1-0.4	LHRS	5.2×10^{-4}	4.5×10^{-2}	3.6×10^{-2}
k1-1.5	LHRS	5.2×10^{-4}	3.2×10^{-3}	1.1×10^{-2}
k1-1.8	RHRS	5.3×10^{-4}	1.7×10^{-3}	8.2×10^{-3}
k1-1.9	RHRS	5.4×10^{-4}	1.2×10^{-3}	1.2×10^{-2}
k3-4	LHRS	9.3×10^{-4}	1.3×10^{-2}	6.3×10^{-2}
k3-6	LHRS	7.4×10^{-4}	5.2×10^{-3}	2.1×10^{-2}
k3-7	LHRS	7.6×10^{-4}	2.1×10^{-3}	1.1×10^{-2}
k3-8	LHRS	8.4×10^{-4}	1.2×10^{-3}	8.7×10^{-3}
k4-9	LHRS	8.8×10^{-4}	3.3×10^{-3}	1.3×10^{-2}
k4-10	LHRS	8.1×10^{-4}	2.2×10^{-3}	8.4×10^{-3}
k4-11	LHRS	1.1×10^{-3}	1.4×10^{-3}	8.8×10^{-3}
k3-9	RHRS	2.0×10^{-3}	7.8×10^{-4}	1.4×10^{-2}
k4-12	RHRS	1.5×10^{-3}	5.3×10^{-4}	9.9×10^{-3}

Table 3.4: Relative total uncertainties on extracted electron efficiency, pion rejection efficiency, and final pion-to-electron ratio for all Fall 2016 GMp kinematics. As mentioned in the text, uncertainties are applied on the extracted electron and pion efficiencies due to the purity of the sample selection and the E/p threshold used to separate the good events from the 'low-energy' background. We apply an uncertainty of 5×10^{-4} (1×10^{-4}) on the electron (pion) efficiency due to the sample selection. We apply an uncertainty of 1×10^{-4} on both the electron and pion efficiency due to the E/p threshold.

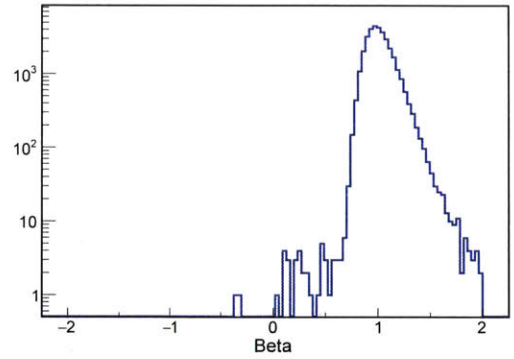

Figure 3-24: Track beta for a sample of good electrons selected as discussed in the text. The efficiency of a cut of $\beta > 0.2$ is shown in table 3.5. The data shown in the figure is from GMp kinematic k3-7.

Kinematic	Spectrometer	ϵ_β
k1-0.4	LHRS	$0.9999\ (8 \times 10^{-6})$
k1-1.5	LHRS	$0.9997\ (2 \times 10^{-5})$
k1-1.8	RHRS	$0.9999\ (1 \times 10^{-5})$
k1-1.9	RHRS	$0.9999\ (2 \times 10^{-5})$
k3-4	LHRS	$0.9995\ (1 \times 10^{-4})$
k3-6	LHRS	$0.9995\ (1 \times 10^{-4})$
k3-7	LHRS	$0.9997\ (9 \times 10^{-5})$
k3-8	LHRS	$0.9998\ (9 \times 10^{-5})$
k4-9	LHRS	$0.9997\ (1 \times 10^{-4})$
k4-10	LHRS	$0.9996\ (1 \times 10^{-4})$
k4-11	LHRS	$0.9998\ (1 \times 10^{-4})$
k3-9	RHRS	$0.9998\ (2 \times 10^{-4})$
k4-12	RHRS	$0.9999\ (1 \times 10^{-4})$

Table 3.5: Track beta cut efficiency for a selected cut of beta greater than 0.2 for all GMp Fall 2016 kinematics. The relative uncertainty shown in parenthesis is the statistical (binomial) uncertainty.

Vertical Drift Chamber (VDC) Tracking Efficiency

For every event, the VDC can reconstruct zero, one, or multiple tracks. The 'standard' analysis method in Hall A consists of only analysing the events where the number of tracks is equal to one. Then a correction factor is applied to account for the zero-track and multi-track events: the fraction of events which consist of only one track is determined, and the yield is then divided by this value.

It is useful to briefly consider the merit of this 'one-track efficiency' approach. Let us assume that the VDC can reconstruct multiple tracks well and that the experiment taking data is not limited by statistics. Let us also assume that the experiment is interested in detecting electrons, as was the case for the GMp experiment. For a sample of events where there was a good trigger, good timing, and a large energy deposited in the PID detectors, we know that these events have at least one good electron present. The majority of the events in this sample will have one track in the VDC, and these events will be analysed. Some of the events will not have any track in the VDC. Since we know the event contained a good electron, the fact that there is no track in the VDC indicates that the detector was inefficient for that event. So a correction should be applied, as is done in the standard 'one-track efficiency' correction.

What about the cases where there are multiple tracks in the VDC? This may be because an event has multiple good electrons (a pile-up event). In the standard analysis method, this event will be thrown away; and then the 'one-track efficiency' correction will add back one of the lost electrons. The other lost electrons will be added back through the dead-time (electronic or computer) correction. Indeed, it would be a mistake to try to reconstruct two electrons in the same event, because the second electron is already counted in the dead-time correction. Multiple tracks in the VDC may also arise if there is one good electron and a 'junk' track. [2] The standard tracking correction will correct for the one good electron.

[2]This 'junk' track may be contained in the VDC; or it may be a delta-electron which escapes and either hits or misses the trigger detectors. Even if the 'junk' track hits the trigger detectors, however, it should come at the same time as the good electron track. So it will be within the electronic dead-time window, and it should not be counted by the scalers.

So the standard VDC 'one-track efficiency' correction seems justified. However, there is a complication. The newest version of the analysis software will only form two tracks when there are at least two clusters in all four VDC planes. There are some events where there are two clusters in one plane, but one cluster is the other three planes. In this case, the VDC software will reconstruct one track; but there is not always a robust way to determine which of the two clusters should be used. [3] So it might be better to throw away all events with multiple clusters in any of the four planes, and then calculate a 'one-cluster efficiency' correction. (In addition, when multiple clusters are present, the clusters may interfere with one another, and they may not be reconstructed well.)

In this section, we will calculate both the 'one-track efficiency' and the 'one-cluster' efficiency for the GMp Fall 2016 dataset. We will spend some time discussing placing reasonable uncertainties on the extracted efficiencies. In addition, we will describe a novel technique to extract position-dependent VDC efficiencies by forming a non-VDC 'track' using information from the other detectors.

Overall Efficiencies

To calculate the VDC efficiencies, we begin by selecting a sample of good electrons. First we require the event to have a good hit on the main trigger (trigger 1, which is a coincidence of the two scintillator planes). Then we require at least 5 photoelectrons in the gas cherenkov detector. Lastly we apply a cut on the energy deposited in the calorimeter normalized by the spectrometer central momentum. It is important to highlight the reason that we divide the energy deposited in the calorimeter by the spectrometer central momentum instead of the event momentum, as we did in previous sections. The event momentum is calculated using the central momentum and information from the reconstructed VDC track. Using VDC information when creating a sample to study the VDC efficiency would obviously bias our study. By normalizing the calorimeter energy deposition by a fixed number (the spectrometer

[3] Of course, the VDC software could be changed to reconstruct two tracks here. But this is just a semantic issue, as it would change the 'one-cluster efficiency' into the 'one-track efficiency'.

central momentum), we avoid this particular pitfall.

Now that we have a sample of good electrons, we can calculate the fraction of these events with one track in the VDC or one cluster in all four VDC planes. But we first make use of two additional pieces of information to remove any potential cosmic contamination or events which miss the VDC detector entirely: the relative time in the two scintillator planes, and the hit positions of the event in the two scintillator planes.

The S0 and S2m scintillators have been well calibrated, with regards to their relative times and their positions with respect to the VDC. For every event, we can extract the (X,Y,Z) hit positions for each scintillator. For the S2m scintillator, the Z position relative to the VDC is known; we can set the X position as the center of the S2m paddle that had a hit; and we can use the time difference between the left and right PMTs of the hit paddle to determine the Y position. For the S0 scintillator, the Z position relative to the VDC is known; we can set the Y position as the center of the S0 detector; and we can use the time difference between the top and bottom PMTs to determine the X position. Using the extracted (X,Y,Z) hit positions for the two scintillator detectors, we form a 'track' (i.e. non-VDC track).

Using the scintillator relative times and the scintillator-based track, we calculate a beta for every event (figure 3-25). (If multiple S2m paddles fire, we use the earliest one that was within a 50 ns time window of the S0 hit.) As can be seen in the plot, even after the PID cut, there are a few events with negative beta. We remove these events by requiring the beta to be larger than 0.4 and less than 2.0.

We can also form the standard focal plane tracking variables in the transport coordinate system using the scintillator-based track. We can then remove events from our sample which track far outside the acceptance of the VDC detector. In figure 3-26, we show these four quantities formed with the scintillator-based track, both for all trigger 1 events and for those events passing the above PID and beta cuts. After applying the PID and beta cuts, it is clear that very few events are left which are outside the VDC fiducial region. Nonetheless, we apply cuts to remove the small number of events which are far outside the VDC acceptance.

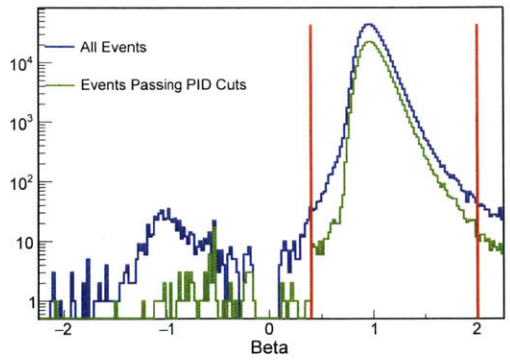

Figure 3-25: Beta formed from the scintillator times and path-length of the scintillator-based track. The blue curve shows all trigger 1 events. The cosmic events are the ones with negative beta. The green curve shows the distribution for the events remaining after the application of the PID cuts discussed in the text. The PID cuts remove the majority of the cosmic events. Note how there are no events with $-0.1 < \beta < 0.1$; this occurs because we require the S0 and S2m hit times to be within 50 ns of each other. The results are shown for an inelastic run on the LHRS.

We use the sample of events remaining after applying the PID, beta, and scintillator-based tracking cuts to study the VDC efficiency. That is, we calculate the fraction of these events that have one-track or one-cluster present in the VDC. Figure 3-27 shows the number of tracks reconstructed by the VDC for the selected event sample for an inelastic run on the LHRS.

In table 3.6, we show the extracted VDC one-track and one-cluster efficiencies for all GMp Fall 2016 kinematics. In addition, the table shows the statistical uncertainty placed on the efficiencies assuming standard binomial uncertainties. We place an additional uncertainty of 0.2% on all extracted VDC efficiencies. This additional uncertainty is needed to take into account the fact that the fraction of one-track or one-cluster events in the physics region of interest may be different from the fraction of multi-track or multi-cluster events in that same region. See Ref. [68] for a more complete discussion.

Position-Dependent Efficiency

While the procedure we developed in the previous section works well for calculating the overall VDC efficiency, the scintillator-based track is not adequate for calculating

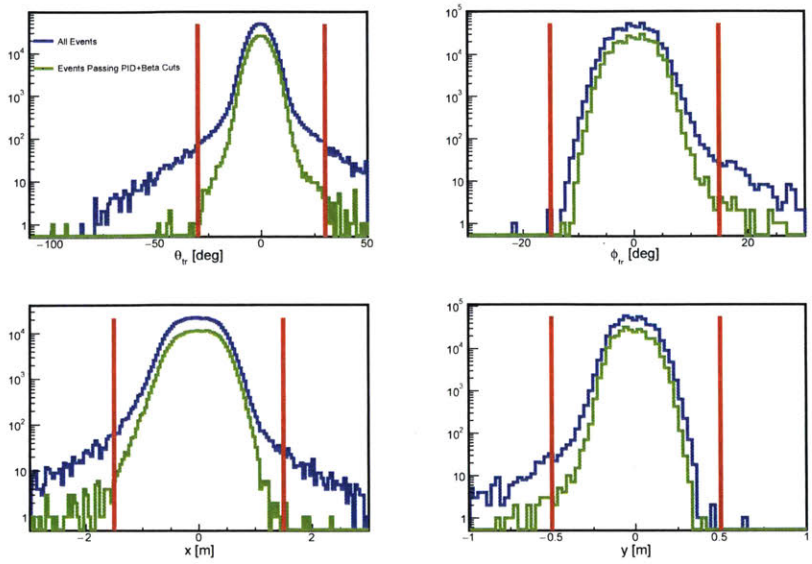

Figure 3-26: The standard focal plane variables in the transport coordinate system formed from the scintillator-based track. (Clockwise from the top left: angle in the dispersive direction, angle in the non-dispersive direction, position in the non-dispersive direction, position in the dispersive direction.) The blue curves show the distributions for all trigger 1 events. The green curves show the distributions after applying the PID and beta cuts discussed in the text. For the green curves, a few events reconstruct far outside the known VDC acceptance; these events are removed with the cuts shown in the figure. The results are shown for an inelastic run on the LHRS.

efficiencies as a function of position in the VDC detector. The reason for this can be seen in figure 3-28. In this figure, we take events in which a good track was reconstructed in the VDC. We then project the VDC track to the S0 (S2m) detector plane, and we compare this track's X (Y) position in the S0 (S2m) plane to the X (Y) position given by the time difference of the S0 (S2m) PMTs. The X position we get by using the S0 PMT time difference can differ from the X position of the VDC track projection by up to 10 cm. For S2m, the PMT-based Y position can differ by 5 cm from that of the VDC track projection. Since the VDC tracks are reconstructed with a high accuracy, this large discrepancy is mostly due to the time resolution of the scintillators (and also perhaps to some multiple scattering between the VDCs and the scintillator detectors).

Thankfully, additional position information from other detectors can be used to

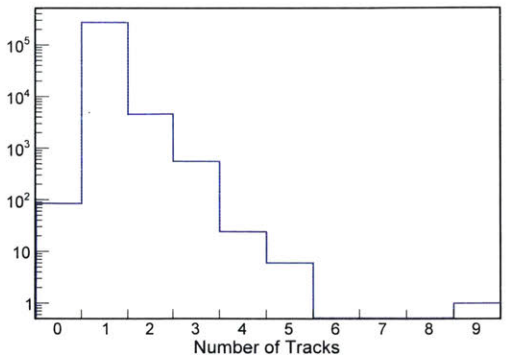

Figure 3-27: Number of tracks reconstructed by the VDC for a sample of good electrons. The results are shown for an inelastic run on the LHRS.

form a more accurate non-VDC-based track. In the calorimeter, we have access to the energy-weighted X and Y hit positions in both layers (figure 3-29). In the straw chambers, we can extract X and Y positions based on which straws had signals for that event (figure 3-30).

So we have five potential sets of (X,Y,Z) values for each event: one from S0, one from S2m, two from the calorimeter (since there are two layers), and one from the straw chamber. Since we have already imposed the requirement that trigger 1 is present and that there is a large amount of energy deposited in the calorimeter (i.e. the PID cuts), we are guaranteed to have at least four (X,Y,Z) values for every event. (If there are multiple clusters in the calorimeter, we take the one with the largest energy deposition.) When the event has one cluster in the straw chamber, we include the (X,Y,Z) hit information from the straw chamber; if the straw chamber has zero or multiple clusters, we do no use the straw chamber information. We weight each used X and Y position based on its accuracy (as determined from figures 3-28 - 3-30), and we perform a least-squares fit to determine a track.

Figure 3-31 compares the non-VDC-based track to the standard VDC track for events with one cluster in all four VDC planes. The figure shows the difference between the non-VDC-based track and the standard VDC track for the four focal plane quantities in the transport coordinate system. The blue curves show the differences between the non-VDC-based track and the standard VDC track when only the two

Kinematic	Spectrometer	$\epsilon_{1-track}$	$\epsilon_{1-cluster}$
k1-0.4	LHRS	$0.9899\ (9.6 \times 10^{-5})$	$0.9282\ (2.6 \times 10^{-4})$
k1-1.5	LHRS	$0.9913\ (9.6 \times 10^{-5})$	$0.9244\ (2.9 \times 10^{-4})$
k1-1.8	RHRS	$0.9940\ (9.7 \times 10^{-5})$	$0.9242\ (3.5 \times 10^{-4})$
k1-1.9	RHRS	$0.9940\ (1.3 \times 10^{-4})$	$0.9244\ (4.8 \times 10^{-4})$
k3-4	LHRS	$0.9728\ (6.5 \times 10^{-4})$	$0.8886\ (1.37 \times 10^{-3})$
k3-6	LHRS	$0.9770\ (4.9 \times 10^{-4})$	$0.9016\ (1.06 \times 10^{-3})$
k3-7	LHRS	$0.9800\ (5.1 \times 10^{-4})$	$0.9107\ (1.11 \times 10^{-3})$
k3-8	LHRS	$0.9846\ (5.6 \times 10^{-4})$	$0.9171\ (1.35 \times 10^{-3})$
k4-9	LHRS	$0.9726\ (4.1 \times 10^{-4})$	$0.8949\ (1.27 \times 10^{-3})$
k4-10	LHRS	$0.9744\ (4.0 \times 10^{-4})$	$0.9015\ (1.27 \times 10^{-3})$
k4-11	LHRS	$0.9793\ (6.0 \times 10^{-4})$	$0.9095\ (1.27 \times 10^{-3})$
k3-9	RHRS	$0.9905\ (7.4 \times 10^{-4})$	$0.9195\ (2.24 \times 10^{-3})$
k4-12	RHRS	$0.9833\ (7.5 \times 10^{-4})$	$0.9118\ (1.80 \times 10^{-3})$

Table 3.6: Extracted VDC one-track and one-cluster efficiencies for all GMp Fall 2016 kinematics. The relative uncertainty shown in parenthesis is the statistical (binomial) uncertainty. As discussed in the text, we suggest placing an additional uncertainty of 0.2% on these values.

scintillators are used to form the non-VDC-based track; the red curves show the differences when the two scintillators and the calorimeter are used to form the non-VDC-based track; the green curves show the differences when the non-VDC-based are formed as described in the previous paragraph. As can be seen in the figure, the resolution on the green curves is quite good. (In figure 3-32, we show the same differences as in figure 3-31 for the final non-VDC-based track, but this time as a function of position in the VDC detector.)

The upshot of all this is the following: for a sample of good electrons selected by the trigger and PID detectors, we can form a non-VDC-based track using the scintillators, the calorimeter, and (usually) the straw chamber. We can then bin that sample across the entire VDC detector and study the one-track and one-cluster efficiency of the VDC in different parts of the detector. We do this as a function of the X and Y position in the focal plane transport coordinate system in figures 3-33 and 3-34 for an inelastic run on the LHRS. As can be seen in figure 3-34, the one-cluster efficiency shows a minor dependence on X. (The full rotated width of the VDC in the X direction in the transport coordinate system is 156 cm.) It appears that the

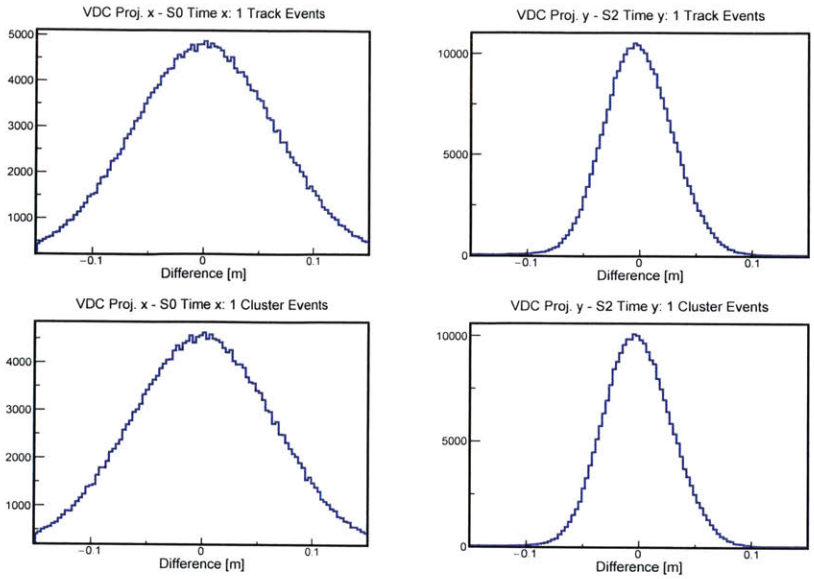

Figure 3-28: Top/Bottom Left: Difference between the VDC track projection to the S0 scintillator in the X direction and the position determined by the S0 PMT times. The top plot is shown for events with one track in the VDC; the bottom plot is shown for events with one cluster in all four VDC planes. Top/Bottom Right: Difference between the VDC track projection to the S2m scintillator in the Y direction and the position determined by the S2m PMT times of the struck paddle. The top plot is shown for events with one track in the VDC; the bottom plot is shown for events with one cluster in all four VDC planes.

efficiency shows a major dependence on Y. However, while the full physical width of the VDC in the Y direction is 30 cm, the vast majority of the events fall within about 8 cm of the center of the VDC for the run studied, as can be seen in figure 3-32. In this narrow window, the efficiency is very stable.

The technique we described in this section can be used to extract position-dependent VDC efficiencies in many situations. However, we do not think it is correct to apply the curves in figure 3-34 as a general efficiency correction. The VDC one-track and one-cluster overall efficiency will change with the event rate, and the shape of the efficiency curve across the VDC may be affected by the relative event rate. For experiments, like GMp, where the events of interest are rather localized at the focal plane, a single number for the VDC efficiency correction is probably sufficient.

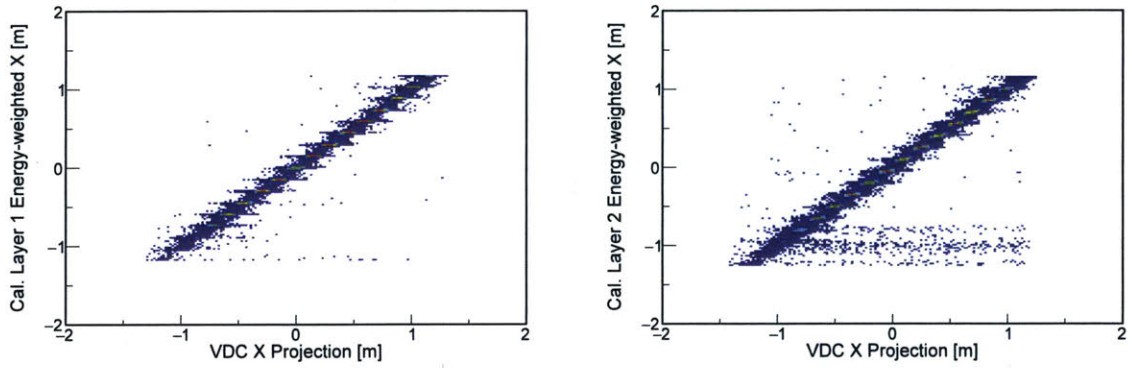

(a) (b)

Figure 3-29: The energy-weighted X position of the largest-energy cluster in the calorimeter vs. the VDC track X projection to the calorimeter. Since the extracted energy-weighted position is consistent with the VDC position (within resolution), the energy-weighted position can be used when calculating the non-VDC-based track. The left plot is for calorimeter layer 1, while the right plot is for calorimeter layer 2. The results are shown for a LHRS inelastic run.

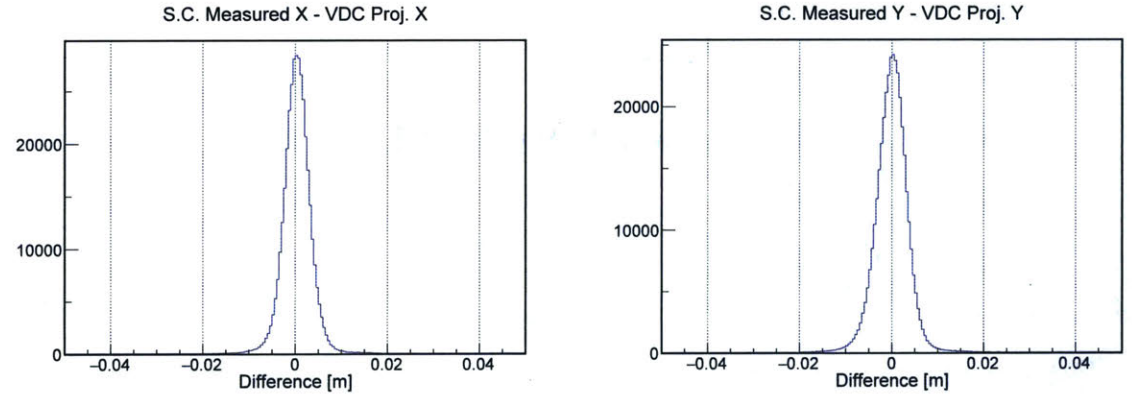

(a) (b)

Figure 3-30: Left (Right): The difference between the position extracted from the straw chamber in the X (Y) direction minus the position of the VDC track projected to the straw chamber. The extracted positions are consistent to better than 1 cm. This means that the straw chamber hit information can be used when forming a non-VDC-based track. The results are shown for events with a single track in the VDC and a single cluster in the straw chamber. The straw chamber geometry consists of 3 parallel layers followed by an additional 3 layers perpendicular to these; so we assume that all straw chamber hits occur at the center of the detector in the Z direction when calculating the hit X and Y positions. The results are shown for a LHRS inelastic run.

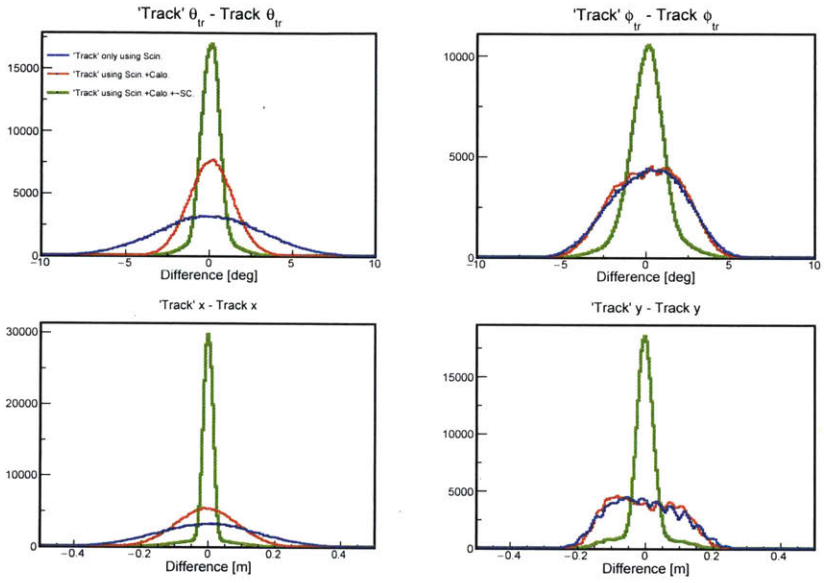

Figure 3-31: The difference between the standard focal plane variables in the transport coordinate system formed from the non-VDC-based track and those formed from the standard VDC track for events with one cluster in all four VDC planes. (Clockwise from the top left: difference in the angle in the dispersive direction, difference in the angle in the non-dispersive direction, difference in the position in the non-dispersive direction, difference in the position in the dispersive direction.) As discussed in the text, the blue curve shows the difference when only the two scintillators are used to form the non-VDC-based track. The red curve shows the difference when the calorimeter information is included in addition. The green curve shows the difference when the straw chamber information is included as well, if a single cluster is present in the straw chamber. The results are shown for an inelastic run on the LHRS.

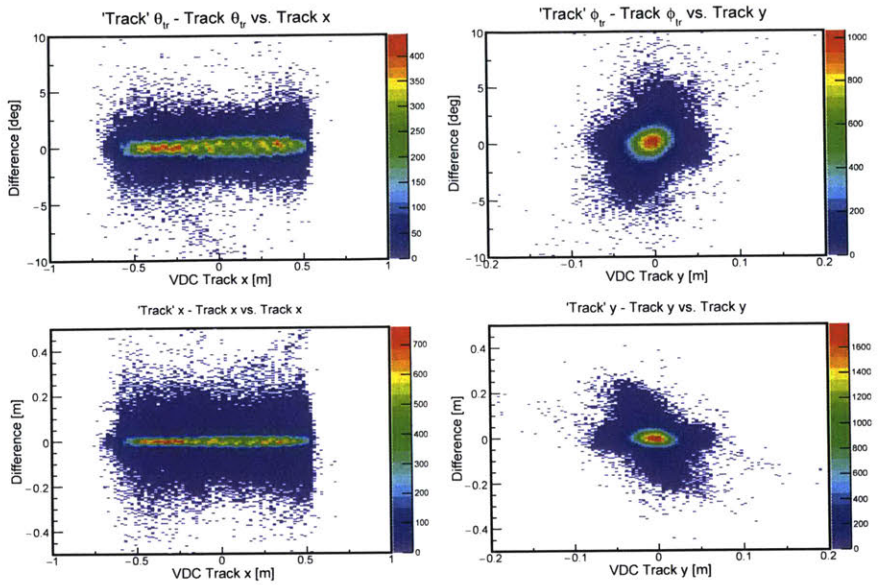

Figure 3-32: The difference between the standard focal plane variables in the transport coordinate system formed from the non-VDC-based track and those formed from the standard VDC track vs. the position in the VDC (as determined from the standard VDC track). (Clockwise from the top left: difference in the angle in the dispersive direction vs. the position in the dispersive direction, difference in the angle in the non-dispersive direction vs. the position in the non-dispersive direction, difference in the position in the non-dispersive direction vs. the position in the non-dispersive direction, difference in the position in the dispersive direction vs. the position in the dispersive direction.) The results show that the final non-VDC-based track is accurate across the entire VDC detector. The results are shown for an inelastic run on the LHRS.

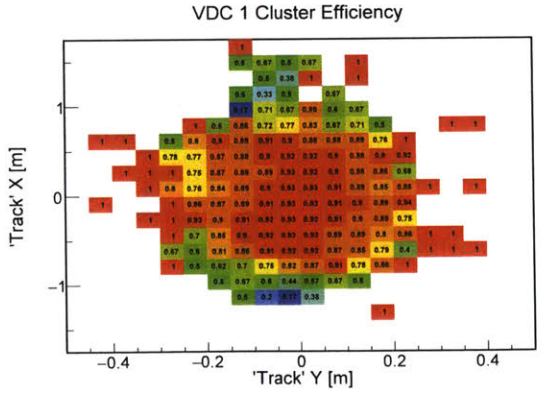

Figure 3-33: Fraction of the good electron events which contain one cluster in all four VDC planes as a two-dimensional function of position at the VDC. The data is binned in X vs. Y in the focal plane transport coordinate system using the non-VDC-based track, and an efficiency is calculated for each bin. The results are shown for an inelastic run on the LHRS.

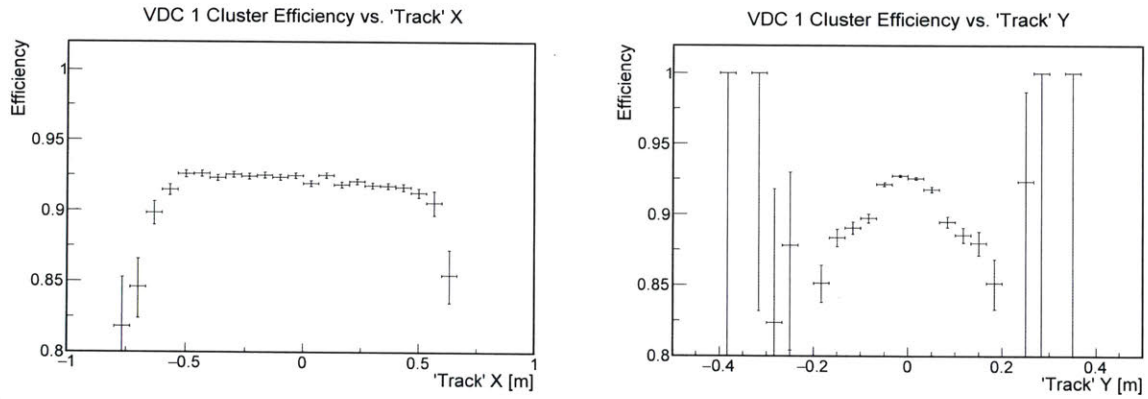

(a) (b)

Figure 3-34: Left (Right): Fraction of the good electron events which contain one cluster in all four VDC planes as a function of the X (Y) position at the VDC. The data is binned in X (Y) in the focal plane transport coordinate system using the non-VDC-based track, and an efficiency is calculated for each bin. The results are shown for an inelastic run on the LHRS.

Cosmic Suppression

As mentioned in previous sections, the main trigger for the GMp experiment was Trigger 1 (T1), a coincidence of the two scintillator detectors (S0 and S2m). This trigger collected cosmic events at a raw rate of approximately 5 Hz. Since the GMp experiment took data for over a month, it is important to determine whether any cosmic contamination is present in the data after the application of our final software cuts. During the experiment, we were able to take a 33 hour cosmic run on the LHRS (i.e. a run where we collected data in the same way as during production running, but no beam was present in the experimental hall). We can use this run to study our success in suppressing cosmic contamination with our software cuts.

For this cosmic run, figure 3-35a shows the beta distribution for T1 events. The beta is calculated using the relative time between the two scintillator detectors and the scintillator-based track described in section 3.3. The vast majority of events have a negative beta peaked at -1, as expected (i.e. the cosmic event first hits S2m and then hits S0). However, there are a few events peaked around beta equal to +1. Since at this point we only require the two scintillator detectors to have a signal, these events may be ones that first hit the top of the S0 detector before striking the S2m detector. In figure 3-35b, we plot the beta vs. the angle in the dispersive direction (i.e. the vertical direction) for the same events as shown in figure 3-35a. As can be seen in figure 3-35b, the events with negative beta have a negative angle. This is consistent with the events hitting S2m at a higher part of the detector than S0. (Remember that +X is down, and +Z points from S0 to S2m.) The events with positive beta tend to have a positive angle. This suggests that these events hit S0 higher than S2m.

The important question for the cosmic contaimination is what happens when we apply cuts on the VDC and the PID detectors. In figure 3-36, we plot the beta distribution for the cosmic run under study after applying cuts on the VDC and PID detectors. We require a single cluster to be present in all four VDC planes, and we require 5 photoelectrons in the gas cherenkov detector. In addition, we require the total energy deposited in the calorimeter to be greater than 510 MeV. This is

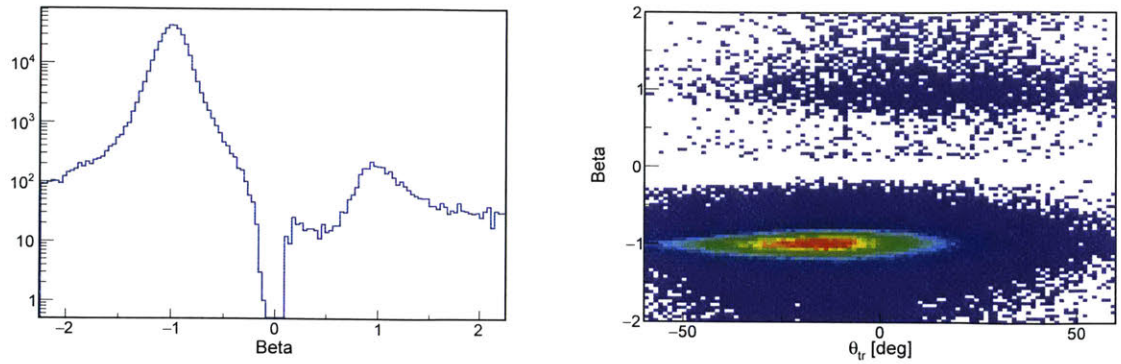

(a) (b)

Figure 3-35: (a) Beta calculated from the scintillator times and scintillator-based track for a cosmic run on the LHRS. The vast majority of events have a negative beta, as expected for cosmic particles, but a few events have positive beta. The events shown here are the same ones in figure 3-35a. (b) The angle calculated using the scintillator-based track vs. beta. The coordinate system used to define the angle is the spectrometer transport coordinate system. So a positive angle means that the event hit the S0 detector vertically higher than the S2m detector (+X points down). As discussed in the text, the events with positive beta have a more positive angle, indicating that they hit the S0 detector prior to the S2m detector.

equivalent to requiring a momentum-normalized energy deposition of 0.6 if the central momentum is 850 MeV/c. (For the GMp production data, the set momentum was always greater than 1 GeV/c; so what is shown here is a worst-case scenario.) As can be seen in the figure, there are still approximately 100 events remaining after the VDC and PID cuts. However, they are all at negative beta.

We can conclude that the combination of trigger, VDC, PID, and beta cuts are sufficient to remove all cosmic events over a 33 hour period. The higher Q^2 GMp kinematic settings took data for approximately a week, and accumulated about 10,000 good electrons during that time. In addition to the cuts discussed here, software cuts are applied on the reconstructed target quantities and the invariant mass. These cuts would further reduce the cosmic contamination. Furthermore, these higher Q^2 kinematics had central momentum settings of around 2 GeV/c; thus the applied calorimeter energy deposition cut is higher than the one used in this study. So it is justified to claim that the final cosmic contamination is less than 5×10^{-4}.

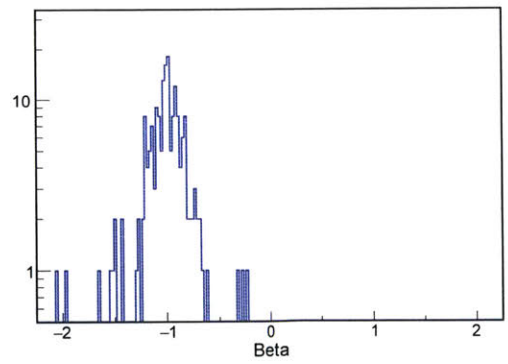

Figure 3-36: Beta distribution for cosmic events on the LHRS after applying the tracking and PID cuts discussed in the text. There are 100 or so events left in the plot, all at negative beta.

Computer and Electronic Live-Time

When an event triggers the data-acquisition system, another event can not be processed for some time. We need to correct for the number of events lost during this time period. Because the events which occur during the period when the data-acquisition is down are still recorded on the scalar counters, we define the computer live-time as the ratio of the number of events recorded for the main trigger divided by the number of counts on the main trigger scalar. The measured yield then needs to be divided by the computer live-time to correct for the lost time. (For the GMp experiment, the pre-scale factor for the main trigger was always set to one during production running. If this were not the case, we would need to take this into account in our calculation.) In table 3.7, we show the computer live-time for all GMp Fall 2016 kinematics, along with the accompanying relative uncertainties calculated using standard binomial errors.

In addition, there is a set of events that are not recorded on the scalar counters. These lost events are due to the electronic dead-time. For every recorded event, the number of lost events is equal to $Rate \times \tau$, where $Rate$ is the raw event rate on the scalar counters and τ is the electronic dead-time. To correct for this electronic dead-time, the measured yield should be multiplied by the following factor:

Kinematic	Spectrometer	Computer Live-Time
k1-0.4	LHRS	0.6935 (5.1×10^{-4})
k1-1.5	LHRS	0.9454 (2.2×10^{-4})
k1-1.8	RHRS	0.9171 (3.3×10^{-4})
k1-1.9	RHRS	0.9207 (5.1×10^{-4})
k3-4	LHRS	0.9654 (4.2×10^{-4})
k3-6	LHRS	0.9774 (3.1×10^{-4})
k3-7	LHRS	0.9794 (1.1×10^{-4})
k3-8	LHRS	0.9843 (3.0×10^{-4})
k4-9	LHRS	0.9742 (2.5×10^{-4})
k4-10	LHRS	0.9728 (2.6×10^{-4})
k4-11	LHRS	0.9790 (3.6×10^{-4})
k3-9	RHRS	0.9684 (5.4×10^{-4})
k4-12	RHRS	0.9547 (6.5×10^{-4})

Table 3.7: Extracted computer live-times for all GMp Fall 2016 kinematics. The relative (i.e. fractional) uncertainty shown in parenthesis is calculated assuming binomial errors.

$$Correction\,Factor = 1 + Rate \times \tau\,.$$

One way to estimate the correction factor is to use multiple coincidence units with different output widths [19]. In our case, we make use of the fact that we have multi-hit TDCs. Figure 3-37a shows the TDC time (relative to a common start) for the main trigger when two hits are present. The vertical axis is the earlier hit, and the horizontal axis is the later hit. The vertical band in the figure shows events for which earlier hit came prior to the data acquisition system being ready to accept an event. The horizontal band represents events for which the earlier hit carried the time. By examining the gap in the middle of the figure, we can conclude that the electronic dead-time (τ) is about 40 ns.

In figure 3-37b, we plot the correction factor as a function of rate for a 40 ns electronic dead-time. For GMp Fall 2016 production running, the raw rate was always below 6 kHz (usually below 1 kHz). This means the correction due to the electronic dead-time is at most 2×10^{-4}.

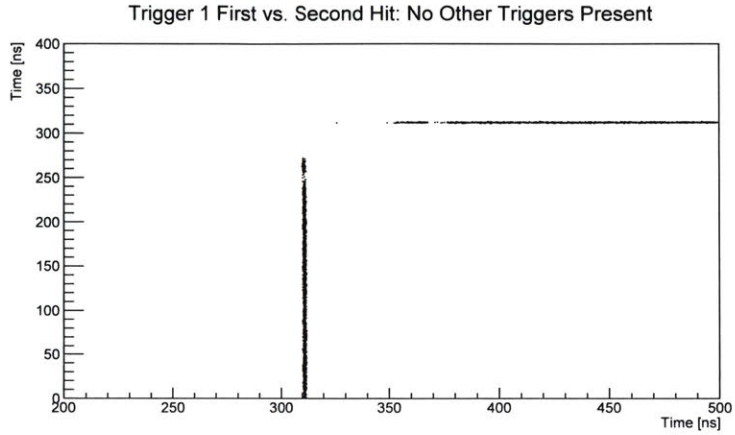

(a)

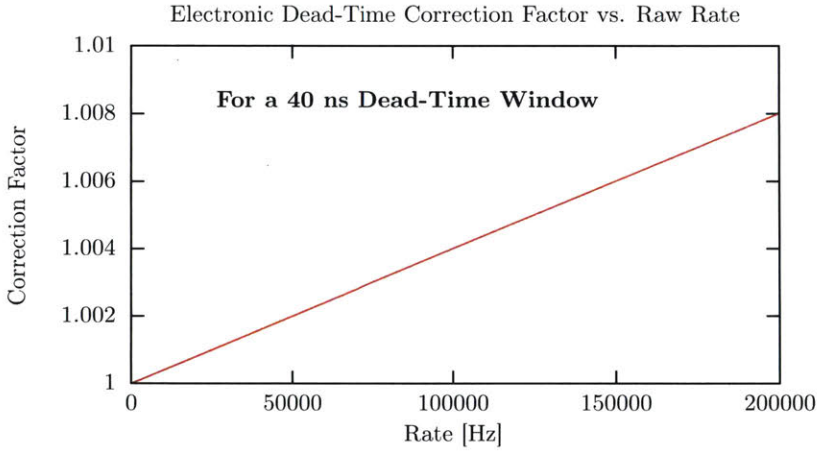

(b)

Figure 3-37: (a) Main trigger TDC times for events with two hits. The interpretation of the figure is discussed in the text. (b) Electronic dead-time correction factor vs. raw rate. The plot is made assuming a 40 ns electronic dead-time. The measured yield should be multiplied by this correction factor.

3.4 Preliminary Cross-Section Results

The data collected by the *GMp* experiment for large Q^2 is at lower ϵ than the SLAC data [69] extracted in the same Q^2 range (figure 3-38a). The *GMp* data was collected with better than 1% statistical uncertainty for the majority of the measured kinematic points. The final combined point-to-point and normalization systematic uncertainties are expected to be better than 2.25%. This will give a total uncertainty of better than 2.5% for the majority of measured reduced cross-sections.

The *GMp* collaboration has extracted preliminary cross-section results for much of the data collected in the spring and fall of 2016. These preliminary results are shown in figure 3-38b without uncertainties for $Q^2 > 6\ GeV^2$. The final results should be completed before the end of 2018.

Since the *GMp* dataset is at lower ϵ and will have better uncertainties than the high Q^2 SLAC data, the measured cross-sections will have a smaller contribution from the electric form factor. This allows for a higher precision extraction of the magnetic form factor, which can be used to test the high Q^2 QCD scaling of the Dirac F_1 form factor [1]. In addition, the *GMp* results are needed for the extraction of the individual form factors from the ratios obtained from the future high Q^2 recoil polarization measurement at JLab [70].

Note that the cross-sections presented in figure 3-38b are divided by the cross-sections assuming dipole form factors. Once this normalization is made, the results from the two datasets agree with each other to the few percent level. This is to be expected if the form factors extracted using inclusive scattering approximately scale (i.e. the ratio of the electric to magnetic form factors is a constant). The form factors extracted using inclusive scattering cross-section measurements are expected to scale in some approaches even if the measurements are contaminated by two-photon exchange effects [9].

A global analysis of the inclusive cross-section measurements and the form factor ratios extracted from the polarization transfer results can be used to constrain two-photon exchange effects. For example, the measured inclusive cross-sections can be

written as

$$\sigma_R^{exp} = \sigma_R^{Born} + \sigma_R^{2\gamma}\,, \tag{3.4}$$

where σ_R^{exp} is the measured inclusive cross-section, σ_R^{Born} is the true Born cross-section, and $\sigma_R^{2\gamma}$ is the contribution from two-photon exchange. The Born term can be written as

$$\sigma_R^{Born} = \tau(G_M^p)^2(1 + \frac{\epsilon}{\tau}R^2)\,, \tag{3.5}$$

where R is the ratio of the electric to magnetic form factors, which comes from the polarization data.

The magnetic form factor, $(G_M^p)^2$, and the two photon exchange term, $\sigma_R^{2\gamma}$, can then be parametrized based on different models, and those models can be compared to the measured data.

The final, high precision *GMp* results will be an important input to these types of global studies.

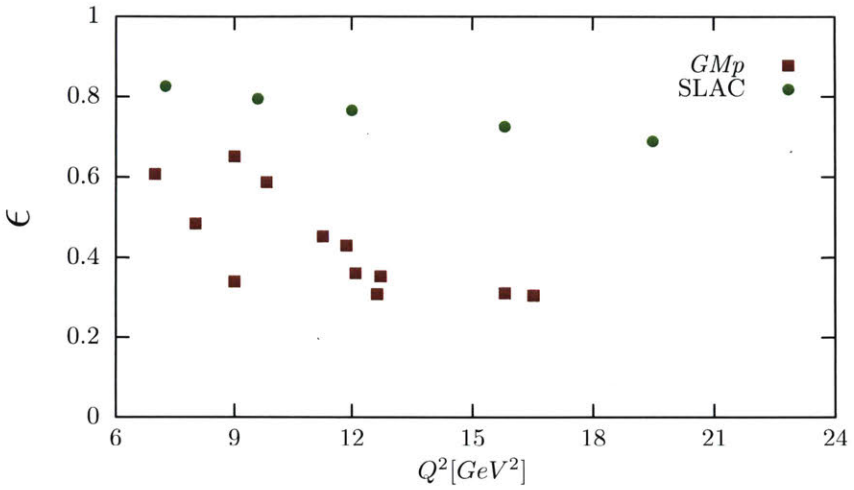

(a) *GMp* kinematic coverage in ϵ vs. Q^2 compared to the coverage for the SLAC data [69]. The data is shown for $Q^2 > 6\ GeV^2$, the high Q^2 portion of the *GMp* dataset. Preliminary cross-sections have been extracted for some of the shown *GMp* kinematic points.

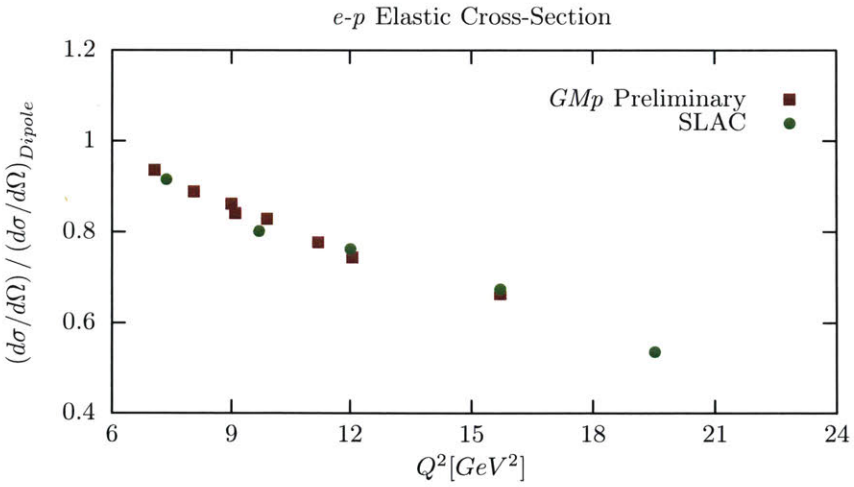

(b) Preliminary cross-section results as a function of Q^2 for the *GMp* experiment for $Q^2 > 6\ GeV^2$ kinematic points which have been currently studied. The measured cross-section is divided by cross-section assuming dipole form factors. The SLAC data [69] is shown for comparison. No uncertainties are shown in the figure.

Figure 3-38: GMp kinematics and preliminary results

Chapter 4

Conclusions

This thesis presented studies of nucleon structure at different resolution scales using inclusive electron scattering, including studies of how that structure is modified by the nuclear medium. Nucleon structure is of course a very broad term with many different avenues of study. This thesis focused on three topics: the electromagnetic structure of the proton as encapsulated by the form factors, the motion of nucleons inside the nucleus in the high-momentum SRC region, and the modification of the inelastic structure of the nucleon by the nuclear medium (the *EMC* effect). The work related to the electromagnetic form factors was conducted in Hall A at JLab, while the data analysed on nucleon SRCs and the *EMC* effect were collected using the *CLAS* detector in Hall B at JLab.

The electromagnetic form factors of the proton have been under experimental and theoretical study for many years. From an experimental standpoint, these form factors are unknown functions of Q^2 that are present in the elastic electron-proton Born cross-section formula. These functions can then be extracted by measuring the elastic cross-section. Much work has been done to show that these form factors are the momentum space representations of the charge and magnetic distributions inside the proton [1]. The electric and magnetic form factors exhibit scaling when extracted using the Rosenbluth method, but this scaling was not observed in the recently developed polarization transfer technique [8]. This may be an indication that hard two-photon exchange effects play a large role in the Rosenbluth results

[9, 71]. As discussed in section 3.4, one way to put better constraints on two-photon exchange models is by taking precision elastic cross-section measurements at high Q^2 and relatively low ϵ. These are the results that the *GMp* experiment will publish in the next several months.

A direct way to nail down the radiative corrections for electron-proton elastic scattering is by comparing electron-proton and positron-proton elastic cross-sections [72]. Looking into the future, the small acceptance spectrometers in Hall A and Hall C at JLab would be an ideal place to make these measurements if a future positron beam were available [73].

The other topic discussed in this thesis was the *EMC* effect and its connection with nucleon SRCs. The *EMC* effect is non-trivial, in the sense that it cannot be explained without modifying the nucleon structure or including multi-nucleon clusters. If the nucleon inelastic structure is modified and certain quarks move slower on average in the nuclear medium, the question is how that modification takes place - primarily in the mean-field or in SRC pairs.

This thesis presented new measurements of the *EMC* effect in heavy nuclei, including the first measurement on the asymmetric nucleus lead. The results of these measurements are consistent with previously published data. We made simultaneous measurements of the SRC pair probability (a_2) in the same heavy nuclei. This work made the first measurements of a_2 on aluminum and lead, as well as the first direct iron to deuterium measurement.

One unique aspect of the measurements presented here is that they were performed at a large acceptance spectrometer, while the vast majority of the previous electron-based inclusive measurements were performed using small acceptance spectrometers. This means that the cross-section ratios presented here are integrated over a somewhat wide Q^2 range for every x_B point. As discussed in section 2.6, we studied the kinematic cut sensitivity of the extracted *EMC* slopes. We varied the Q^2 cut between 1.5 and 2.5 GeV^2 and the W cut between 1.8 and 2.0 GeV. We observed the slopes to be independent of the selected cut.

Lastly, this thesis developed a data-driven SRC-based *EMC* modification func-

tion. Prior data-driven studies of the connection between the *EMC* effect and SRC [28, 29] did not take into account the known isospin dependence of SRC pairs. This work developed a simple isospin-dependent model that quantified the connection between the *EMC* effect and SRCs. This model was able to consistently describe the *EMC* effect for nuclei ranging from ^{3}He to ^{208}Pb. As nuclei become heavier and more asymmetric, this model makes the interesting prediction that the *EMC* effect will continue to grow for protons but will saturate for neutrons. This growth and saturation behavior was confirmed by calculating per-neutron and per-proton cross-section ratios for the measured data.

Future measurements of "tagged" DIS [74] - where a high momentum spectator nucleon is detected in addition to the scattered electron - will allow testing this model's extraction directly, providing further insight to the underlying mechanisms driving bound nucleon structure modification in QCD.

Bibliography

[1] C. Perdrisat, V. Punjabi, and M. Vanderhaeghen. *Prog. Part. Nucl. Phys.*, 59:694–764, 2007.

[2] N. Fomin, D. Higinbotham, M. Sargsian, and P. Solvignon. New results on short-range correlations in nuclei. arXiv:1708.08581.

[3] O. Hen, G. A. Miller, E. Piasetzky, and L. B. Weinstein. *Rev. Mod. Phys*, 89:045002, 2017.

[4] P. R. Norton. *Rep. Prog. Phys.*, 66:1253, 2003.

[5] David Griffiths. *Introduction to Elementary Particles.* Wiley-VCH, Second, Revised edition, 2008.

[6] Y. Wang. *Measurement of the Elastic Ep Cross Section at Q^2 = 0.66,1.10,1.51 and 1.65 GeV^2.* PhD thesis, College of William and Mary, 2017.

[7] M.N. Rosenbluth. *Physical Review*, 79:615, 1950.

[8] O. Gayou et al. *Phys. Rev. Lett.*, 88:092301, 2002.

[9] P. A. M. Guichon and M. Vanderhaeghen. *Phys. Rev. Lett.*, 91:142303, 2003.

[10] K. Egiyan et al. *Phys. Rev. C*, 68:014313, 2003.

[11] J. Seely. *Precise Measurement of the Nuclear Dependence of Structure Functions in Light Nuclei.* PhD thesis, Massachusetts Institute of Technology, 2006.

[12] Particle Data Group collaboration, S. Eidelman, et al. *Physics Letters B*, 592:1–1109, 2004.

[13] J.J. Aubert et al. *Physics Letters B*, 123:275–278, 1983.

[14] O. Hen et al. *Int. J. Mod. Phys. E*, 22:1330017, 2013.

[15] J.J. Aubert et al. *Nucl. Phys. B*, 293:740–786, 1987.

[16] S. Malace, D. Gaskell, D.W. Higinbotham, and I. Cloet. *Int. J. Mod. Phys. E*, 23:1430013, 2014.

[17] G. Bari et al. *Physics Letters B*, 163:282, 1985.

[18] J. Seely et al. *Phys. Rev. Lett.*, 103:202301, 2009.

[19] J. Gomez et al. *Phys. Rev. D*, 49:4348, 1994.

[20] G. L. Li, K. F. Liu, and G. E. Brown. *Physics Letters B*, 213:531–536, 1988.

[21] C. Ciofi degli Atti and S. Liuti. *Physics Letters B*, 225:215–221, 1989.

[22] L. L. Frankfurt and M. I. Strikman. *Physics Letters B*, 183:254, 1987.

[23] M. Ericson and A. W. Thomas. *Physics Letters B*, 128:112–116, 1983.

[24] D. M. Alde et al. *Phys. Rev. Lett.*, 64:2479, 1990.

[25] J. R. Smith and G. A. Miller. *Phys. Rev. Lett.*, 91:212301, 2003.

[26] I. C. Cloet, W. Bentz, and A. W. Thomas. *Phys. Rev. Lett.*, 95:052302, 2005.

[27] I. C. Cloet, W. Bentz, and A. W. Thomas. *Phys. Rev. Lett.*, 102:202301, 2009.

[28] L. B. Weinstein et al. *Phys. Rev. Lett.*, 106:052301, 2011.

[29] O. Hen, E. Piasetzky, and L. B. Weinstein. *Phys. Rev. C*, 85:047301, 2012.

[30] J. Arrington, S. Gilad, B. Moffit, B. Wojtsekhowski, et al. Jefferson Lab experiment E12-07-108 (GMp).

[31] B.A. Mecking et al. *Nuclear Instruments and Methods A*, 503:513–553, 2003.

[32] L. B. Weinstein and S.E. Kuhn. Short distance structure of nuclei: Mining the wealth of existing Jefferson Lab data. DOE Grant DE-SC0006801.

[33] W. K. Brooks et al. Quark propagation through cold QCD matter, 2002. Proposal to PAC22.

[34] K. Hafidi et al. Q^2 dependence of nuclear transparencies for incoherent ρ^0 electroproduction, 2002. Proposal to PAC22.

[35] H. Hakobyan et al. *Nuclear Instruments and Methods A*, 592:218–223, 2008.

[36] C. W. Leemann, D. R. Douglas, and G. A. Krafft. *Ann. Rev. Nucl. Part. Sci.*, 51:413, 2001.

[37] L. Zana. *Search for the Onset of Color Transparancy Through ρ^0 Electroproduction on Nuclei.* PhD thesis, University of New Hampshire, 2010.

[38] R. Dupre. *Quark Fragmentation and Hadron Formation in Nuclear Matter.* PhD thesis, 2011.

[39] L. El Fassi et al. Search for the onset of color transparency via ρ^0 electroproduction off nuclei. CLAS analysis note, 2011.

[40] O. Hen et al. Probing PP-SRC in ^{12}C, ^{27}Al,^{56}Fe, and ^{208}Pb using the A(e,e'p) and A(e,e'pp) reactions. CLAS analysis note, 2013.

[41] N. Baltzell and S. Stepanyan. Beam XY-position at the target for CLAS/EG6. CLAS note 2013-007.

[42] D. Protopopescu et al. Electron momentum corrections for CLAS at 4.4 GeV. CLAS note 2001-008.

[43] S. Stepanyan. Beam energy measurement with $ep \to ep$ elastic scattering on CLAS. CLAS note 2002-008.

[44] K. Y. Kim et al. General momentum correction for CLAS ... CLAS note 2001-018.

[45] A. Klimenko and S. Kuhn. Momentum corrections for E6. CLAS note 2003-005.

[46] M. Ungaro. *π^0 electroproduction from $\Delta(1232)$ at high momentum transferred with CLAS.* PhD thesis, 2005.

[47] V. Burkert, L. Elouadrhiri, and S. Stepanyan. Deep Virtual Compton scattering with CLAS. CLAS note 2001-006.

[48] D. Higinbotham and S. Stepanyan. Private Communication.

[49] L. W. Mo and Y.S. Tsai. *Rev. Mod. Phys.*, 41:205, 1969.

[50] SIMC Monte Carlo. `https://hallcweb.jlab.org/wiki/index.php/SIMC_Monte_Carlo`.

[51] R. C. Torres. Private Communication.

[52] M. Sargsyan. Computer code for Inclusive (e,e') electro-production reactions and radiative corrections. CLAS note 90-007.

[53] A. Aste and J. Jourdan. *Europhys. Lett.*, 67:753–759, 2004.

[54] P. Solvignon, D. Gaskell, and J. Arrington. Coulomb Distortion in the Inelastic Regime. arXiv:0906.0512.

[55] N. Fomin et al. *Phys. Rev. Lett.*, 100:092502, 2012.

[56] X. Zheng. Cryogenic Target Thickness Study for EG2. Technical report, 2003. `http://www.jlab.org/~xiaochao/eg2/eg2targ.ps`.

[57] N. Fomin. *Inclusive electron scattering from nuclei at $x > 1$ and high Q^2 with a 5.75 GeV beam.* PhD thesis, 2008.

[58] A. Daniel. *Precise Measurement of the Nuclear Dependence of the EMC Effect at Large x.* PhD thesis, 2007.

[59] J. Arrington, F. Coester, R. J. Holt, and T.-S.H. Lee. *J. Phys. G*, 36:025005, 2009.

[60] S. A. Kulagin and R. Petti. *Phys. Rev. C*, 82:054614, 2010.

[61] M. Duer et al. *Nature*, 2018. in press.

[62] S. Dulat et al. *Phys. Rev. D*, 93:033006, 2016.

[63] L. Ou. The GMp Experiment...: Presentation at the Hall A Collaboration Meeting, January 2018.

[64] J. Alcorn et al. *Nuclear Instruments and Methods A*, 522:294, 2004.

[65] T. Gautam. Charge Calibration at Hall A. Technical report, 2017.

[66] V. Sulkosky. Data Acquisition for the Hall A High Resolution Spectrometers during 12 GeV. `http://hallaweb.jlab.org/12GeV/experiment/E12-07-108/DAQ/HallA_hrs_daq.pdf`.

[67] B. Schmookler. Detector position determination: GMp analysis logbook entry.

[68] L. Ou. Using straw chamber to reconstruct target variables: GMp analysis logbook entry.

[69] A. F. Sill et al. *Phys. Rev. D*, 48:29–55, 1993.

[70] C. F. Perdrisat et al. Large Acceptance Proton Form Factor Ratio Measurements...: Jefferson Lab Hall A PAC Proposal.

[71] I. A. Qattan, A. Alsaad, and J. Arrington. *Phys. Rev. C*, 84:054317, 2011.

[72] B. S. Henderson et al. *Phys. Rev. Lett.*, 118:092501, 2017.

[73] A. Afanasev et al. Physics with Positron Beams at Jefferson Lab 12 GeV: Letter-of-Intent to the Jefferson Lab PAC.

[74] O. Hen et al. Jefferson Lab experiments E12-11-107 and E12-11-003.